



Università degli Studi di Catania

in convenzione con



Università degli Studi di Palermo

DOTTORATO DI RICERCA
Scienza dei Materiali e Nanotecnologie
XXX ciclo

RICCARDO GIOVANNI URSO
EXPERIMENTAL STUDIES OF THE EFFECT OF ENERGETIC
PROCESSING ON ASTROPHYSICAL RELEVANT MATERIALS

TESI DI DOTTORATO

Coordinatore: PROF.SSA MARIA GRAZIA GRIMALDI
Tutor: PROF. GIUSEPPE COMPAGNINI
Cotutor: DOTT.SSA MARIA ELISABETTA PALUMBO

ANNO ACCADEMICO 2016-2017

Contents

I	Material science for Astrophysics	5
1	Introduction	7
1.1	From cold clouds to comets	9
1.2	Gas and Dust	14
1.2.1	The chemistry in star-forming regions	17
1.2.2	Energetic processing	23
1.3	This work	29
II	In the solid phase: on the icy grain mantles	37
2	Combined infrared and Raman study of solid CO	39
2.1	Searching for CO phase changes	40
2.2	Experimental methods	45
2.2.1	Thickness measurement	48
2.3	Results	54
2.3.1	Temperature experiments	54
2.3.2	Irradiation experiments	57
2.3.3	Increasing Thickness	60
2.4	Discussion	63
3	On the detection of solid deuterated water in astrophysical environments: constrains from laboratory experi-	

ments	67
3.1 Deuterated water in astrophysically relevant ices	68
3.2 Experimental methods	72
3.3 Results	77
3.3.1 Thermal processing of H ₂ O:HDO=1000:1 mixture	77
3.3.2 Thermal processing of D ₂ O:HDO=3:1 and H ₂ O:HDO=2:1 mixtures	79
3.3.3 Energetic processing	81
3.3.4 Other vibrational features in the 4.1 μm spectral range	87
3.4 Discussion	91

III Synthesis and desorption: the role of energetic processing **96**

4 Synthesis of formamide and isocyanic acid after ion irradiation of frozen gas mixtures	98
4.1 The role of energetic processing in the synthesis of pre-biotic molecules	99
4.2 Energetic processing	101
4.2.1 Previous experiments	101
4.2.2 Experimental apparatus	103
4.2.3 Results	106
4.3 Discussion	114
4.3.1 Pre- and proto-stellar regions	114
4.3.2 Comets	118
4.3.3 Astrobiological relevance of formamide	123
5 Infrared study on the thermal evolution of solid state formamide	126

5.1	From the solid-phase synthesis to the gas-phase detection	127
5.2	Experimental methods	132
5.3	Results	136
5.3.1	Pure formamide	136
5.3.2	Formamide in water	140
5.3.3	Formamide in a CO matrix	142
5.3.4	Irradiation of a $\text{N}_2:\text{CH}_4:\text{H}_2\text{O}=1:1:1$ mixture . . .	145
5.4	Discussion	149

IV From the solid-phase synthesis to the gas-phase detections 155

6	C_2O and C_3O in star-forming regions	157
6.1	Carbon chain oxides	158
6.2	Observations	161
6.2.1	Source sample	161
6.2.2	New observations	163
6.2.3	C_2O and C_3O abundances	170
6.3	Modelling	173
6.3.1	Model description	173
6.3.2	Chemical network	176
6.3.3	Results of the modeling	178
6.4	Experimental results	185
6.5	Discussion	191
7	Conclusions	197
7.1	Acknowledgements	214

Part I

**Material science for
Astrophysics**

Chapter 1

Introduction

The knowledge on the physical and chemical properties of astrophysical bodies, such as planets, comets, asteroids and meteorites, together with primordial matter in star-forming regions, derives from the comparison between astronomical observations and laboratory experiments and models that try to simulate their formation and the harsh conditions they experience in space. Modern technology allowed to build sensitive instruments that enabled scientist to acquire interesting data to spread light on the origins of planet Earth and to reconstruct the history of the entire Solar System. As an example, thanks to radiotelescopes and ground- and space-based radio infrared observatories, astronomers have found several young Sun-like stars in the Galaxy that allowed a better comprehension of the Solar System formation. Moreover, unique in-situ data about the matter on the surface of planets and other minor bodies are furnished by space probes. These data, together with typical laboratory analysis carried out on samples collected on Earth, during space missions or on analogues synthesised by simulating space conditions, are fundamental to understand how matter evolved from a crowded environment of simple gas and dust to the present Solar System. Finally, how life emerged on Earth and whether

life exists beyond Earth is a perpetual human query. Material Science, Astrochemistry and Astrobiology are scientific branches that make use of chemistry, physics, astronomy, biology and many other research fields with the aim to spread light on our origins.

1.1 From cold clouds to comets

Star formation takes place in the *interstellar medium (ISM)*, i.e., the space between stars in galaxies. The ISM is characterized by the presence of rarefied material. About 99% in mass is gas, mainly hydrogen. The remaining 1% is due to the presence of silicate and carbonaceous sub-micron dust grains. The ISM composition, temperature and density are highly variable. In particular, two main cold regions can be distinguished, according to temperature and density conditions: *diffuse cold clouds* and *dense molecular clouds*.

Diffuse cold clouds are formed by tenuous material ejected by stars at the end of their life, as examples, during Super-Novae explosions or fast winds of Asymptotic Giant Branch (AGB) stars. Typical temperatures are in the range 10-80 K and density ¹ between 0.1-1 cm⁻³. If there is enough material, the cooling of diffuse cold clouds determines the formation of *dense molecular clouds*. Here the temperature drops down to 10-50 K, while density increases up to 10⁴-10⁶ cm⁻³. It is in these regions that new stars form (e.g., Palla & Stahler 2002; Stahler & Palla 2005). According to their mass, young stellar objects (YSO) are classified in low-mass ($M < 2 M_{\odot}$), intermediate- ($2 \leq M \leq 6 M_{\odot}$) and high-mass ($M > 6-8 M_{\odot}$)² YSO (Strom et al. 1975; McKee & Ostriker 2007). Also, it is here that chemical and physical processes determine the formation of both astronomical simple and complex molecules.

¹in number of hydrogen atoms cm⁻³

² M_{\odot} is the Solar mass, equal to $\sim 1.98 \times 10^{30}$ kg

Sun-like star formation can be divided in five formation steps, as shown in Fig.1.1 (Caselli & Ceccarelli 2012):

1. Pre-stellar core
2. Protostellar envelope
3. Protoplanetary disk
4. Planetesimals
5. Planets

In the pre-stellar core formation phase, gravitational energy determines the collapse of a cold cloud of gas and dust. Matter accumulates toward the centre, and the low temperature causes gas-phase atoms and molecules to freeze-out on the dust grain surfaces, forming the so-called *icy grain mantles*. Despite the low temperature, hydrogen atoms possess mobility enough to scan the icy mantles and hydrogenate atoms and CO molecules, the most abundant species in cold molecular gas after H₂, forming H-rich species such as water, formaldehyde and methanol (see § 1.2.1).

During the protostellar envelope formation, gravitational energy is converted into radiation, so that the envelope around the central object, i.e. the future star, warms up. The higher temperature and the exposure to highly energetic charged particles and UV photons determine the formation of new molecular species within the icy grain mantles and eventually their partial sublimation, sputtering and photodesorption. Thus, new molecules might be injected in the gas phase where they can further react increasing the chemical complexity. During the collapse, a fraction of matter is ejected outside the central region as highly supersonic collimated jets and molecular outflows that interact with the surrounding matter and contribute to the sputtering of icy

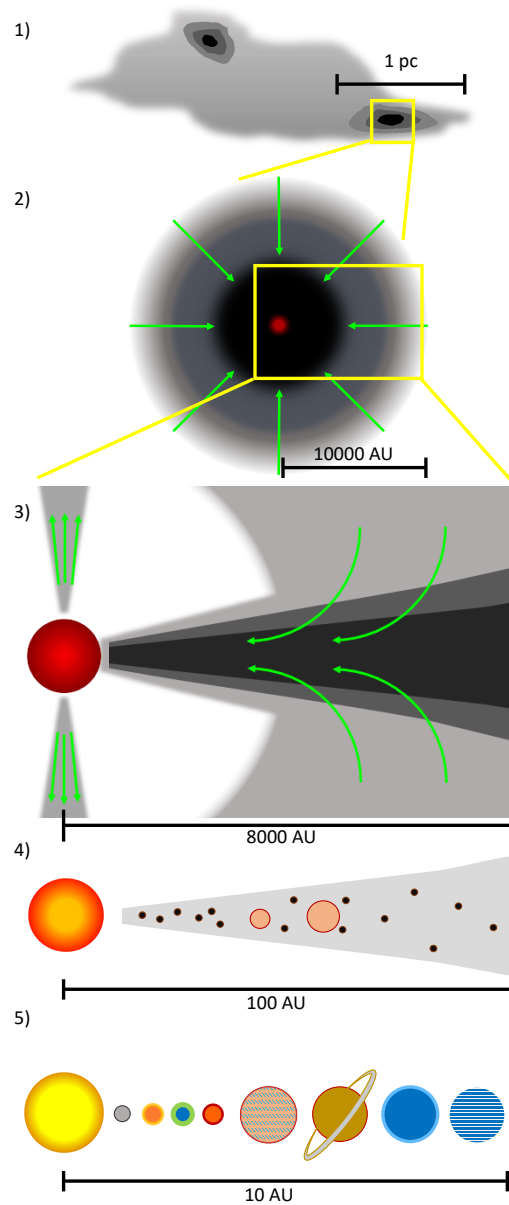


Figure 1.1: *Star-formation steps: 1) pre-stellar core in a cold cloud; 2) zoom on a protostellar envelope undergoing gravitational collapse; 3) within the envelope, a protoplanetary disk forms; 4) planetesimals formation takes place within the circumstellar disk; 5) formation of planets and other minor objects due to planetesimals accretion. Dimension scales are given in parsec, $1 \text{ pc} = 3.086 \times 10^{13} \text{ km}$ and astronomical units, $1 \text{ AU} = 1.496 \times 10^8 \text{ km}$.*

mantles. These processes inject molecules in the gas phase, allowing their detection by means of radiotelescopes.

In the protoplanetary disk formation, the envelope dissipates and a circumstellar disk appears. About 10^6 years are necessary up to this stage. Within the disk a temperature gradient is present. The hotter regions are those closer to the central objects, where further chemical reactions occur. The external regions are colder; temperature is low enough to allow gas-phase molecules to freeze-out again on dust grains, where molecules accreted during the prestellar phase may still be present. Then, planetesimal formation takes place within the circumstellar disk. Planetesimals are the building blocks of comets, asteroids and planets. They form when dust grains encounter each other and stick together to form larger agglomerates.

Finally, the further accretion of planetesimals determines the formation of planets (e.g., Pollack et al. 1996). In the crowded environment around them, the left over material forms minor bodies that bombard these objects. Falling on planet surfaces, comets and asteroids release their constituents, as it happened in the primitive Earth between 4.1 and 3.8 billion years ago.

It is generally accepted that during the planetesimal formation a fraction of the icy grain mantles remains trapped in these bodies. Thus, a link between the composition of interstellar matter and comets has been suggested (e.g., Greenberg 1982; Fresneau et al. 2017). An intriguing issue concerns the extent to which comets preserved the chemical composition of pre-solar matter versus the role of further chemical processes experienced in the latter stages (e.g., Bockelée-Morvan et al. 2000).

Thanks to observational facilities, such as radio telescopes and both ground- or space-based infrared telescopes, astronomers have been able to detect volatiles in cometary comae (e.g., Combes et al. 1988; Irvine

et al. 1996; Dutrey et al. 1996; Mumma et al. 1996; Lis et al. 1997; Woodney et al. 1997; Crovisier 1997; Bockelée-Morvan et al. 2000). By comparing the species detected with those observed toward star-forming regions in space, it has been possible not only to obtain precious insights into the origins of cometary materials, but also on the evolution of matter from the presolar cloud to the Solar System planet formation.

Interesting information has been obtained by the direct analysis of meteorites. As an example, Moynier et al. (2007) have been able to estimate the age of the Solar System (found to be 4.568 billion years old) by analysing the chromium isotopic composition in carbonaceous chondrites, i.e., meteorites composed by primitive cosmic sediments named chondrules (silicate droplets) and Ca-Al and Fe-Ni-metal inclusions embedded in a fine grained matrix rich in organic material (Lauretta et al. 2006; Pizzarello et al. 2006; Lantz et al. 2017).

1.2 Gas and Dust

As said in the previous section, the ISM is mainly composed by gas, about 75% in mass being hydrogen. Helium is the second most abundant element, being about 20% in mass. Other heavier elements contribute to the remaining 5%. Generally, neutral atomic and ionized hydrogen are found in diffuse cold clouds, while molecular hydrogen is found in dense molecular clouds.

Despite the harsh conditions, since the first detections reported in the late '30s and '40s (e.g., Swings and Rosenfeld 1937; McKellar 1940; Douglas and Herzberg 1941), to date about 200 molecules³ have been detected in the gas phase of the ISM. Their detection has been allowed by radiotelescopes, i.e., parabolic antennas that allow astronomers to acquire spectra in the frequency range of the electromagnetic spectrum where molecular rotational transitions fall, so that it is possible to obtain qualitative and quantitative information about molecules present in the observed sources.

Despite the lower abundance w.r.t.⁴ gas-phase matter, dust is important in the evolution of the ISM and star formation. In fact, the condensation of metals to form planetesimal is considered the starting point of planet formation (e.g., Lindblad 1935). Also, the accretion of the most abundant elements and molecules onto the grain surfaces has been used by van de Hulst (1946) to explain the formation of water, methane and ammonia as interstellar icy grain mantles. Interstellar dust is composed by nonvolatile silicate (e.g., $\text{Mg}_{2x}\text{Fe}_{2-2x}\text{SiO}_4$, olivines

³<https://www.astro.uni-koeln.de/cdms/molecules>

⁴with respect to

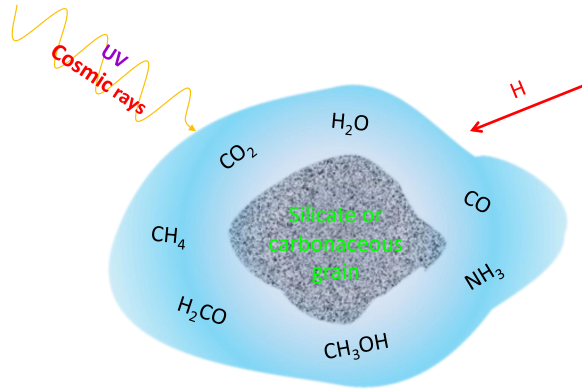


Figure 1.2: *Dust grain covered by the icy mantle, a layer of condensed volatile species. H atoms may reach the surface, stick on it and react with frozen molecules (see § 1.2.1). Also, the grains are exposed to UV photons and low-energy cosmic rays that modify the physical structure and chemical composition of icy mantles (see § 1.2.2).*

and $\text{Mg}_x\text{Fe}_{1-x}\text{SiO}_3$, pyroxenes) or carbonaceous compounds including polycyclic aromatic hydrocarbons (PAHs). Each grain is covered by a layer of condensed molecules, mainly water and carbon monoxide and other species in lower abundance that form the icy mantles.

Although interstellar ice models propose that their compounds are mixed together, recent observations suggest that interstellar ices are best represented by a layered ice model (e.g., Fraser et al. 2004; Palumbo 2006) (see Table 1.1 for a list of solid-phase molecules detected toward star forming regions, Boogert et al. 2015; Yamamoto 2014).

Water is the most abundant observed solid-phase molecule in star-forming regions. Its presence has been reported for the first time toward the Orion Nebula by Gillett and Forrest (1973). Using the University of Minnesota-UCDS 60-inch infrared telescope at Mount Lemmon Observatory (Arizona, USA), they have been able to detect the $3.1\mu\text{m}$ OH stretching mode band of water. To date, several other solid-phase species have been detected and many other are thought to be present

Table 1.1: *The abundance of solid-phase molecules detected toward low- and high-mass young stellar objects and in background stars with respect to water (Boogert et al. 2015).*

Species	Abundance w.r.t. H ₂ O
H ₂ O	100
CO	<3-85
CO ₂	11-50
CH ₃ OH	<1-31
NH ₃	3-10
CH ₄	1-11
H ₂ CO	2-7
XCN	<0.1-1.1
OCS	0.03-1.6
SO ₂	0.3-0.8

in lower abundance within the icy mantles, but due to detection limits of currently available infrared telescopes they cannot be detected.

In Table 1.1 the abundances of the main molecules trapped in icy grain mantles observed toward young stellar objects w.r.t. water column density are reported.

1.2.1 The chemistry in star-forming regions

Star-forming regions host hundreds gas-phase molecular species, and as already said, radiotelescopes allow their detection. On the other hand, to obtain information on solid-phase molecules it is needed to observe their vibrational transitions, thus infrared telescopes are needed. In Fig. 1.3 an example of a typical infrared spectrum acquired toward a high-mass YSO is shown (from Boogert et al. 2015). Labels indicate the known vibrational features. The attributions mainly derive from the comparison between laboratory experiments in which icy grain mantles analogues are synthesised and analysed by means of infrared spectroscopy (see the dashed line in the figure).

One of the main open issues in astrochemistry is to understand what are the chemical and physical processes that contribute to the formation of both gas-phase and solid-phase molecules observed in star-forming regions. Both gas-phase reactions and solid-phase processes that occur on the surface of dust grains have to be taken into account.

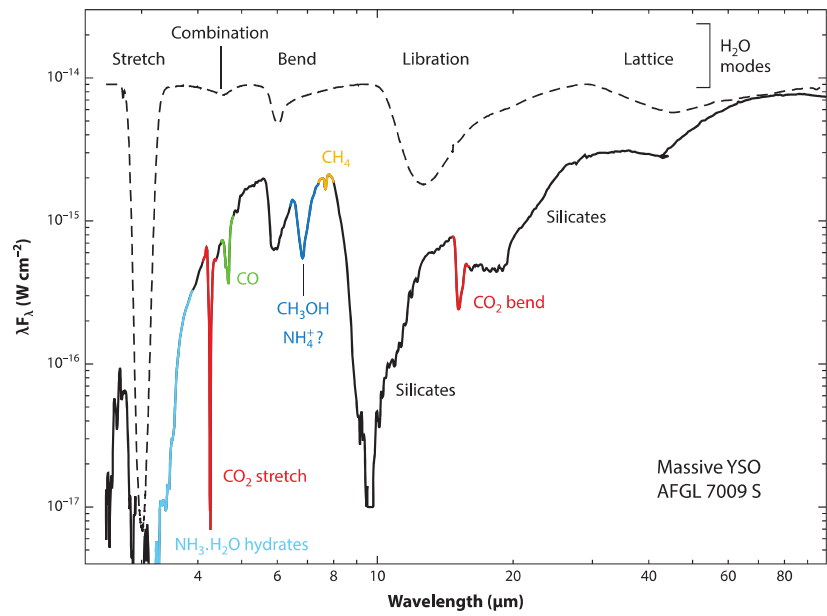


Figure 1.3: Infrared spectrum acquired toward the massive Young Stellar Object AFGL 7009S (solid line) and infrared spectrum of water ice spheres at 10 K (dashed line) from Boogert et al. (2015).

Gas-phase chemistry

To study the formation of gas-phase molecules, astrochemists developed several models with the aim to simulate the typical physical and chemical parameters found in these regions, trying to predict the molecular abundance variations as a function of time. In general, to run simulations a list of initial elemental abundances is needed, together with a network of gas-phase reactions and their rate coefficients, given by the Arrhenius formula: $k = A(T)\exp(-E_a/k_B T)$, where $A(T)$ is a pre-exponential factor, a weak function of the temperature that depends on the shape of the reaction potential surface, E_a is the activation energy, k_B is the Boltzmann constant and T is the gas kinetic temperature. The main reactions taking place in the gas phase of star forming regions can be divided into six classes, and they are reported in Table 1.2. See Chapter 3 in Yamamoto (2014) for more details about gas-phase reactions.

In simulations, the main uncertainties are due to poorly known physical parameters in the region to be modelled (e.g. the cloud density, the temperature and the cosmic-ray ionization rate) and in the rate coefficients of many reactions. To date, several astrochemical models exist, and thanks to the constraints given by observational, theoretical and experimental data (e.g., Loison et al. 2014, 2016) their performances in reproducing the observed abundances of many species are improving. In Chapter 6 other details about astrochemical models and gas-phase reactions are given.

Table 1.2: Classes of gas-phase reactions in star forming regions and their typical rate coefficients k as reported by Caselli (2005).

Reaction	Process	Rate coefficient
Ion-molecule	$A^+ + B \rightarrow C^+ + D$	$\sim 10^{-9} \text{ cm}^3 \text{ s}^{-1}$
Dissociative recombination	$AB^+ + e^- \rightarrow A + B$	$\sim 10^{-6} \text{ cm}^3 \text{ s}^{-1}$
Radiative association	$A + B \rightarrow AB + h\nu$	$\sim 10^{-16} - 10^{-9} \text{ cm}^3 \text{ s}^{-1}$
Neutral-neutral	$A + B \rightarrow C + D$	$\sim 10^{-12} - 10^{-10} \text{ cm}^3 \text{ s}^{-1}$
Photodissociation	$AB + h\nu \rightarrow A + B$	$\sim 10^{-9} \text{ s}^{-1}$
Charge-transfer	$A^+ + B \rightarrow A + B^+$	$\sim 10^{-9} \text{ cm}^3 \text{ s}^{-1}$

Solid-phase chemistry

Together with gas-phase reactions, dust grain cold surfaces play a fundamental role in the formation of molecules. As an example, the most abundant molecule in these regions, i.e. H_2 , is formed on the cold grain surfaces (e.g., Gould & Salpeter 1963; Hollenbach & Salpeter 1971; Pirronello et al. 1999; Mennella et al. 2012). Furthermore, atoms and molecules accrete on dust grain surfaces, allowing chemical reactions that increase the icy mantles chemical complexity.

Due to the low temperature, gas-phase species that collide with dust grains are adsorbed on their cold surfaces, in the so-called *sticking* process. There are two mechanisms of interaction between the grain surface and the guest species: *physisorption*, via weak van der Waals forces or *chemisorption*, via valence forces. However, chemisorption has a potential barrier, and it is generally assumed that in cold sources the sticking occurs via physisorption onto the surface potential minima, known as *binding sites*. Once on the surface, the guest species may desorb by overcoming an energy barrier (E_d in Fig.1.4), either by sublimation (only for very light species) or by nonthermal mechanisms, such as cosmic-ray bombardment by heavy nuclei (e.g., Léger et al. 1985; Ivlev et al. 2015), energy released by chemical surface reactions (e.g., Willacy & Millar 1998). Also, photodesorption is relevant if the amount of UV photons that reach the grains is enough, such as in the so-called photodissociation regions (PDR) or diffuse clouds (e.g., Paardekooper et al. 2016).

As the guest species are adsorbed on the grain surfaces, icy mantles are formed and a complex surface chemistry begins. Surface reactions can be divided into three classes: *Langmuir-Hinshelwood*, *Eley-Rideal* and the *hot atom*. All processes are schematically shown in Fig. 1.4. In

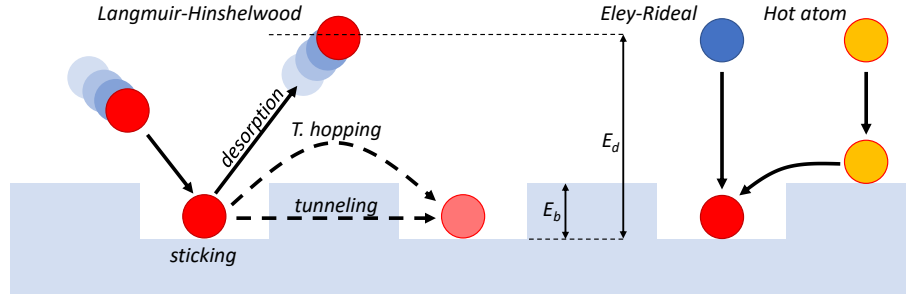
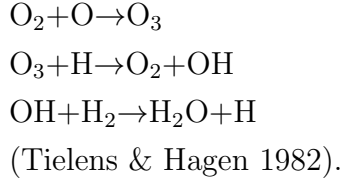


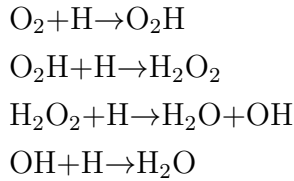
Figure 1.4: Mechanism of accretion, desorption or diffusion and reaction of guest atoms or molecules on the cold dust grain surfaces; adapted from Fig. 9 by Herbst & van Dishoeck (2009).

the *Langmuir-Hinshelwood* mechanism, diffusion takes place by tunneling or thermal hopping between two adjacent binding sites, if the guest possesses the energy E_b . When two guests encounter each other in the same binding site they can react, releasing the exceeding energy to the grain. In the *Eley-Rideal* mechanism, reactions occur between a guest that has been previously adsorbed in a binding site and a gas-phase species that lands on it. Finally, in the *hot atom* mechanism, a gas-phase species lands on a random point of the grain surface and scans it before thermalisation, with the probability to find an adsorbate in a binding site and react with it (Herbst & van Dishoeck 2009).

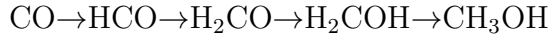
Being hydrogen the lighter and most abundant element in space, its reaction with species that are already on the icy grain mantles is common, and it is called *hydrogenation*. Once H atoms accrete on the surface, they quickly diffuse and react (e.g., Accolla et al. 2011). It has been proposed that water ice is produced directly on the grains surface by atomic oxygen hydrogenation via the reaction $O \rightarrow OH \rightarrow H_2O$ (e.g., Herbst & van Dishoeck 2009), or via:



Also, another pathway has been proposed and experimentally confirmed by Miyauchi et al. (2008):



Also carbon monoxide, that is formed by gas-phase reactions, accretes onto the grain surfaces and reacts with H atoms up to the formation of methanol, as suggested in experimental works by Watanabe & Kouchi (2002) and Fuchs et al. (2009):



1.2.2 Energetic processing

In both diffuse cold clouds and dense molecular clouds, icy grain mantles are bombarded by UV photons and low-energy cosmic rays, i.e. energetic charged particles, in a phenomenon known as *energetic processing*. In dense molecular clouds, UV photons typically have energies less than 13.6 eV and flux in the range 2×10^3 - 3×10^4 photons $\text{cm}^{-2} \text{s}^{-1}$ (Prasad & Tarafdar 1983; Mennella et al. 2003; Shen et al. 2004) and

they only penetrate the outer icy grain mantle monolayers. Galactic cosmic rays consist of about 98% H^+ and 2% He^{2+} . At energy around 1 MeV, the flux is in the range 1-10 ions $\text{cm}^{-2} \text{s}^{-1}$ (Strazzulla & Johnson 1991; Mennella et al. 2003; Indriolo & McCall 2012; Islam et al. 2014), and they can penetrate the entire grain. Several processes may be induced, such as desorption and sputtering, structural and phase changes, fragmentation (radiolysis) followed by chemical reactions to form new molecules and radicals (e.g., Palumbo et al. 2016; Rothard et al. 2017). These effects are due to the transfer of energy and momentum between the impinging particle and the condensed matter. The collision between the particle and the target atoms can be elastic or inelastic. In elastic collisions, the particle transfers a fraction of its momentum to the target nuclei. This process, also called *nuclear stopping*, may lead to a cascade of recoiling target atoms and sputtering from the surface. During inelastic collisions, the target electrons can be scattered by the projectile's Coulomb potential and the atom can be excited or ionised. This process (i.e., electronic stopping) may lead to the ejection of secondary electrons and photons. Electrons from primary ionisation travel through the medium and may suffer elastic or inelastic scattering by target atoms and electrons, respectively. The latter inelastic process may lead to further ionisation and creation of secondary electrons. The ion trajectory in the medium result in a zone of high ionisation density. The overall process require about 10^{-14} s. More details on the physical process have been given by Rothard et al. (2017).

A pathway to the formation of complex species

Most of the knowledge about the effects of energetic processing on interstellar ices is based on laboratory experiments in which energetic ions or electrons (keV-MeV) or UV photons impact frozen mixtures that are thought to be representative of icy grain mantles or cometary

surfaces, in order to simulate the effects induced by low-energy cosmic rays, UV-photons and solar/stellar wind. The chemistry induced in the processed material is due to the fact that both ions and UV photons cause the breaking of molecular bonds and the production of radicals and molecular fragments that recombine, forming species that were not present in the deposited sample that increase its chemical complexity. Both volatile and less volatile species are produced. Also, if carbon-bearing species are deposited in the original mixture, a refractory residue is formed (e.g., Strazzulla et al. 1983; Moore et al. 1983; Gerakines et al. 1996; Palumbo et al. 2016). Laboratory experiments have shown that the energetic processing of icy grain mantles has a role not only in the formation of simple species, but also in the formation of so-called *Astrophysical* or *Interstellar Complex Organic Molecules* (ACOMs or ICOMs, e.g., Caselli & Ceccarelli 2012), i.e., molecules that contain more than 5 atoms.

Also prebiotic species are synthesised, i.e., molecules that could have been involved in the early processes that led to the origin of life on Earth (e.g., Saladino et al. 2005; Bennett & Kaiser 2007; Fedoseev et al. 2015). To explain the emergence of life, two main theories have been proposed: the *endogenous* synthesis, supported by the famous Miller-Urey experiment (Miller 1953), according to which organic molecules have been synthesised on Earth from simple inorganic precursors (water, methane, ammonia and hydrogen) and the *exogenous delivery* due to comets and meteorites impacts on the primitive Earth during the *Late Heavy Bombardment*, between 4.1 and 3.8 billion years ago (e.g., Chyba and Sagan 1992). In fact, both objects contain extraterrestrial molecules that may have been synthesised after the energetic processing of pristine pre-solar simple matter.

Generally, laboratory experiments with astrophysical applications require complex experimental set ups that include one (or more) radia-

tion sources, such as UV lamps (e.g., Grim et al. 1989; Bernstein et al. 2002; Henderson & Gudipati 2015; Leto & Baratta 2003), electron guns or ion accelerators (e.g., Strazzulla et al. 2001; Hudson et al. 2001; Famá et al. 2009; Bennett et al. 2007; Abdulgalil et al. 2013) that are able to cover a wide range of energies up to a few hundreds keV. Recently, also synchrotron radiation has been used to investigate the effect induced by vacuum ultraviolet (VUV) photoabsorption (e.g., Mason et al. 2006; Sivaraman et al. 2014). The irradiation source is connected to high vacuum ($P \leq 10^{-7}$ mbar) or ultra high vacuum chamber ($P \leq 10^{-9}$ mbar) that is equipped with nitrogen or helium cryostat, devices that allow to go down in temperature to about 80 K and 10 K, respectively. The cryostat is in thermal contact with a substrate where the sample is deposited. In the most common approach, the deposition is carried out by introducing a pure gas species or a mixture that condenses on the cold substrate, forming a frozen layer on top of it. Usually, by means of a resistor, it is also possible to increase the cryostat temperature in order to investigate the thermal evolution and the desorption of the sample (see Chapter 5). Once the deposition is completed, the radiation source is turned on and the sample irradiation begins. The effects induced on the sample are investigated by analytical techniques, such as infrared spectroscopy or mass spectrometry of the ejected particles. Other complementary and emerging techniques are also used (e.g., Alodi et al. 2013). A schematic drawing of an experimental set up to deposit, irradiate and analyse frozen samples is shown in Fig. 1.5.

Due to the fact that infrared telescopes allow the detection of solid-phase molecules in star-forming regions, infrared spectroscopy is the most diffuse analytical technique to study icy grain mantles analogues synthesised in laboratory. In fact, infrared spectroscopy is a powerful tool that allows in-situ analysis of the samples to obtain information not only on molecular groups and specific molecules, but also on their

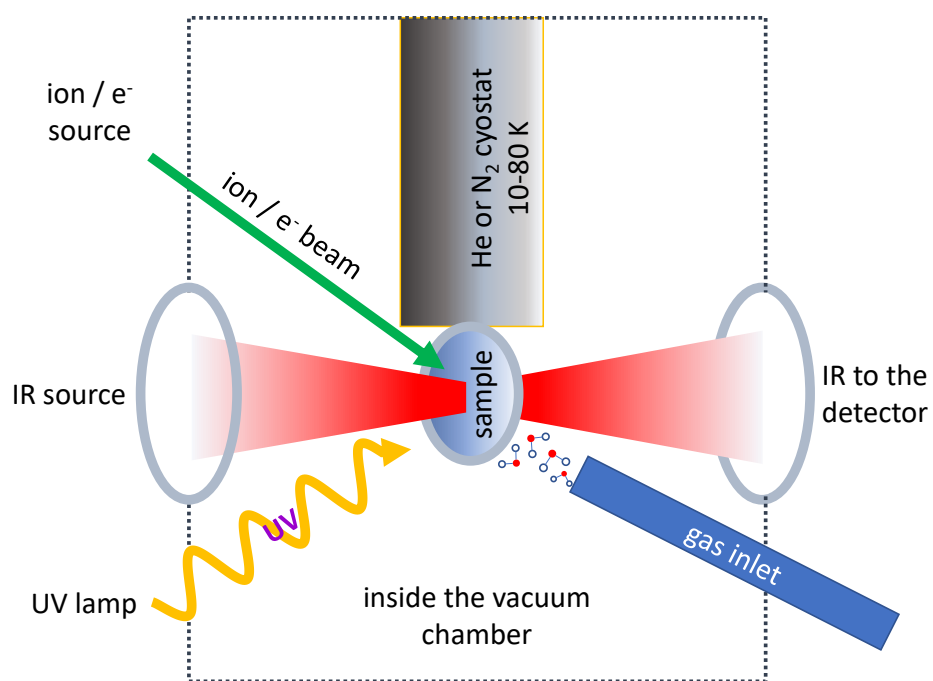


Figure 1.5: An experimental laboratory set up to deposit, irradiate and analyse frozen samples by means of IR spectroscopy.

physical structure. Thus, together with the chemical composition of the irradiated sample, it is possible to study whether the energetic processing induces structural changes, such as compaction (e.g., Palumbo 2006; Dartois et al. 2013; Raut et al. 2007a), or phase changes, such as amorphization of crystalline samples (e.g., Baratta et al. 1991; Dartois et al. 2015). Comparing these data with spectra collected by infrared telescopes helps to reveal the physical-chemical structure of icy grain mantles.

1.3 This work

In the last decades, the role of many laboratories for experimental astrophysics has been fundamental to interpret astronomical data and, as an example, to spread light on the molecular synthesis reproducing the conditions under which astrochemistry occurs in space or on planetary surfaces. The results presented in this work have been obtained during laboratory experiments that have been performed at the *Laboratorio di Astrofisica Sperimentale* (LAsp) at *INAF-Osservatorio Astrofisico di Catania*. The laboratory has been active in Catania since the '80s, and it is equipped with high vacuum chambers, facilities for the deposition of films at low temperature (down to 10 K), many spectrometers in the range from 190 nm up to 200 μm , and Raman spectrographs. Also, Lyman-alpha and ion irradiation experiments are performed, in order to simulate the effect of UV photons and cosmic rays on icy grain mantles and cometary surfaces.

This thesis reports laboratory experiments that have been performed in order to interpret astronomical observation acquired toward star-forming regions where icy grain mantles are found. Also, constrains and suggestions for future observations are given. After the introduction, this work is divided into four parts: Part II - In the solid phase: on the icy grain mantles; Part III - Synthesis and desorption: the role of energetic processing; Part IV - From the solid-phase synthesis to the gas-phase detections. For each chapter, an introduction explains the aims of the work, and the experimental methods and set up are given in details.

In particular, in Part II we report about several experiments that

have been performed in order to investigate structural and phase changes induced by thermal and energetic processing on the astrophysical relevant species carbon monoxide (Chapter 2) and deuterated water (Chapter 3).

In part III we report about isocyanic acid and formamide synthesis (Chapter 4), thermal evolution and desorption (Chapter 5) after ion irradiation of icy grain mantles and cometary surface analogues. Formamide has been detected toward star-forming regions and it is considered a prebiotic molecule. Experiments have shown that formamide could have been a potential source of amino and nucleic acids in the primordial Earth conditions.

Finally, in Part IV we report our contribute in the debate about the growth of simple molecules to explain the formation of more complex species observed in the ISM. The results have been obtained in collaboration with astronomers from the Observatoire de Grenoble (France). C_2O and C_3O are two simple species that have been detected in the gas phase toward several star-forming regions. Laboratory experiments have shown that they are formed after the energetic processing of icy grain mantles analogues (e.g., Palumbo et al. 2008). To better understand the presence of both molecules toward these sources, we performed a work in which observational data, laboratory experiments and gas-phase modeling are combined.

The following sections briefly introduce each chapter.

Chapter 2: Combined infrared and Raman spectroscopy of solid CO

Based on Urso, R. G., Scirè, C., Baratta, G. A., Compagnini, G. & Palumbo, M. E. 2016, *Astronomy & Astrophysics*, 594, A80

Knowledge about the composition and structure of interstellar ices is mainly based on the comparison between astronomical and laboratory spectra of astrophysical ice analogues. Carbon monoxide is one of the main components of the icy mantles of dust grains in the interstellar medium. Because of its relevance, several authors have studied the spectral properties of solid CO both pure and in mixtures. In this chapter we report about a study on the profile (shape, width, peak position) of the solid CO band centered at about 2140 cm^{-1} at low temperature, during warm up, and after ion irradiation to search for a structural variation of the ice sample. We also report on the appearance of the longitudinal optical-transverse optical (LO-TO) splitting in the infrared spectra of CO films to understand if this phenomenon can be related to a phase change. We studied the profile of the 2140 cm^{-1} band of solid CO by means of infrared and Raman spectroscopy. We used a free web interface that we developed that allows us to calculate the refractive index of the sample to measure the thickness of the film. The profile of the fundamental band of solid CO obtained with infrared and Raman spectroscopy does not show any relevant modification after warm up or ion bombardment in the dose range investigated. We explain that the LO-TO splitting is not connected to a structural variation of the film. Ion irradiation causes the formation of new molecular species. Raman spectroscopy allowed us to detect, among other bands, a band centered at 1817 cm^{-1} that has been attributed to the infrared inactive species

C₂ and a band centered at 1767 cm⁻¹ that remains unidentified.

Chapter 3: On the detection of deuterated water in icy grain mantles: constrains from laboratory experiments

Based on Urso, R. G., Palumbo, M. E. et al. in prep.

The comparison between astronomical spectra and laboratory experiments is fundamental to spread light on the structure and composition of ices in interstellar dense molecular clouds and on Solar System bodies. Infrared spectra acquired toward several star-forming regions revealed the presence of water as the most abundant observed constituent of icy grain mantles. Several attempts have been made to investigate the presence of solid-phase water isotopologues in space. In particular, the detection of the O-D stretching mode band at 4.1 μm due to the presence of D₂O and HDO within icy grain mantles is still under debate. In fact, available spectra acquired by means of infrared space telescopes are not detailed enough to confirm the presence and abundance of both species. According to current models, the HDO/H₂O ratio in icy grain mantles depends on the grain temperature at the time of H₂O formation. In this chapter, we report about experiments we performed to study the O-D stretching mode band in solid mixtures that simulate astrophysical relevant ices containing water and deuterated water in various ratios deposited at 17 K. During the experiments, samples have been either heated or irradiated with energetic ions (200 keV H⁺) in order to study the effects induced by both thermal and energetic processing. Our results provide some constrains on the detection of the 4.1 μm band in astronomical environments.

Chapter 4: Synthesis of formamide and isocyanic acid after ion irradiation of frozen gas mixtures

Formamide (NH_2CHO) and isocyanic acid (HNCO) have been observed as gaseous species in several astronomical environments such as cometary comae and pre- and protostellar objects. A debate is open on the formation route of those molecules, in particular if they are formed by chemical reactions in the gas phase and/or on grains. In this latter case it is relevant to understand if the formation occurs through surface reactions or is induced by energetic processing. We present arguments that support the formation of formamide in the solid phase by cosmic-ion-induced energetic processing of ices present as mantles of interstellar grains and on comets. Formamide, along with other molecules, are expelled in the gas phase when the physical parameters are appropriate to induce the desorption of ices. We have performed several laboratory experiments in which ice mixtures ($\text{H}_2\text{O}:\text{CH}_4:\text{N}_2$, $\text{H}_2\text{O}:\text{CH}_4:\text{NH}_3$, and $\text{CH}_3\text{OH}:\text{N}_2$) were bombarded with energetic (30-200 keV) ions (H^+ or He^+). FTIR spectroscopy was performed before, during, and after ion bombardment. In particular, the formation of HNCO and NH_2CHO was measured quantitatively. Energetic processing of ice can quantitatively reproduce the amount of NH_2HCO observed in cometary comae and in many circumstellar regions. HNCO is also formed, but additional formation mechanisms are requested to quantitatively account for the astronomical observations. We suggest that energetic processing of ices in the pre- and proto-stellar regions and in comets is the main mechanism to produce formamide, which, once it is released in the gas phase because of desorption of ices, is observed in the gas phase in these astrophysical environments.

Chapter 5: Infrared study on the thermal evolution of solid state formamide

Based on Urso, R. G., Scirè, C., Baratta, G. A., Brucato, J. R., Compagnini, G., Kaňuchová, Z., Palumbo, M. E. & Strazzulla, G. 2017, *Physical Chemistry Chemical Physics*, 19, 21759

Laboratory experiments have shown that the energetic processing, i.e. ion bombardment and UV photolysis, of interstellar grain mantles and cometary surfaces is efficient in the production of formamide. To explain its presence in the gas phase in these astrophysical environments, a desorption mechanism has to be taken into account. In this chapter we show experimental results on the thermal evolution of formamide when deposited at 17 K as pure and in mixture with water or carbon monoxide. In these samples, we observed formamide desorption at 220 K. Moreover, we discuss its synthesis in a mixture containing molecular nitrogen, methane and water ($\text{N}_2:\text{CH}_4:\text{H}_2\text{O}$) deposited at 17 K and bombarded with 200 keV H^+ . Heating the sample, we observed that the newly formed formamide remains trapped in the refractory residue produced after the ion bombardment up to 296 K. To analyse the samples we used Fourier transform-infrared spectroscopy (FT-IR) that allowed us to study the infrared spectra between the deposition and the complete desorption of formamide. Here we discuss the experimental results in view of their astrophysical relevance.

Chapter 6: C₂O and C₃O in star-forming regions

Based on Urso, R. G., Palumbo, M. E., Ceccarelli, C. et al. in prep.

C₂O and C₃O, namely dicarbon monoxide and tricarbon monoxide, belong to the carbon chain oxides family. Both molecules have been detected in the gas phase toward several star-forming regions. Among them, in TMC-1 C₂O and C₃O fractional abundances with respect to H₂ have been estimated to be about 6×10^{-11} (Ohishi et al. 1991) and 1.4×10^{-10} Brown et al. (1985). To explain these abundances, ion-molecule gas-phase reactions have been invoked. On the other hand, laboratory experiments have shown that carbon chain oxides are formed after ion bombardment and UV photolysis of CO-rich solid mixtures. Therefore, it has been proposed that they are formed in the solid phase in dense molecular clouds after cosmic ion irradiation of CO-rich icy grain mantles and released in the gas phase after their desorption. Our aim is to contribute to the understanding of the role of both gas-phase reactions and energetic processing in the formation of carbon chain oxides. In this chapter, we present observations obtained with the 30 m IRAM and 32 m IRA-Noto telescopes, the results of a gas-phase model that simulate C₂O and C₃O formation and destruction and laboratory experiments in which both molecules are produced after energetic processing of icy grain mantles analogues. The results show that the observed fractional abundances are due to the energetic processing of CO-rich icy grain mantles and their subsequent desorption because of non thermal processes.

Part II

In the solid phase: on the icy
grain mantles

Chapter 2

Combined infrared and Raman study of solid CO

Based on Urso, R. G., Scirè, C., Baratta, G. A., Compagnini, G. & Palumbo, M. E. 2016, *Astronomy & Astrophysics*, 594, A80

2.1 Searching for CO phase changes

After molecular hydrogen, carbon monoxide is the most abundant molecule in space. The first detection of this molecule in the gas phase of the interstellar medium (ISM) was reported by Wilson et al. (1970). Infrared observations have shown the presence of solid CO in quiescent molecular clouds and in both low-mass and high-mass star-forming regions because this molecule, together with water, is one of the main components of the icy mantles of dust grains (e.g., Boogert et al. 2015). Because of the relevance of CO in astrophysics, several laboratories have been involved in the study of this molecule and its spectral properties in astrophysical ices analogues (e.g., Sandford et al. 1988; Tielens et al. 1991; Palumbo & Strazzulla 1993; Quirico & Schmitt 1997; Dartois et al. 2006; Palumbo et al. 2006; Cuppen et al. 2011).

As discussed in detail by Quirico & Schmitt (1997), two main experimental approaches are used: direct deposition on a single window (thin-film technique) and crystal films growth from the liquid phase in a closed cell. The thin-film technique has the advantage that films with good optical quality and well-known thickness can be obtained. On the other hand, only a limited range of temperature can be investigated owing to sample sublimation since it is in direct contact with the chamber vacuum; also a limited range of thicknesses can be investigated (less than few micrometers) making it difficult to study weak absorption features. The closed cell technique allows crystals to be grown from the liquid in a closed cryogenic cell under thermodynamical equilibrium. This allows cm-thick samples to grow with good optical and crystal qualities and it is not possible to form phases outside the thermodynamical equilibrium (e.g., to obtain amorphous solids). Closed cell technique studies have shown that CO has four different phases

(namely α -, β -, γ -, and ϵ - CO), a phase transition occurs at 61.6 K between the α - phase (the coldest one) to the β - phase, and that CO melting point is at 68.14 K (e.g., Löwen et al. 1990; Quirico & Schmitt 1997). When deposited following the thin-film technique, CO sublimate at about 30 K (e.g., Collings et al. 2004), which is well below the α - β - phase transition temperature.

The profile of the CO stretching mode in pure ice samples shows two features at about 2138 and 2142 cm^{-1} known as the transverse optical (TO) and the longitudinal optical (LO) modes (e.g., Chang et al. 1988; Palumbo et al. 2006). Both these features can be observed when IR spectra are taken in reflection-absorption IR spectroscopy (RAIRS) and oblique transmittance, while only the TO mode is observed in transmittance spectra taken at normal incidence. As discussed by Palumbo et al. (2006) the presence of the LO-TO splitting is not attributable to the presence of crystalline CO.

Recently, an interesting phenomenon has been investigated, which is the appearance of a spontaneous electric field due to dipole orientation within thin films of dipolar molecules. Materials that exhibit this behavior are called spontelectric (from spontaneously electrical). Using RAIRS, Lasne et al. (2015) studied the Stark shift created by the spontelectric field in vibrational frequencies of solid CO. They measured the LO-TO splitting to determine the values of the spontelectric field as a function of film deposition temperature.

In recent decades, several experimental investigations have focused on astrophysical relevant molecules, such as H_2O , CO_2 , CH_3OH , CH_3CN , and CH_3OCHO . Many of these experiments were meant to study the profile (i.e., shape, width, and peak position) of IR bands at different temperatures in pure ices and in mixtures. Laboratory spectra show that during warm up the profile of IR bands change. These changes can be attributed to a transition between a disordered phase to a much or-

dered one, i.e., an amorphous to crystalline transition. Some examples are reported by Hudgins et al. (1993), Palumbo et al. (1999), Moore et al. (2010), Abdulgalil et al. (2013), and Modica & Palumbo (2010). Bossa et al. (2012) reported about the thermal processing of porous amorphous solid water. They observed that between 20 and 120 K the ice undergoes a thickness decrease that they attribute to a phase transition to a nonporous and more compact structure of the ice.

Other studies have focused on the effects of energetic processing (i.e., ion bombardment and UV photolysis) on the structure and morphology of ices. As an example, on the basis of laboratory experiments, it has been shown that polycrystalline water ice is converted to amorphous ice after energetic processing (e.g., Baratta et al. 1991; Moore & Hudson 1992; Leto & Baratta 2003; Dartois et al. 2015). Furthermore, energetic processing also causes the conversion of porous amorphous water to compact amorphous water (e.g., Palumbo 2006; Raut et al. 2007a; Palumbo et al. 2010; Dartois et al. 2013) at 10-20 K.

Also some attempts have been made to look for a phase change of solid CO, both pure and in solid matrices, by studying its infrared spectrum (Maki 1961; Nealand 1985; Sandford et al. 1988; Loewenschuss et al. 1997). Katz et al. (1984) reported about a Raman scattering experiment of solid CO placed in a diamond cell and subjected to variation in temperature and pressure. Looking at the feature of the CO stretching mode, they identified four structures named α -, β -, γ -, and ϵ - CO, each showing a different profile of the stretching-mode feature.

Fuchs et al. (2006) reported on the change in the heights, widths, and position of the ^{13}CO stretching vibrational band by means of RAIRS spectroscopy during a temperature programmed desorption (TPD) experiment. At low temperatures (18.5 K) these authors observed a single peak at 2096 cm^{-1} due to amorphous ^{13}CO . Raising the temperature to 27.5 K, a peak centered at 2095.1 cm^{-1} appears and they attributed it to

the α -crystalline LO component. They concluded that these variations are due to a phase change from amorphous to crystalline ice at close to the desorption temperature. Studying the effect of photodesorption in CO ices, Öberg et al. (2009) reported that the CO photodesorption yield decreases, thereby raising the ice temperature from 15 K to 27 K. They carried out a RAIRS experiment that shows a change in the CO band profile between 15 K and 27 K. They concluded that because the annealing determines the formation of a more compact ice, its structure, rather than the temperature, affects the photodesorption yield.

Recently, Munõz Caro et al. (2016) reported on some experiments they carried out to evaluate if there is a connection between the structure and photodesorption rate of solid CO by means of IR spectroscopy, vacuum-UV (VUV) spectroscopy, and TPD. They observed that the photodesorption yield linearly decreases with the deposition temperature of CO from 7 to 20 K, but they do not attribute this decrease to a variation in its morphology toward a crystalline solid.

To extend previous work, in this article we present new laboratory experiments on solid CO. Both infrared and Raman spectroscopy are used to analyze the samples. These are two powerful and complementary tools to study the physical and chemical properties of frozen samples. By means of infrared spectroscopy it is possible to identify molecular groups and specific molecules. Raman spectroscopy gives further information on the structural properties of the samples and it is often used to study the effects of ion induced lattice damage in carbonaceous solids (e.g., Elman et al. 1981; Strazzulla & Baratta 1992; Baratta et al. 1996; Kalish et al. 1999; Strazzulla et al. 2001; Costantini et al. 2002). The main purpose of this work is to verify whether it is possible to observe a structural variation in solid CO during warm up and after ion bombardment. The article is organized as follows: the experimental methods are described in §2.2, the results are presented

in §2.3, and a discussion is given in §2.4.

2.2 Experimental methods

Experiments were performed in the Laboratory for Experimental Astrophysics (LAsp) at INAF-Osservatorio Astrofisico di Catania (Italy). The solid CO samples were prepared in a stainless steel high vacuum chamber (pressure $<10^{-7}$ mbar) in which a crystalline silicon substrate is placed in thermal contact with a cold finger whose temperature can vary between 17 K and 300 K.

The samples were analyzed using infrared and Raman spectroscopies. Infrared transmission spectra were taken at oblique incidence (45°) by a Fourier transform infrared (FTIR) spectrometer (Bruker Equinox 55 or Vertex 70). Transmission spectra are obtained through the KBr windows in the chamber and a hole made in the cold finger, which allows the infrared beam to be transmitted through the substrate and the sample. The alignment of the IR beam of the spectrometer through the hole of the cold finger and KBr windows of the chamber is obtained using a moveable optical bench, on which an IR spectrometer is placed that permits fine vertical and horizontal adjustments. A rotatable polarizer placed along the path of the IR beam allows us to take spectra both with the electric vector parallel (p -polarized) and perpendicular (s -polarized) to the plane of incidence. Infrared spectra are taken with a resolution of 1 cm^{-1} .

In situ Raman spectra were acquired using two different setups with visible and near-infrared laser excitation, respectively (Fig.2.1). In the first setup, a Triplemate spectrometer by SPEX equipped with a Peltier cooled CCD detector is used. A continuous Ar-ion laser beam ($\lambda=514.5 \text{ nm}$) enters a confocal illuminator by DILOR, perpendicularly to its optical axis, into which it is deflected by a microprism. The con-

focal optical system is arranged in such a way that any parallel beam incident along the optical axis in the opposite direction of the laser is focused onto the entrance slit of the spectrometer. By means of two flat mirrors, the laser beam is reflected toward the vacuum chamber and focused by an objective lens into a $40\ \mu\text{m}$ spot on the sample. The back-scattered Raman light is collimated by the same objective into a parallel beam that, according to the setup geometry, goes back along the same path of the laser beam and reaches the confocal illuminator where it is focused onto the entrance slit of the spectrometer. Since the incoming laser and the Raman collected light are collimated into parallel beams, this configuration allows us to acquire Raman spectra up to several meters away from the spectrometer with negligible performance loss. The spectral resolution is about $5\ \text{cm}^{-1}$.

The second setup, with near-infrared laser excitation, uses an optical fiber-based compact monochromator HE785 by HORIBA. The spectrometer has a fixed objective grating and is equipped with a Peltier cooled CCD detector. The probe head has a confocal optical configuration and is oriented directly toward the objective lens of the chamber. The optical path of the incoming laser beam that emerges from the head, and the collected Raman beam is analogous to that already described for the visible setup. A solid state continuous wave (CW) 785 nm laser diode is used as exciting source. The near-infrared excitation permits a significant decrease in the strong fluorescence continuum usually observed in carbon containing molecular samples irradiated at low doses, when using visible laser excitation (e.g., Ferini et al. 2004). Although the Raman features are relatively $(785\ \text{nm}/514.5\ \text{nm})^4=5.4$ times less intense with respect to the 514.5 nm excitation, this setup is particularly useful when searching for weak features of species formed by ion bombardment. A strong fluorescence continuum can indeed totally mask weak features. The spectral resolution is $10\ \text{cm}^{-1}$.

In the experiments we present here, a needle valve is used to admit gaseous CO (Aldrich, 99.0%) into the vacuum chamber where it freezes on the substrate. The gas inlet is not directed toward the substrate, thus a “background deposition” is obtained. This method ensures a uniform thickness of the film, but has the disadvantage that the gas phase molecules can freeze out onto all of the cold surfaces inside the chamber. To avoid any deposition on the backside of the substrate, this is protected by a 2 cm long copper tube aligned with the IR beam with a central hole of 4.5 mm.

The vacuum chamber is connected to a 200 kV ion implanter by Danfysik. The irradiation experiments were carried out using 200 keV H^+ . The ion beam is electrostatically swept to ensure a uniform coverage on the target and produces a 2×2 cm² spot on it. To avoid a macroscopic heating of the irradiated sample, we used an ion current density between 100 nA cm⁻² and a few μ A cm⁻². The ion fluence (ions cm⁻²) was measured by integrating the ion current monitored during irradiation.

The energy deposited by incoming ions to the sample (dose) was obtained by multiplying the fluence and stopping power (i.e., the amount of energy deposited per unit path length; eV cm²/molecule) given by SRIM code (Ziegler et al. 2008). In this work the dose is given in eV/16u, which is a convenient way to characterize chemical changes and to enable a comparison with other experiments with different samples (Strazzulla et al. 1991).

2.2.1 Thickness measurement

We followed the procedure described in Fulvio et al. (2009) and Modica & Palumbo (2010) to measure the thickness of the CO solid film. In the experiments we present here, a He-Ne laser beam ($\lambda = 543.5$ nm) is directed toward the sample and reflected at 45° both by the vacuum-ice and ice-substrate interfaces. The reflected laser beam is detected by an external silicon-diode detector. There is a difference in the optical path between the reflected components of the laser beam that varies with the thickness of the film, so that interference is produced. Hence it is possible to follow the accretion of the frozen film by looking at the interference curve (intensity versus time) of the reflected laser beam (see Fig. 2.2 A).

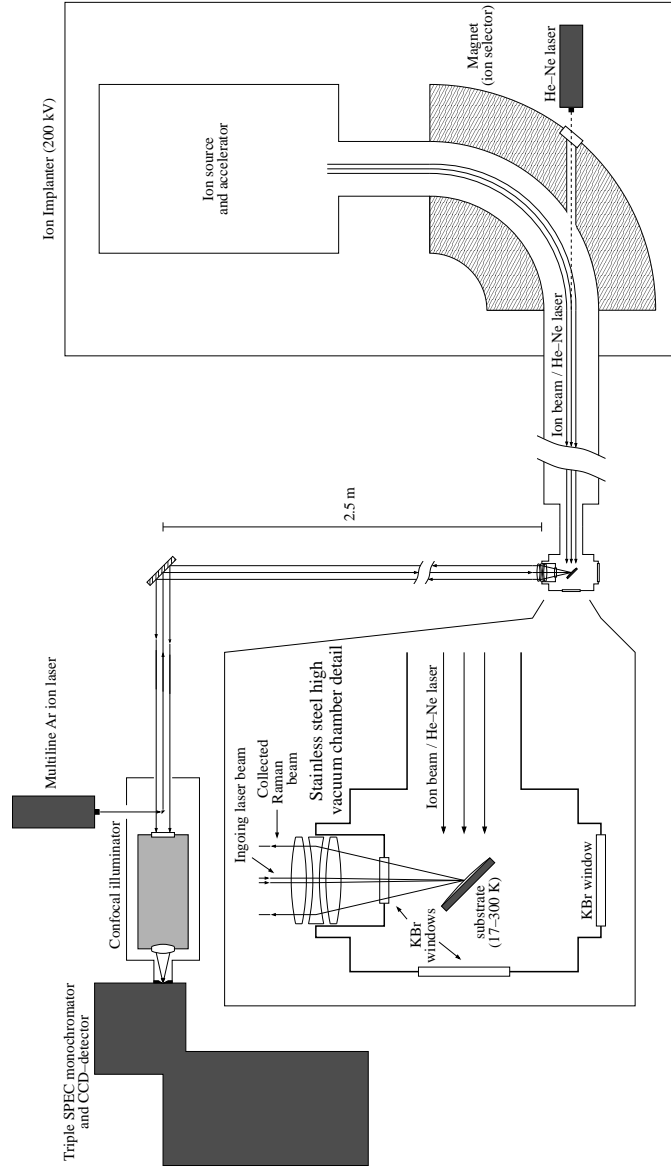


Figure 2.1: Schematic view of the Raman setup. The Ar laser beam is focused on the sample mounted inside the HV chamber, which is connected to the Ion implanter.

The spikes in the interference curve indicate the time when the infrared spectra are taken. The damping seen in the interference curve is due to scattering loss, either by the bulk or surface of the film, and a loss of coherence of the reflected light at the two, vacuum-film and film-substrate, interfaces. It should be considered that the damping is not usually due to absorption since most of the molecular ices are transparent at visible wavelengths. In general, the reflectance of a thin film deposited over a substrate can be schematically represented by Eq.2.1

$$R = F(n_f, n_s, d, \theta_i, \lambda), \quad (2.1)$$

where n_f and n_s are the complex refractive indexes of the film and substrate respectively, d is the film thickness, θ_i is the incidence angle and λ is the wavelength. If the incidence angle is not equal to 0, this function also depends on the polarization of the incident electromagnetic field. At fixed wavelength, the reflectance R versus the thickness is, for nonabsorbing materials, a periodic function whose period (distance between two maxima or minima) is given by Eq.2.2

$$\Delta d = \frac{\lambda_0}{2n_f \sqrt{1 - \sin^2 \theta_i / n_f^2}}, \quad (2.2)$$

where λ_0 is the laser wavelength. From Eq.2.2, it is evident that the refractive index of the sample must be known in order to measure the thickness. Nevertheless, the amplitude of the interference curve itself depends on the refractive index, so by measuring this quantity (intensity ratio between maxima and minima) it is possible to derive the refractive index of the sample and then the thickness. In particular in Eq.2.1, λ_0 , θ_i , and n_s are known quantities, hence for a given refractive index of the film (n_f), an interference curve (R versus the thickness d) can be computed. In order to derive the refractive index of the film, n_f

is automatically varied, using a FORTRAN code, until the theoretical amplitude of the interference curve becomes equal to the experimental amplitude. We found $n_f = 1.30$ for frozen CO. As an example, looking at Fig. 2.2 it is possible to compare the experimental interference curve obtained during the deposition of CO on a silicon cold substrate (A) with the computed theoretical curve (B).

A free web interface to the FORTRAN code used in this work is available at <http://www.oact.inaf.it/spess/>. This interface calculates the refractive index of the ice sample and gives the theoretical interference curve from the amplitude of the experimental interference curve. The sample thickness can be obtained by comparing the theoretical interference curve with the experimental one. Since the experimental reflectance is usually given in arbitrary units and exhibit a damping due to scattering losses, a direct comparison between the theoretical and experimental curves is not possible. In this work both the experimental and theoretical curves are normalized by placing all the minima at 0 and the maxima at 1 before the comparison. The normalization procedure is straightforward for the theoretical curve since the minima and maxima have the same intensity. In the case of the experimental curve two spline continuum, passing through the minima and maxima, respectively, can be used for normalization. For each chosen point, we read the intensity in the normalized experimental interference curve. Then we identified the point at which the normalized intensity corresponds at the given fringe number in the normalized theoretical curve; the abscissa of the point is the value of the thickness.

This method ensures a measure of the film thickness with an absolute accuracy of about 5%. The main limits are the uncertainties in knowledge of the refractive index of the substrate at low temperature and the error in measuring the incidence angle of the laser. In the present version of the web interface, only some of the more com-

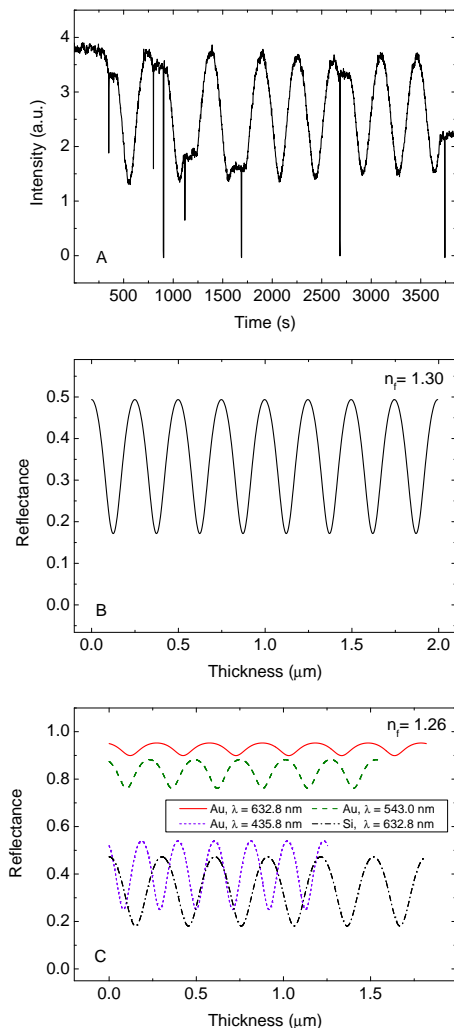


Figure 2.2: *Panel A): experimental interference curve obtained during the deposition of gaseous CO on a Si cold substrate using an He-Ne laser. Panel B): theoretical interference curve for solid CO film on a Si cold substrate. The comparison between the theoretical and experimental curves allows us to measure the sample thickness using the interference fringe method. Panel C): theoretical interference curves calculated assuming an ice with refractive index equal to 1.26 that is deposited on cold Au substrate for different laser wavelengths. For comparison, the interference curve computed for the same ice deposited on silicon is shown.*

mon opaque substrates (silicon, aluminum, gold) are considered. We would like to note that a smaller amplitude of the interference curve increases the uncertainty in the derived refractive index and thickness of the film owing to the experimental noise of the interference curve. In particular in the case of a gold substrate, the use of a laser at violet or UV wavelength is suggested. In fact, as shown in Fig. 2.2 C, the amplitude of the interference curve is small when laser wavelengths greater than about 500 nm are used. The theoretical optical model for the reflectance does not take into account the reflection at the second substrate interface (the one in contact with the cold finger). Indeed it is not straightforward to consider, in a reliable way, the contribution of the electromagnetic radiation that is transmitted through the substrate and reflected at the second substrate interface. Also, it is not straightforward to take into account the reflected component by mirror-like polished cold finger surface. Hence the procedure can only be used reliably in the case of substrates that are opaque at the laser wavelength.

2.3 Results

We carried out several experiments to study the profile of the 2140 cm^{-1} fundamental band of solid CO by infrared transmission spectroscopy and Raman spectroscopy as a function of temperature, irradiation dose and thickness of the CO sample. Throughout the chapter IR spectra are plotted in a decreasing wavenumber scale (i.e., increasing wavelength) as this is the common style in the astronomical literature, while Raman spectra are plotted in increasing wavenumber scale. We present our results in the following sections. In Fig. 2.3 we show the peak position of the CO band at different temperatures (*A*), irradiation doses (*B*), and film thicknesses (*C*). To obtain these values, we fitted each CO band with a polynomial curve and then we reported the position of the maximum of each fit. As said in § 2, the Raman spectral resolution is 5 cm^{-1} , so it is not possible to resolve the LO and TO mode of solid CO.

2.3.1 Temperature experiments

In this paragraph we show the data collected for a 0.1 μm -thick CO sample increasing its temperature from 17 K to 32 K, the highest temperature at which spectra can be acquired in our experimental condition before which CO starts to sublime. In Fig. 2.4 *A* we report the IR spectra in P polarization showing the LO-TO splitting, while in Fig. 2.4 *B* we show the spectra of the same sample in S polarization. No significant variation of the band profile occurred during the warm up. As is discussed in §3.3, the relative intensities of TO and LO bands depend on the thickness of the sample. It is possible to notice just a

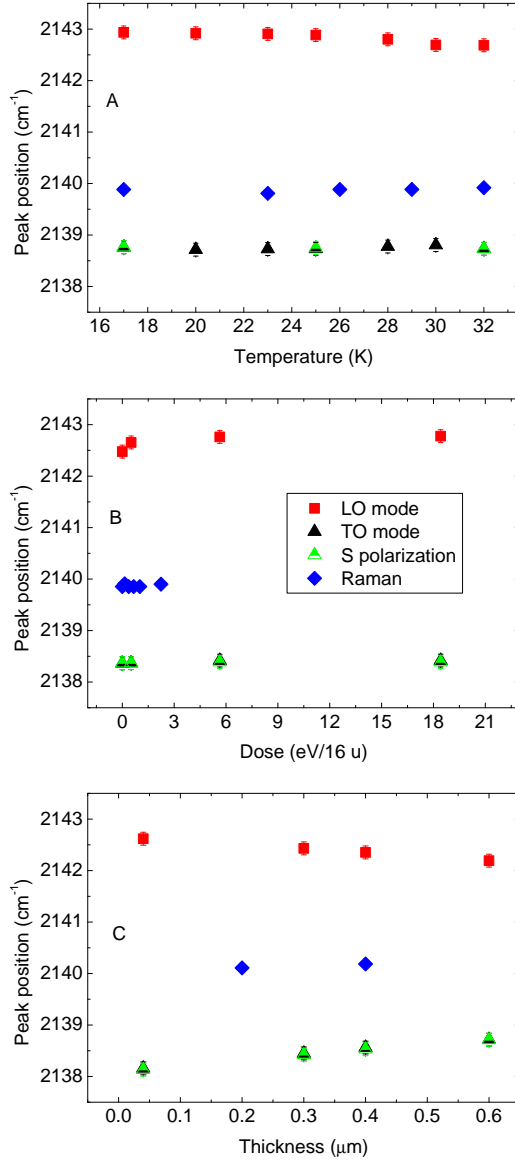


Figure 2.3: Experimental CO peak positions measured in IR and Raman spectra varying the sample temperature (panel A), irradiation dose (panel B), and film thickness (panel C). Red squares: LO band in P polarization; black triangles: TO band in P polarization; green triangles: CO band in S polarization; and blue rhombus: Raman stretching mode band.

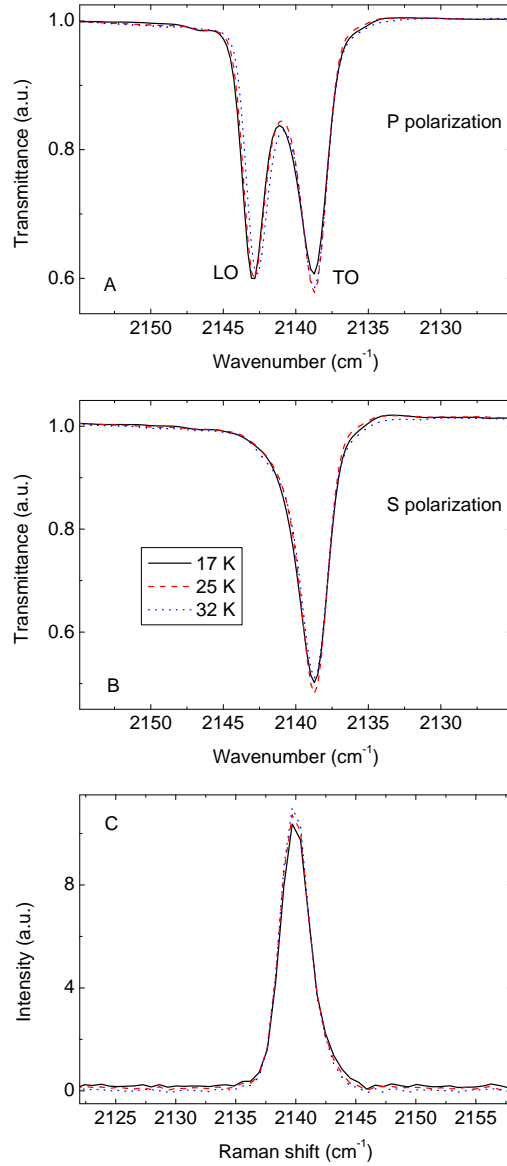


Figure 2.4: Experiments performed increasing the sample temperature. Panels A), B): infrared spectra of the fundamental vibrational band of solid CO and panel C): Raman spectra of the stretching mode feature. Black solid line: solid CO film at 17 K; red dashed line: 25 K; and blue dotted line: 32 K.

small variation in the intensity of the band. The same experiment has been repeated in the case of Raman analysis and the results are reported in Fig. 2.4 *C*. It is well known that this technique is particularly sensitive to structural variations, but except for a small increase of the peak intensity, as seen for IR spectra, the band profile does not show any significant change.

In Fig. 2.3 *A* it is clearly visible that from 17 K to 32 K is not possible to observe any variation of the band peak position either in the IR or in the Raman spectra. The measured values, in fact, differ by less than the uncertainties (0.25 cm^{-1} in the IR spectra and 1 cm^{-1} in the Raman spectra). The peak position of the band in the IR spectra, remains nearly constant at about 2138.7 cm^{-1} for the TO band and 2142.8 cm^{-1} for the LO band. The Raman peak position also remains almost constant at 2140.0 cm^{-1} .

2.3.2 Irradiation experiments

In Fig. 2.5 we show the Raman spectra and IR spectra acquired in P polarization and S polarization of a $0.2 \mu\text{m}$ -thick solid CO film before and after irradiation with 200 keV H^+ . In Figs. 2.5 *A* and *B* it is possible to see that the band intensity decreases at increasing irradiation doses. The energetic ions (keV-MeV) used to irradiate the sample release their energy to the target along the ion track. As a consequence molecular bonds are broken, and radicals and molecular fragments recombine to form new molecular species not present in the original sample. The irradiation of solid CO causes the synthesis of carbon dioxide and others carbon and oxygen containing molecules, such as carbon chain oxides. This phenomenon is well known and extensive studies have been reported by Trottier & Brooks (2004), Loeffler et al. (2005), Palumbo et al. (2008), and Seperuelo Duarte et al. (2010). In Fig. 2.5 *C* we report a portion of the Raman spectra showing the solid

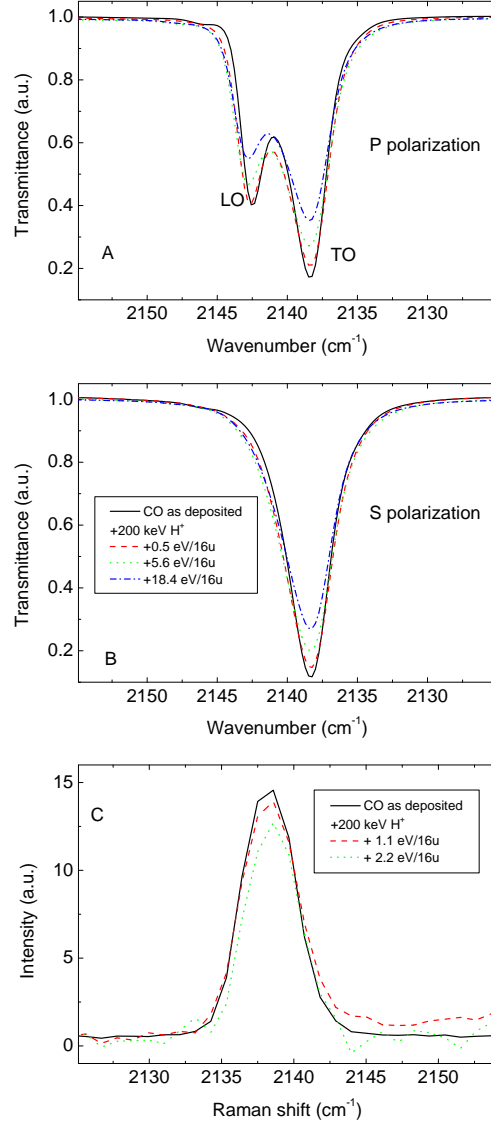


Figure 2.5: Energetic processing of solid CO film with 200 keV H^+ . Panel A): IR spectra in P polarization. Panel B): IR spectra in S polarization. CO film as deposited (black solid line); CO film after irradiation dose of 0.5 eV/16u (red dashed line), 5.6 eV/16u (green dotted line), and 18.4 eV/16u (blue dash-dotted line). Panel C): Raman spectra. CO film as deposited (black solid line); CO film after irradiation dose of 1.1 eV/16u (red dashed line), 2.2 eV/16u (green dotted line).

CO band. As described in Ferini et al. (2004), after ion bombardment, an intense fluorescence continuum appears in all the Raman spectra because of radiative recombination of electron-hole pairs produced by the Raman laser irradiation. For clarity we subtracted this continuum. Because of different selection rules, by using Raman spectroscopy it is possible to observe molecular transitions that are not active in the infrared. In Fig. 2.6 a different portion of the same spectra shown in Fig. 2.5 *C* is reported. The contribution due to the fluorescence continuum has also been subtracted in these spectra. We observed a band centered at 1817 cm^{-1} that is clearly visible at higher irradiation doses and a band centered at 1767 cm^{-1} since the first irradiation step. The Crovisier database ¹ reports a vibrational band of gaseous C_2 at 1828 cm^{-1} , so we tentatively attribute the 1817 cm^{-1} band to solid C_2 . A contribution from C_5O , which had been assigned to a feature observed close to this position by Sicilia et al. (2012), could also be present. We were not able to attribute the 1767 cm^{-1} band to any molecule. Since the feature is not present within the noise level in the IR spectra, this suggests that it could be due to a symmetric vibrational mode in a molecular species without a permanent dipole moment.

In Fig. 2.3 *B* we report the peak position of the CO band versus the irradiation dose. No significant variation of the CO band peak position is observed during irradiation in the range of doses that we investigated. In fact, the band peak positions remain almost constant at about 2138.4 cm^{-1} and 2142.6 cm^{-1} for the TO and LO mode, respectively. The Raman spectra show that the band is centered at about 2139.9 cm^{-1} and that it remains unaltered, within the noise, throughout the experiment.

In order to decrease the strength of the fluorescence background that adds noise to the Raman spectra, we carried out an experiment using

¹<http://www.lesia.obspm.fr/perso/jacques-crovisier/basemole/>

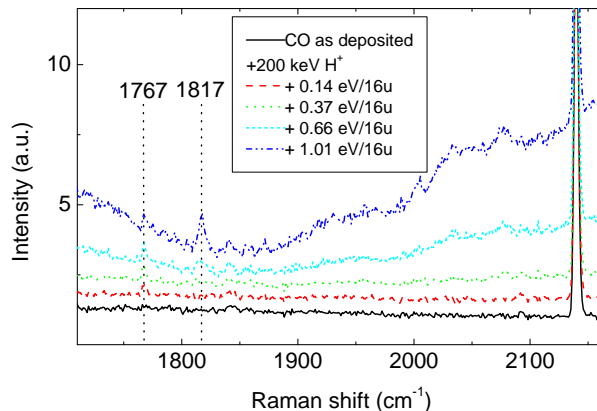


Figure 2.6: Raman spectra of solid CO irradiated with 200 keV H^+ . CO film as deposited (black solid line); CO film after irradiation dose of 0.14 eV/16u (red dashed line), 0.37 eV/16u (green dotted line), 0.66 eV/16u (cyan short-dashed line), and 1.01 eV/16u (blue dash-dotted line). Black dotted vertical lines indicate 1767 cm^{-1} unidentified band and 1817 cm^{-1} band tentatively attribute to C_2 .

a near-infrared laser excitation wavelength at 785 nm. Nevertheless, in this case there is also no significant variation of the CO profile increasing the irradiation dose, so we do not report the spectra.

2.3.3 Increasing Thickness

We carried out some experiments in which the thickness of the solid CO layer has been varied. As shown in Fig. 2.7 A and B, we acquired the IR spectra both in P and S polarization after the deposition of 40 nm (black solid line), 300 nm (red dashed line), and 600 nm (blue dotted line) thick solid CO. Both P and S polarization spectra show an increase in transmittance at about 2133 cm^{-1} . This happens because of the sharp variation in the real part of the refractive index (n) of solid CO at this wavenumber, and also this increase depends on the optical

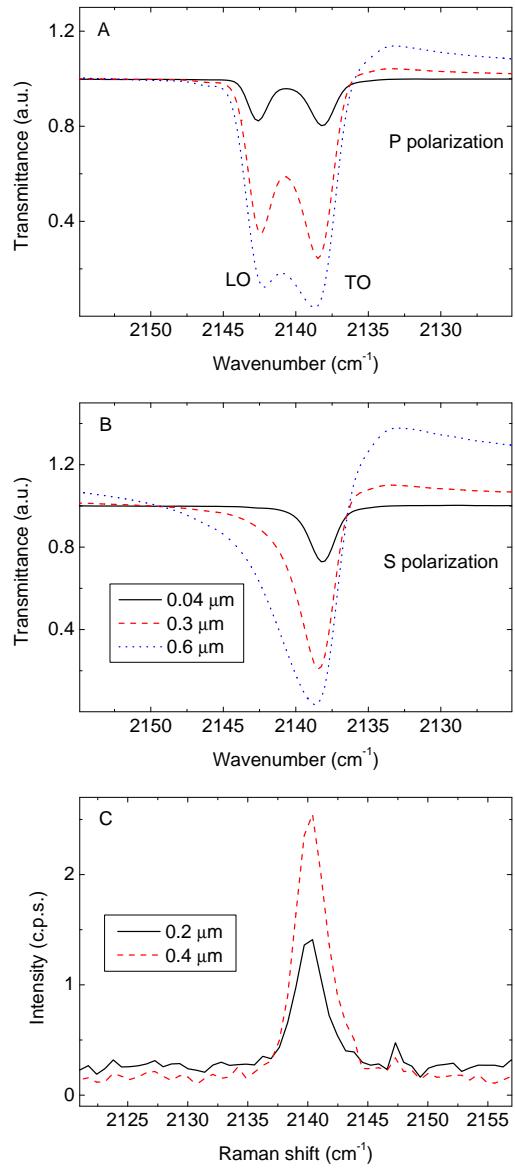


Figure 2.7: Thickness experiment. Panel A): IR spectra in P polarization; panel B): IR spectra in S polarization. CO film thickness: black solid line: 0.04 μm; red dashed line: 0.3 μm; blue dotted line: 0.6 μm. Panel C): Raman experiment. CO stretching mode band of a 0.2 μm (black solid line) and 0.4 μm (red dashed line) film.

properties of the substrate. This feature is predicted by theory and is well reproduced by theoretical optical models employing experimental optical constants of solid CO (see Fig.4 in Baratta & Palumbo (1998)). In Fig. 2.3 *C* we observe the band peak position of the TO mode slightly increasing from the 40 nm to the 600 nm thick layer; in particular it varies between 2138.1 and 2138.7 cm^{-1} . The peak position of the LO mode remains almost constant between 2142.6 and 2142.2 cm^{-1} throughout the experiment.

In Figs. 2.7 *A* and *B* the CO band of the 0.6 μm thick sample is close to reaching saturation. In principle, this could hinder the linear correlation existing between the thickness of the film (related to the amount of CO in the sample) and the area underlying the band. In Fig. 2.8 black squares represent the values of the CO band area measured at 0.04, 0.3, 0.4, 0.6, 1.3, and 1.9 μm thickness. The graph shows that even if the band is close to saturation at 0.6 μm thickness (see the blue dotted line in Figs. 2.7 *A* and *B*), its area still linearly increases with the film thickness, as shown by the linear best fit (red line) in Fig. 2.8.

Raman spectra are shown in Fig. 2.7 *C*. They were acquired at 200 nm (black solid line) and 400 nm (red dashed line) thickness. The band shape and peak position do not show any relevant variation.

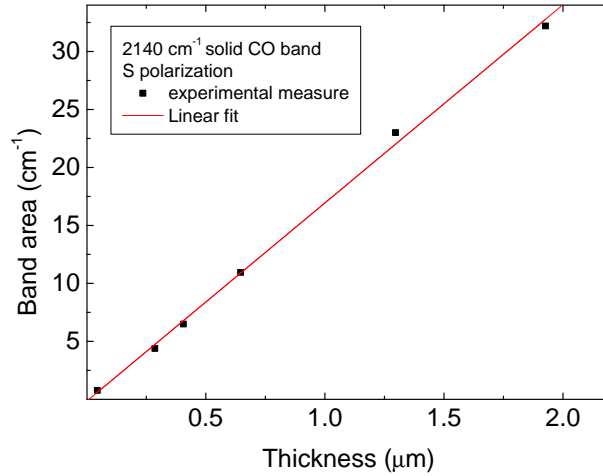


Figure 2.8: *Solid CO band area vs. film thickness. Black squares: measured values of the band area; red solid line: linear fit of the measured areas.*

2.4 Discussion

Comparing our Raman spectra of solid CO with those presented by Katz et al. (1984), we notice that the profile of the CO band is similar to the profile of β -CO, which is a much disordered phase if compared to the ordered α -CO. We explain the formation of a disordered structure in our HV chamber because of the fast cooling of the CO gas when it comes in contact with the cold surface of the substrate on the sample holder.

In the experiments that we carried out at increasing temperatures from 17 K to 32 K (see Fig. 2.4), we would have expected a relevant variation in the IR and an even more pronounced in the Raman of the CO band profile if a structural change had occurred. But these varia-

tions are almost absent. This result is in agreement with Lasne et al. (2015) who studied the LO-TO splitting to calculate the spontelectric field in solid CO. They found that annealing from 18 to 26 K does not produce detectable shifts of the LO and TO bands. A study of the profile of the LO- and TO-components at about 2140 cm^{-1} of solid CO during warm-up in the temperature range 14-26 K has recently been reported by Muñoz Caro et al. (2016). Also, in their experiments, the band profile remained unaltered. Our results are also in agreement with those presented by Löwen et al. (1990). They report that no change of structure and no frequency shifts have been observed in the Raman spectra of solid CO in the temperature range between 4.5 and 30 K. So we conclude that our samples preserve the same structure during warm up. Alternatively, the profile of the CO band does not depend on the structure of the sample.

We have also investigated any possible modification of the CO band profile after ion irradiation (see Fig. 2.5). As already noticed in the previous section, ion irradiation causes the reduction of the intensity of the CO band in the IR spectra. This is due to the formation of new molecular species in the samples. In Fig. 2.3 *B* we see that while the peak position of the TO band remains almost constant, the peak position of the LO band slightly shifts to higher wavenumbers between the first and second irradiation step. This small variation is comparable with the shift of the LO peak position observed as a function of film thickness. The Raman spectra do not show any significant variation in the band profile after ion irradiation.

Most of our knowledge about the composition and structure of interstellar and planetary ices is based on the comparison between laboratory and astronomical spectra. When high resolution astronomical spectra are available, it is possible not only to identify a given solid phase species but also, from the band profile, to infer the mixture it

is embedded in and the average temperature experienced by the ice in a given environment. As an example, crystalline water ice has been identified toward high-mass young stellar objects based on the profile of the $3\ \mu\text{m}$ water ice band (e.g., Dartois & d’Hendecourt 2001).

Some attempts have been made to infer the structure of solid CO observed toward low-mass young stellar objects. Pontoppidan et al. (2003) reported about the stretching band of solid CO detected toward several young stellar objects by means of the VLT-ISAAC. They found that this band results from the superposition of three components centered at $2143.7\ \text{cm}^{-1}$, $2139.9\ \text{cm}^{-1}$ and $2136.5\ \text{cm}^{-1}$, respectively. They suggested that in the majority of the observed lines of sight, most of the CO is in a nearly pure form. Moreover, they attributed the $2143.7\ \text{cm}^{-1}$ component to the LO mode of the vibrational transition of solid crystalline CO.

Chapter 3

On the detection of solid
deuterated water in
astrophysical environments:
constraints from laboratory
experiments

3.1 Deuterated water in astrophysically relevant ices

Based on Urso, R. G., Palumbo, M. E. et al. in prep.

Infrared observations toward several star-forming regions allow to obtain primary information on the chemical and physical nature of dust grains and their icy mantles (e.g., Boogert et al. 2015). The analysis of the spectra acquired revealed the presence of water and carbon monoxide as the main constituents of icy grain mantles, followed by carbon dioxide, methane, methanol and ammonia (Boogert et al. 1997; Gibb et al. 2004; Dartois 2005; Öberg et al. 2011; Boogert et al. 2015). Also, other molecules have been likely detected, such as formaldehyde (H_2CO), sulphur dioxide (SO_2) and carbonyl sulphide (OCS, Schutte et al. 1994; Boogert et al. 1997; Palumbo et al. 1997). Solid phase molecules are also present on a variety of places in the Solar System, such as on the surfaces of satellites of outer planets, the trans-Neptunian objects (such as Pluto), and the comets (e.g., Cruikshank et al. 1984; Morrison et al. 1984; Thomas et al. 1986; Brown et al. 1995; Calvin et al. 1995; Cruikshank et al. 1995; Nash & Betts 1995)

To better understand the chemical composition and physical structure of ices in space, it is fundamental to compare infrared spectra acquired by telescopes with those obtained in laboratory experiments in which ice analogues are produced. As an example, several experimental works have been focused on studying thermal induced changes in water ice by means of laboratory infrared spectroscopy. The study of the band profiles (i.e., shape, width and peak position) with increasing temperature allowed to obtain information about the physical structure of water ice and its phase changes (e.g., Hudgins et al. 1993; Grundy &

Schmitt 1998; Dartois & d’Hendecourt 2001; Bossa et al. 2012).

In particular, the 3 μm band profile of solid water, related to both symmetric and asymmetric O-H stretching vibrational modes, shows a strong variation with increasing temperature. In fact, at low temperature (few tens K) it appears smooth and symmetric. During the warm up, the band profile gradually changes between 100 and 155 K, becoming sharper and structured. Detailed studies on this feature attributed the change to both compaction of the porous as deposited sample and its transition between a disordered phase to a much ordered one, i.e. amorphous to crystalline transition (e.g., Rowland et al. 1991; Jenniskens & Blake 1994). The change in porosity is also testified by the disappearance of the O-H dangling bond feature, that is characterized by the presence of two bands centred at 3697 and 3720 cm^{-1} , attributed to three- and two-coordinated water molecules respectively, that appear in porous amorphous water ice only (e.g., Rowland et al. 1991; Palumbo 2006).

The search for structural variations has been carried out for other astrophysical relevant species. Hudgins et al. (1993) reported about the infrared spectra of several species and mixtures with increasing temperature. As an example, they observed that the methanol amorphous-to-crystalline transition takes place between 100 and 120 K, as evidenced by the sharpening of its infrared bands. Recently, Urso et al. (2017) have shown experimental results on the thermal evolution of solid state formamide between 17 and 300 K. Also in this case, the warm up induce the crystallization of the formamide sample, that is evidenced by the sharpening of all the formamide vibrational features.

Together with thermal processing, energetic processing, i.e. bombardment by cosmic rays and UV photons, has a strong effect in modifying the chemical and physical structure of ices. In particular, laboratory experiments have shown that one of the most evident effects induced

by energetic processing is the ice compaction and amorphization. As an example, it has been shown that ion bombardment causes both the compaction of amorphous water ice (e.g., Palumbo 2006; Raut et al. 2007b; Dartois et al. 2013) and the amorphization of crystalline water ice (e.g., Baratta et al. 1991; Moore & Hudson 1992; Leto & Baratta 2003; Leto et al. 2005; Dartois et al. 2015). Taking into account the differences observed in the band profiles of amorphous and crystalline samples acquired in laboratory experiments, it has been possible to spread light on the icy grain mantles structure in star-forming regions (e.g., Dartois & d’Hendecourt 2001) and on outer Solar System objects (e.g., Grundy et al. 1999).

Several water and carbon monoxide isotopologues have been detected in the gas phase of star-forming regions, such as HDO, H_2^{18}O , D_2O , $^{13}\text{C}^{18}\text{O}$, ^{13}CO , C^{17}O , C^{18}O (e.g., Turner et al. 1975; Jacq et al. 1988; Butner et al. 2007; Langer & Penzias 1990; Pineda et al. 2008; Kama et al. 2013; Coutens et al. 2014; Nagy et al. 2017). In the solid-phase, ^{13}CO has been detected, together with $^{13}\text{CO}_2$ (e.g., Boogert et al. 2000, 2002; Gibb et al. 2004). Isotopologues have been observed in the Solar System also (e.g., Hartogh et al. 2011; Füri & Marthy 2015). These observations refer to gas-phase species. To the best of our knowledge, the detection of solid-phase isotopologues has not yet been reported. Furthermore, several attempts have been made to investigate the presence of deuterated water, HDO and D_2O , looking for the O-D stretching mode band at $4.1 \mu\text{m}$ (Parise et al. 2003). As an example, Teixeira et al. (1999) have shown the presence of this band in the line-of-sight to W33 A and NGC7538 IRS9 thanks to the comparison between ISO-SWS spectra and laboratory infrared spectra of solid mixtures containing various ratios of water and deuterated water. However, these detections have been questioned by Dartois et al. (2003). In fact, according to the comparison between laboratory

experiments and spectroscopic observations carried out with two telescopes (VLT and UKIRT), they report that the HDO 4.1 μm feature detected toward W33 A by Teixeira et al. (1999) is due to the presence of amorphous methanol, and that the feature they claimed is a calibration problem or an instrumental response. Also the HDO absorption in NGC 7538 IRS9 could be attributed to detector instabilities. Aikawa et al. (2012) reported about the tentative detection of the O-D stretching mode in HDO toward L1527, IRC-L1041, IRAS04302 and HV Tau obtained with the InfraRed Camera on board of the AKARI telescope. Also, using the band strength value determined by Dartois et al. (2003) (4.3×10^{-17} cm molecule $^{-1}$), they calculated the HDO abundance between 2 and 22% w.r.t. H₂O.

Useful data on the presence and abundance of solid-phase deuterated water in space could be obtained by James Webb Space Telescope (JWST) observations. In fact, the sensitivity of the on-board detectors could allow the detection of the 4.1 μm band. With this in mind, in this chapter we describe recent experiments we performed to study the O-D stretching mode band in solid mixtures containing water and deuterated water in various ratios deposited at 17 K. During the experiments, the samples have been either heated or irradiated with energetic ions (200 keV H⁺) in order to study the effects induced by both thermal and energetic processing. The implications to the detectability of this band are also discussed.

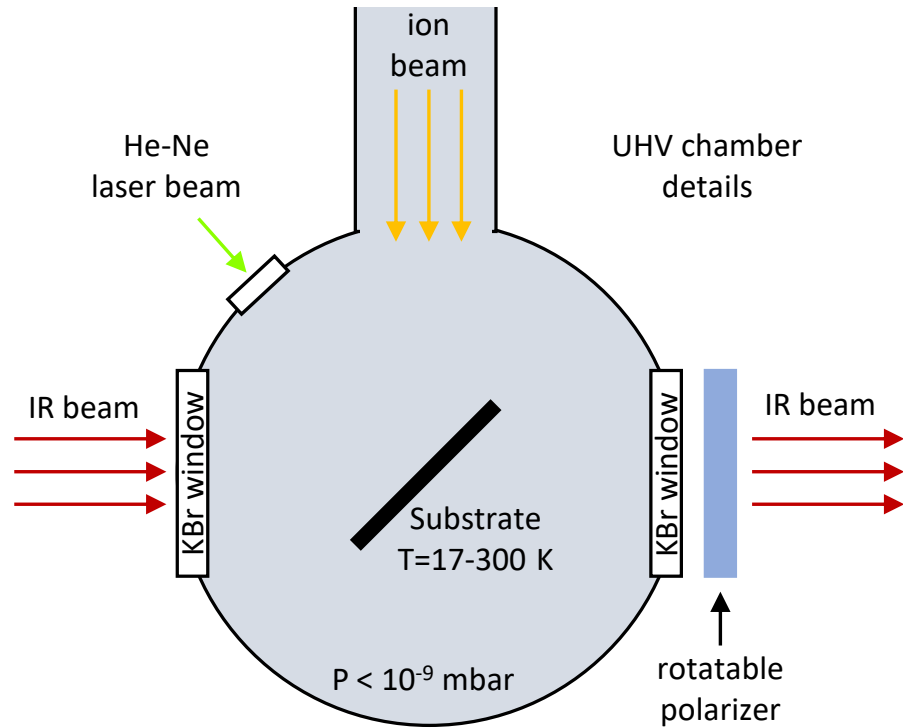


Figure 3.1: Schematic top view of the UHV chamber and the geometry used to perform irradiation and infrared spectroscopy on frozen samples.

3.2 Experimental methods

The experiments were performed in the Laboratory for Experimental Astrophysics at INAF-Osservatorio Astrofisico di Catania (Italy). Two different sets of experiments were performed, in order to investigate the thermal evolution and the effects of the bombardment with energetic ions (200 keV H⁺) on frozen mixtures containing H₂O, HDO and D₂O. All the experiments were performed in an ultra high vacuum

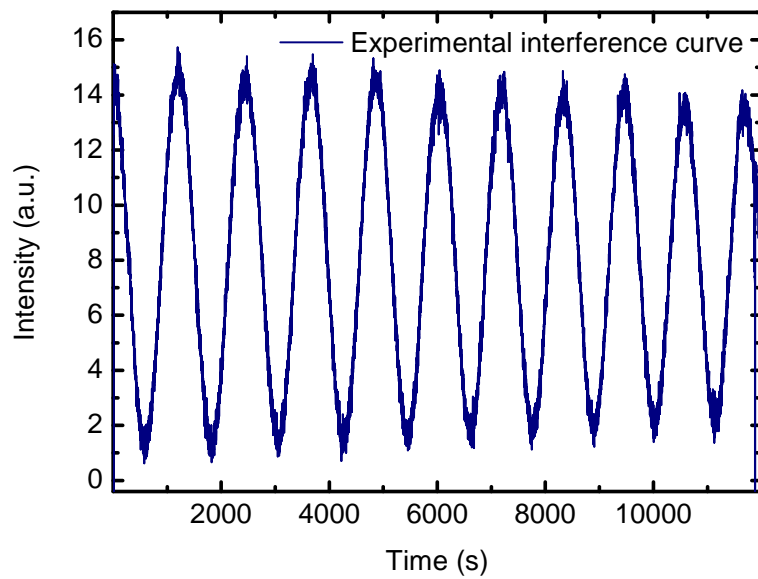


Figure 3.2: *Experimental interference curve obtained using a He-Ne laser during the deposition of a $D_2O:HDO$ mixture on a KBr substrate.*

(UHV) chamber ($P \leq 10^{-9}$ mbar, see Fig. 3.1) in which a KBr substrate is placed in thermal contact with the final tail of a closed-cycle helium Cryocooler (CTI) which temperature can be varied between 17 and 300 K. Gaseous mixtures were prepared in a mixing chamber in which pure water (Sigma Aldrich Chromasolv Plus) and D_2O (Aldrich, 99.990% D) are injected. In this chamber, mixtures with various H_2O/D_2O ratios were prepared, and for each mixture we waited enough to allow the isotopic exchange between H_2O and D_2O to occur. A needle valve allows the resulting mixtures to enter the UHV chamber, where they condense on the cold substrate forming a solid film.

The frozen mixture ratios have been calculated a posteriori from the infrared spectra obtained after each deposition, measuring the O-H and O-D stretching band mode areas. To estimate the column density N of water and deuterated water in the samples we used the equation:

$$N = \frac{\int \tau(\nu) d\nu}{A} \quad (3.1)$$

where τ_ν is the optical depth and A is the band strength (cm molecule^{-1}). For the O-H stretching mode band $A=2.0 \times 10^{-16} \text{cm molecule}^{-1}$ (Gerakines et al. 1995), while for the O-D stretching mode band $A=4.3 \times 10^{-17} \text{cm molecule}^{-1}$ (Dartois et al. 2003). The presence of HDO in the frozen samples is confirmed by the profile of the $4.1 \mu\text{m}$ feature (Gálvez et al. 2006).

During the deposition, the sample thickness has been measured following the procedure described in Fulvio et al. (2009) and Urso et al. (2016). A He-Ne laser beam ($\lambda = 543.5 \text{ nm}$) is directed toward the sample and reflected at near normal incidence (2.9°) both by the vacuum-sample and sample-substrate interfaces. The reflected beam is focused on an external silicon diode detector. There is a difference in the optical path between the reflected components of the laser beam that varies

with the thickness of the film, so that an interference curve is produced. It is possible to follow the accretion of the film by looking at the interference curve (intensity vs. time) of the reflected laser beam, such as the one shown in Fig. 3.2 that represent the deposition of 10 fringes of a D₂O:HDO solid mixture.

To study the samples thermal evolution, mixtures were deposited at 17 K and warmed up to their complete desorption. Several steps of warm up were performed for each sample. In the case of the energetic processing experiments, the mixtures were irradiated with 200 keV H⁺ at 17 K. The UHV chamber is connected to a 200 kV ion implanter by Danfysik. The ion beam is electrostatically swept to ensure a uniform coverage on the target. An ion current density between 100 nA cm⁻² and a few μ A cm⁻² was used in order to prevent a macroscopic heating of the sample. The ion fluence (ions cm⁻²) was measured by integrating the ion current monitored during irradiation. The energy deposited by incoming ions to the sample (dose) was calculated by multiplying the fluence and stopping power (i.e., the amount of energy deposited per unit path length; eV cm²/molecule) given by SRIM code (Ziegler et al. 2008). The dose is given in eV/16u, a convenient way to characterize chemical changes and to allow a comparison with other irradiation experiments (Strazzulla & Johnson 1991).

The samples were analyzed using infrared spectroscopy. Infrared transmission spectra were acquired at oblique incidence (45°) by a Fourier transform infrared (FTIR) spectrometer (Bruker Vertex 70) with a resolution of 1 cm⁻¹ and sampling of 0.25 cm⁻¹. A rotatable polarizer placed along the path of the IR beam allows us to take spectra both with the electric vector parallel (P-polarized) and perpendicular (S-polarized) to the plane of incidence of the infrared beam. Due to the fact that the transmitted signal in P-polarization is higher than the transmitted signal in S-polarization (Bohren & Huffman 1983), unless

differently specified, here we show the spectra acquired in P-polarization because of a better signal-to-noise ratio. We acquired transmission infrared spectra of the samples as deposited and after each step of irradiation and warm up. Also, during the experiments we set the spectrometer in a monitoring configuration that allows to check the infrared spectrum of the sample by means of fast and continuous acquisitions. In this way it was possible to stop the warm up and the irradiation and acquire a spectrum if some change would appear.

3.3 Results

In this section we present experimental results on the thermal processing of samples investigated in this chapter. Spectra (Fig. 3.3-3.5) have been collected at 17, 40, 80, 110, 120, 130, 140 and 155 K, the latter being the crystallization temperature of water in our experimental conditions. For clarity, we show only the spectra acquired at 17, 140 and 155 K between 4200 and 500 cm^{-1} (2.4-20 μm) in transmittance scale. In the figures, top axes report the wavelength in μm and bottom axes the wavenumber in cm^{-1} . Also, we show the results of the energetic processing with 200 keV H^+ of $\text{H}_2\text{O}:\text{HDO}=1000:1$ (Fig. 3.7) and $\text{H}_2\text{O}:\text{HDO}=2:1$ mixture (Fig. 3.9).

3.3.1 Thermal processing of $\text{H}_2\text{O}:\text{HDO}=1000:1$ mixture

In Fig. 3.3 we show the spectra acquired on a $\text{H}_2\text{O}:\text{HDO}=1000:1$ frozen mixture. Panel A shows the spectra acquired at 17 K (black line), 140 K (red line) and 155 K (blue line). In panel B the 3 μm band is shown. The narrowing and increasing in intensity of the band caused by warm up to 140 K, together with the absence of the O-H dangling bonds feature, suggest that the sample experienced the compaction. Finally, at 155 K the O-H stretching modes band exhibits three components, and the whole spectrum depicts a compact and crystalline water ice (Hudgins et al. 1993; Bossa et al. 2012). In Panel C the spectral range of the O-D stretching mode of HDO, centred at 2425 cm^{-1} (about 4.1 μm), is shown. Within the noise of the spectrum, none feature is detectable in this frequency range at 17 K. A feature assigned to the O-D stretching mode band appears at about 80 K, and in the spectrum

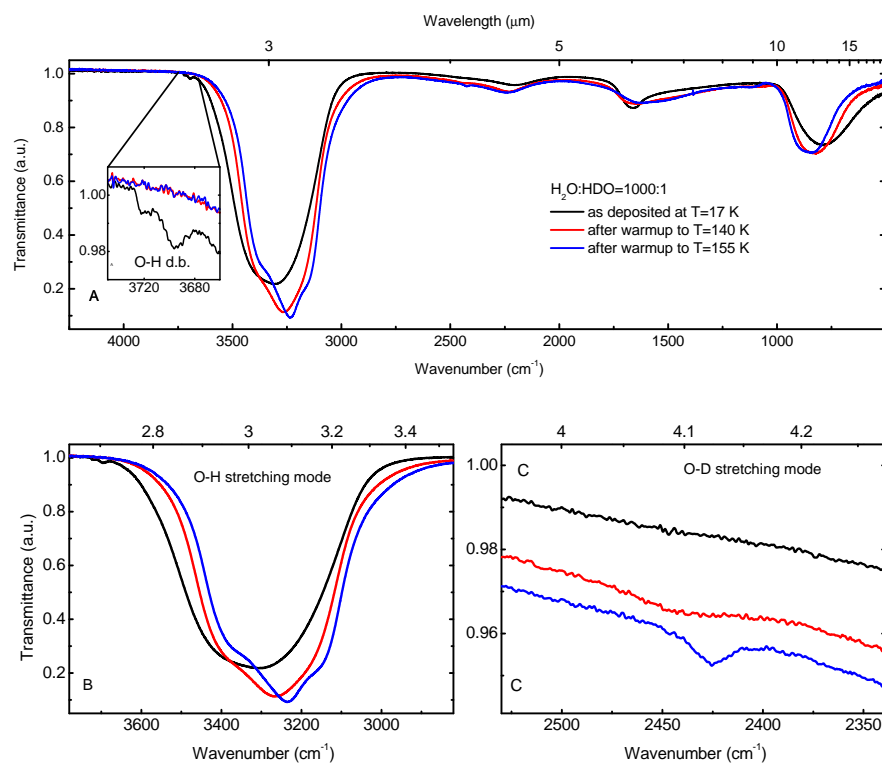


Figure 3.3: Infrared spectra of $\text{H}_2\text{O}:\text{HDO}=1000:1$ frozen mixture acquired at 17 K (black line), 140 K (red line) and 155 K (blue line) in transmittance scale. Panel A: full spectra; panel B: O-H stretching modes region; panel C: O-D stretching modes region.

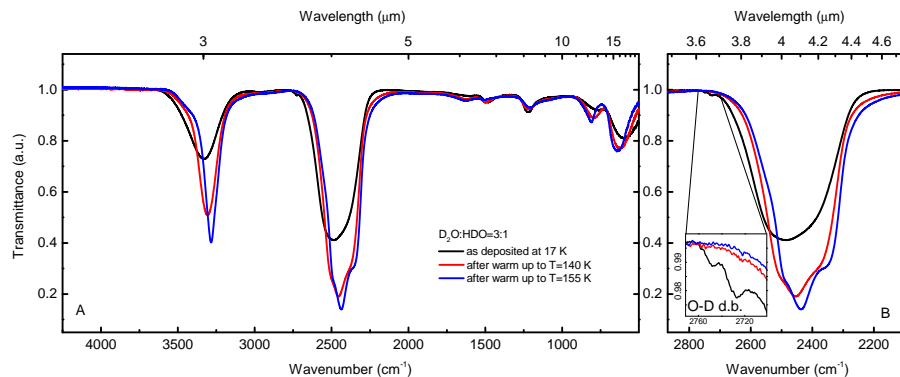


Figure 3.4: Infrared spectra in transmittance scale of a $D_2O:HDO=3:1$ mixture acquired at 17 K (black line), 140 K (red line) and 155 K (blue line). Panel A: full spectra; panel B: O-D stretching mode band; inset in panel B: zoom on the O-D dangling bond feature.

acquired at 140 K it is centred at about 2440 cm^{-1} , while at 155 K it is narrower and shifted to about 2425 cm^{-1} . At the latter temperature, the O-D stretching mode band FWHM is 20.3 cm^{-1} (about $0.04\text{ }\mu\text{m}$).

3.3.2 Thermal processing of $D_2O:HDO=3:1$ and $H_2O:HDO=2:1$ mixtures

To better investigate the O-D stretching mode band profile, other experiments have been performed by depositing solid mixtures containing a higher amount of deuterated water. In Fig. 3.4 the spectra of the $D_2O:HDO=3:1$ mixture deposited at 17 K and warmed up to 140 K and 155 K are shown.

At the deposition temperature (black line), the O-H stretching mode band is centred at 3330 cm^{-1} and the O-D stretching mode band at 2484 cm^{-1} . The warm up determines the shift toward shorter wavenumbers for both features. In particular, the O-H stretching mode band shifts to 3307 cm^{-1} (at 140 K) and 3284 cm^{-1} (at 155 K), while the O-D stretching mode band shifts to 2456 cm^{-1} (at 140 K) and 2437

cm⁻¹ (at 155 K). Also, the heating determines the narrowing and the increase in intensity of both features. These changes can be compared to those observed during the warm up experiment of pure water ice. In particular, it is interesting to notice that the O-D stretching mode band (Fig. 3.4 panel B) follows the same behaviour observed for the 3300 cm⁻¹ O-H stretching band in water (see Fig. 3.3, panel B). Also in this case we attribute these band changes to the sample compaction and to its amorphous-to-crystalline transition. It has to be noticed the absence of the O-H dangling bond feature in the spectrum acquired at 17 K, while we observed the O-D dangling bond bands, (see the inset in Fig. 3.4, panel B), centred at 2727 cm⁻¹ and 2748 cm⁻¹. As already observed for the O-H dangling bond feature, these bands are not present in the spectra acquired at 140 and 155 K, confirming that the sample has been deposited as a porous film and that the heating caused its compaction.

We also performed another experiment by depositing a H₂O:HDO=2:1 mixture. The spectra acquired at 17, 140 and 155 K are shown in Fig. 3.5. At 17 K, the O-H and the O-D stretching mode band are centred at 3316 cm⁻¹ and 2462 cm⁻¹, respectively. The O-D stretching mode band shows a FWHM of 149.7 cm⁻¹ (about 0.25 μm). At 140 K both band peaks shift to about 3275 and 2445 cm⁻¹, respectively. The O-D stretching mode band shows a FWHM of 95.1 cm⁻¹ (about 0.16 μm). Finally, at 155 K, the O-H stretching mode band is centred at 3243 cm⁻¹ and the O-D stretching mode band is centred at 2426 cm⁻¹, with a FWHM of 74.13 cm⁻¹ (about 0.126 μm). As noticed in the previous experiments, for both bands a narrowing and increase in intensity is also observed. It has to be noticed that the O-D dangling bond feature does not appear at the deposition temperature (see Fig. 3.5 panel B), where only the O-H dangling bonds bands are visible, centred at 3692 and 3718 cm⁻¹. This is due to the lower amount of

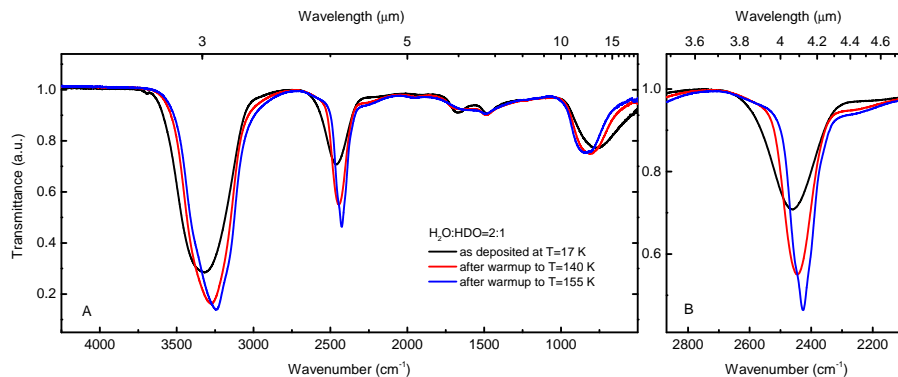


Figure 3.5: *Infrared spectra in transmittance scale of a $H_2O:HDO=2:1$ mixture acquired at 17 K (black line), 140 K (red line) and 155 K (blue line). Panel A: full spectra; panel B: O-D stretching mode band.*

as deposited deuterated water within the mixture with respect to the previous experiment.

In Fig. 3.6 we show the normalized O-D and O-H stretching mode band areas as a function of temperature we measured in the experiments here reported. Panel A shows that in the $H_2O:HDO=1000:1$ mixture, the O-D stretching mode can be observed approaching the amorphous-to-crystalline transition. Only upper limits can be established at temperature lower than 80 K. As it can be observed in panel B and C, when the deuterated water/water ratio increases, the O-D stretching mode band can be detected at lower temperatures also, independently of the sample structural phase. Our results show that the ratio between the O-H and O-D features strongly depends on the temperature in the case of the HDO diluted mixture (panel A in Fig. 3.6), while it is independent of temperature when a high deuterium amount is considered (see panels B and C in Fig. 3.6).

3.3.3 Energetic processing

In this section we report the results obtained during the irradiation

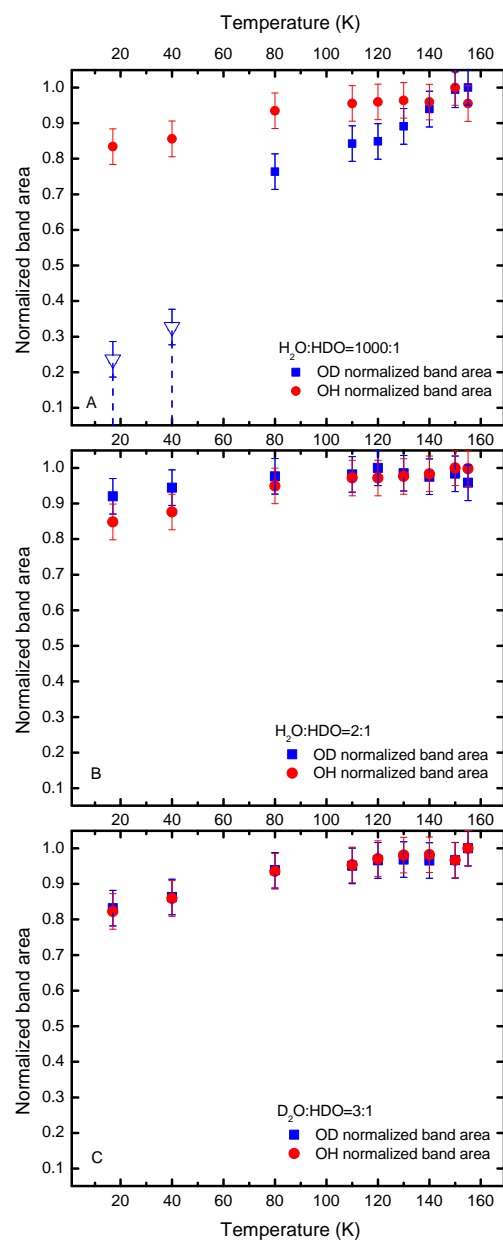


Figure 3.6: Normalized O-D and O-H stretching mode band areas as a function of temperature. Panel A: H₂O:HDO=1000:1; triangles and vertical dashed lines indicate upper limits for the measure; panel B: H₂O:HDO=2:1 mixture; panel C: D₂O:HDO=3:1.

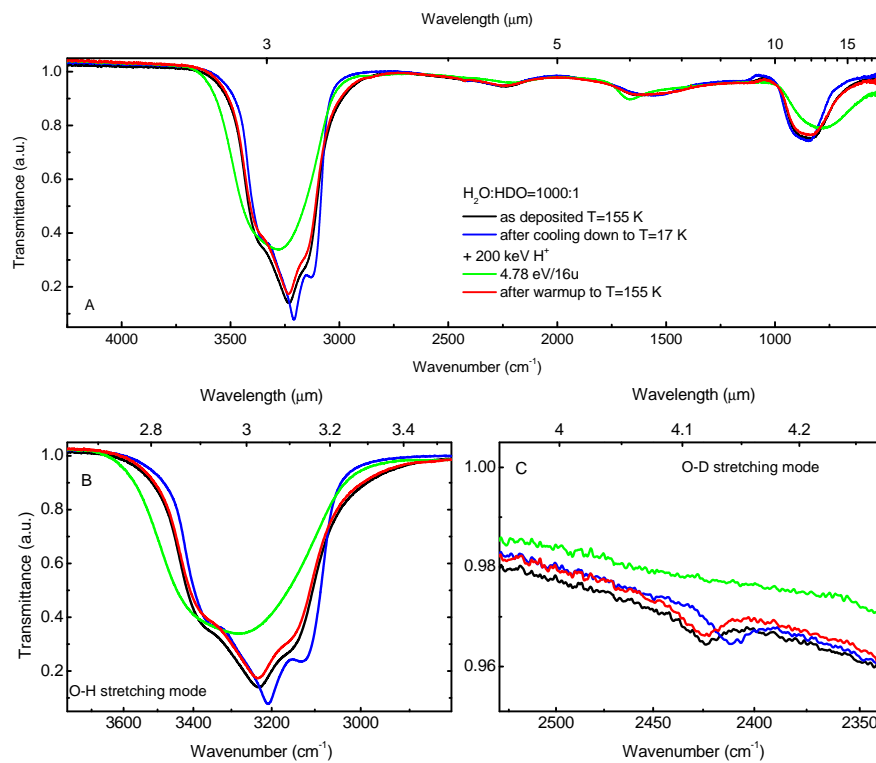


Figure 3.7: Infrared spectra in transmittance scale acquired during the irradiation experiments of crystalline $H_2O:HDO=1000:1$ with 200 keV H^+ . Panel A: whole spectra; panel B: O-H stretching mode band; panel C: O-D stretching mode band.

experiments with 200 keV H^+ . In the first experiment we deposited the $H_2O:HDO=1000:1$ mixture at 155 K (Fig. 3.7, black solid line), then we cooled down the sample to 17 K. This experiment was performed to verify that the disappearance of the O-D feature is due to the sample phase change and not to temperature variations. At 155 K the sample is deposited in the crystalline phase (see Leto & Baratta 2003). After the spectrum acquisition, we cooled down the sample to 17 K (blue solid line). The cooling determines the O-D stretching modes band shift from 2423 cm^{-1} to 2412 cm^{-1} (see Fig. 3.7, panel C). The green line in Fig. 3.7 shows the ice spectrum after the irradiation with 200 keV H^+ performed at 17 K. In particular, in Fig. 3.7 panel B it is possible to see that the O-H stretching mode band profile changed, becoming larger and decreasing in intensity. These changes testify that the irradiation caused the amorphization of the as deposited crystalline sample (e.g., Baratta et al. 1991; Leto & Baratta 2003; Dartois et al. 2015). After the irradiation, the O-D stretching modes band disappears because of the ion-induced amorphization. The warm up to 155 K induce the re-crystallization of the sample (red solid line), and the O-D feature appears again, centred at the same position it has been found in the as deposited sample.

In Fig. 3.8 we show the O-D and O-H band areas normalized to the initial value as a function of irradiation dose that we measured in the $H_2O:HDO=1000:1$ frozen mixture. The O-D experimental data were fitted with an exponential curve $y=e^{-\sigma D}$, where σ is the cross section of the process in $16u/eV$ and D is the dose in $eV/16u$. The fit allows to obtain the cross section $\sigma=1.4\pm 0.1$ in $16u/eV$.

Another experiment has been performed on a $H_2O:HDO=2:1$ solid mixture deposited and irradiated at 17 K. The spectra acquired are shown in Fig. 3.9. The most intense bands are the O-H stretching mode of water and the O-D stretching mode of deuterated water. At 17 K,

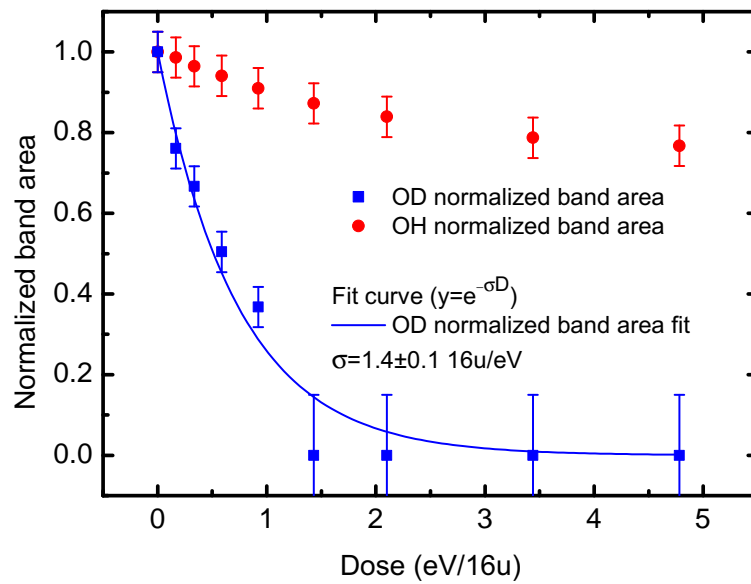


Figure 3.8: *O-D* and *O-H* features normalized areas after ion irradiation with 200 keV H^+ of a $H_2O:HDO=1000:1$ solid mixture at 17 K. The *O-D* experimental data have been fitted with an exponential curve $y=e^{-\sigma D}$, where σ is the cross section in $16u/eV$ and D is the dose in $eV/16u$.

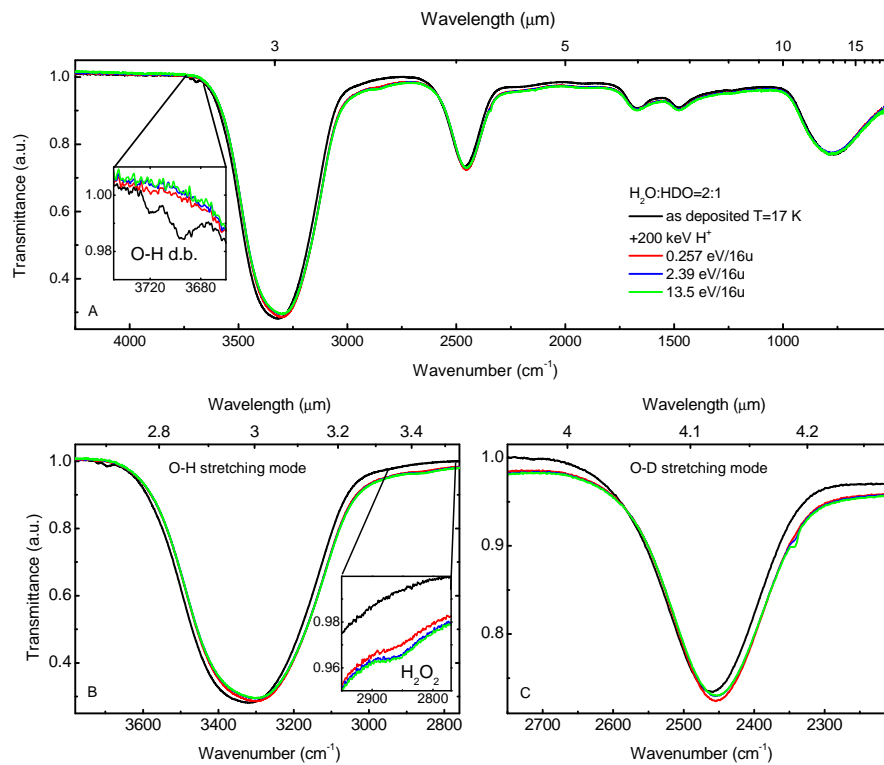


Figure 3.9: Infrared spectra in transmittance scale acquired during the irradiation of a H₂O:HDO=2:1 mixture with 200 keV H⁺. Panel A: whole spectra; inset: O-H dangling bonds; panel B: O-H stretching mode band; inset: H₂O₂ feature; panel C: O-D stretching mode band.

the sample is deposited as a porous and amorphous film, as testified by the presence of the O-H dangling bonds bands at 3692 and 3720 cm^{-1} in the spectrum acquired immediately after the deposition (black line, see the inset in Fig. 3.9 panel A). As expected, the irradiation with 200 keV H^+ caused the disappearance of the O-H dangling bond feature since the first irradiation step (red line in the figure), thus compaction took place (e.g., Palumbo 2006; Raut et al. 2007a; Dartois et al. 2013).

It is known that the ion irradiation of water induce the formation of hydrogen peroxide (e.g., Moore & Hudson 2000; Strazzulla et al. 2003; Zheng et al. 2006). H_2O_2 exhibit a vibrational feature at about 2850 cm^{-1} ($\sim 3.5 \mu\text{m}$). In the inset in Fig. 3.9 panel B the feature attributed to H_2O_2 found in the acquired spectra is shown. We did not find any evidence of HDO_2 nor D_2O_2 formation. In fact, excluding the H_2O_2 feature and a small contribution due to CO_2 contamination found at about 2340 cm^{-1} , the spectra acquired before and after irradiation are superimposable.

3.3.4 Other vibrational features in the 4.1 μm spectral range

The O-D feature falls in a region of the infrared spectrum where other astrophysically relevant species exhibit vibrational modes. A few examples are reported in Fig. 3.10, where spectra collected in the experimental setup described in § are shown. In the figure, the red curve shows the O-D stretching mode band in the crystalline $\text{H}_2\text{O}:\text{HDO}=1000:1$ mixture, while the purple curve shows the $\text{H}_2\text{O}:\text{HDO}=2:1$ mixture at 17 K. Close to the O-D stretching mode band of deuterated water, both amorphous (black line) and crystalline (blue line) methanol exhibit a combination mode band at about 2450 cm^{-1} (e.g., Allamandola et al. 1992; Sandford & Allamandola 1993; Bennett et al. 2007). In star-forming regions, its abundance varies from a few percent up to 30%

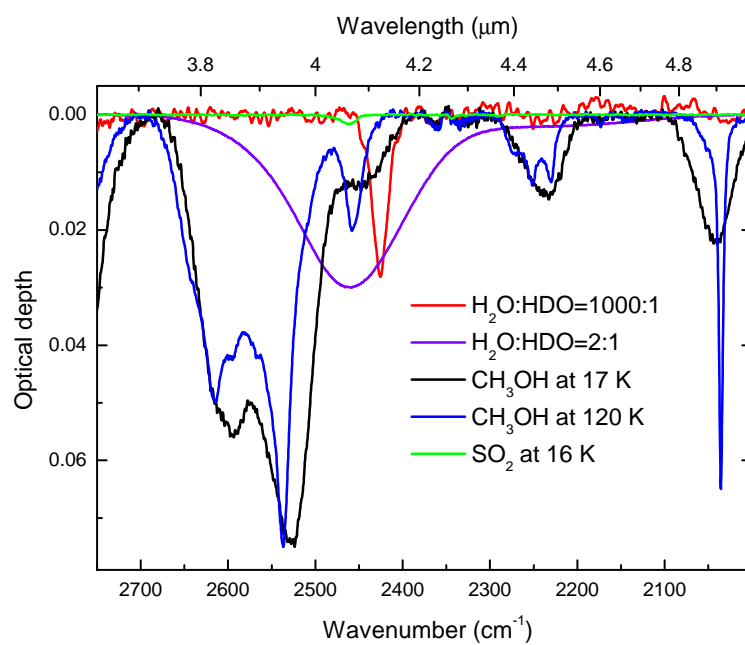


Figure 3.10: *The 4 μm region. Other vibrational bands can hinder the O-D stretching mode band. Scalare in abbondanze relative*

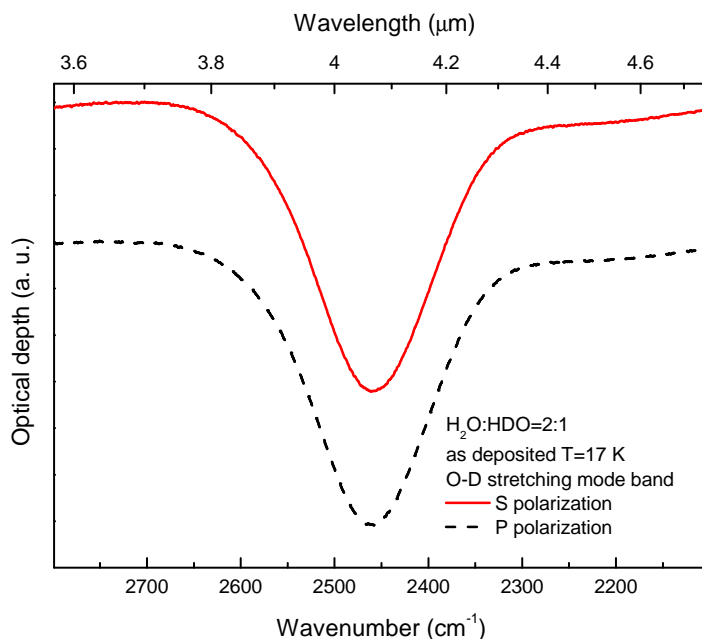


Figure 3.11: *Infrared spectra acquired in P-polarization (red line) and S-polarization (black line) on a H₂O:HDO=2:1 frozen mixture deposited at 17 K. The O-D stretching mode band profiles acquired in different polarization are superimposable.*

w.r.t. water (e.g., Allamandola et al. 1992; Boogert et al. 2008). Also SO₂ exhibits a combination mode at about 2460 cm⁻¹ (purple line, Giguère and Falk 1956; Wiener & Nixon 1956). Boogert et al. (1997) reported that its abundance span between 0.3% and 0.8% w.r.t. water. In the figure, for each species we scaled the spectra taking into account the band intensities observed toward W33 A, according to the detections reported by Allamandola et al. (1992), Boogert et al. (1997) and Teixeira et al. (1999).

Finally, Fig. 3.11 shows a comparison between the profile of the O-D stretching mode band in a H₂O:HDO=2:1 frozen mixture acquired both in P- and S-polarization. Within experimental uncertainties, the two

profiles are perfectly superimposable. This condition is verified also for the other astrophysically relevant mixtures investigated in this chapter. As discussed by Baratta et al. (2000) and Palumbo & Baratta (2000), when the band profile does not depend on the polarization mode, laboratory transmittance spectra directly correlate with the variation of the absorption coefficient in the solid sample. Hence, a direct comparison between laboratory spectra and astronomical observations is possible.

3.4 Discussion

The results reported in the previous section are in agreement with the experiments reported by Gálvez et al. (2006). In fact, when the abundance of deuterated water is of the order of 0.1 % or less, the infrared spectra acquired on amorphous deposited samples have shown that the 4.1 μm vibrational mode band is not detectable, while the feature can be revealed in crystalline samples. This phenomenon is related to the distribution of nearest neighbour oxygen-oxygen distances that is narrow for a ordered film, and becomes broad with the amorphization (e.g., Madden et al. 1978; Gálvez et al. 2006). Furthermore, we have shown that if a sample is deposited as a crystalline film and exposed to ion bombardment, the O-D stretching mode band disappears. This effect has to be ascribed to the ion-induced amorphization of water ice. The fit of the O-D normalized stretching band areas reported in Fig. 3.8 allowed us to obtain the cross section of the process $\sigma=1.4\pm0.1$ 16u/eV. This value is comparable to the cross section obtained by Leto & Baratta (2003) for 30 keV H^+ on crystalline water ice, $k=1.7\pm0.2$ molecule/eV, where 1 molecule = 18u.

In dense molecular clouds, water forms on the cold dust grains after grain surface reactions and its formation, as well as the formation of deuterated water, is regulated by the cloud characteristics. In particular, the dust temperature can affect the $\text{HDO}/\text{H}_2\text{O}$ ratio (e.g., Caselli & Ceccarelli 2012). According to Cazaux et al. (2011), if the dust temperature is lower than 15 K, the $\text{HDO}/\text{H}_2\text{O}$ ratio is predicted to be lower than 0.01%, reflecting the HD/H_2 ratio close to the interstellar D/H ratio $\simeq 1.5\times 10^{-5}$. If the temperature is above 15 K, the $\text{HDO}/\text{H}_2\text{O}$ ratio can be as high as a few %.

Taking into account the work by Cazaux et al. (2011), the results reported in this chapter suggest that when water and deuterated water are formed on cold (≤ 15 K) dust grains, the deuterated water abundance is too low and the $4.1 \mu\text{m}$ O-D stretching mode band could be detected only when HDO is embedded in crystalline icy mantles. On the other hand, when the dust grain temperature is above 15 K during water formation, the deuterated water/water ratio can be high enough to allow the O-D stretching mode band detection in amorphous ices also.

In the protostellar phase, the central object causes the presence of a thermal gradient in the surrounding matter, with the temperature increasing going toward the source. The thermal gradient determines whether molecules remain in the icy grain mantles or sublime, thus dust grains that are further from the heating object may preserve their icy grain mantles. Furthermore, icy mantles closer to the heating source can undergo the amorphous-to-crystalline transition while those in the outer regions remain amorphous because in those regions the temperature is not high enough to cause their crystallization and the time required to undergo crystallization at lower temperature is higher than the age of these objects (e.g., Schmitt et al. 1988; Baragiola 2003).

In this scenario a correct estimation of the HDO/H₂O requires the observations of both the O-H stretching mode band at $3.03 \mu\text{m}$ and the O-D stretching mode band at $4.1 \mu\text{m}$. In fact the profile of the non saturated $3.03 \mu\text{m}$ band gives an estimation of the fraction of crystalline ice along the line of sight (e.g., Leto & Baratta 2003) which in turn gives an estimation of the average temperature along the line of sight. As shown in Fig. 3.6 the ratio between the 3.03 and the $4.1 \mu\text{m}$ band area is independent of the temperature of the sample when the concentration of HDO is of the order of few percent while it strongly depends on the temperature of the sample when the concentration of HDO is of the

order of 0.1 % or less.

To date, the presence and abundance of deuterated water in the solid phase of star-forming regions is still under debate. The main reason is due to the low amount of data available for the 4.1 μm spectral region. In fact, observations by means of ground-based infrared telescopes are hindered by the atmospheric CO_2 absorption. Thus, only space-telescopes can be used to observe the O-D stretching mode band. Also, as we have shown in Fig. 3.10, the presence of other solid-phase interstellar molecule vibrational features close to the O-D stretching mode band frequency could drive to misleading considerations about the presence and the abundance of deuterated water in icy grain mantles. In particular, the contribution in the band intensity of the 4.1 μm band due to the presence of methanol and sulphur dioxide has to be taken into account, in order to avoid overestimating the HDO abundance.

We expect that the higher sensitivity of the detectors on board the JWST, whose launch is scheduled between March and June 2019, will allow to spread light about the presence of deuterated water together with other minor species that are thought to be present in icy grain mantles, and that have not been observed yet. Also, the resolution of these detectors could allow to disentangle the O-D stretching mode band from those related to CH_3OH and SO_2 .

Water ice is largely present in the Solar System in a number of surfaces of planets, moons, comets and rings (e.g., Schmitt et al. 1998). Its detection is mainly based on reflectance near-IR spectra. In fact, the spectrum of solid water shows two absorption features at about 2.0 and 1.5 μm (5000 and 6600 cm^{-1} ; e.g. Grundy & Schmitt 1998; Gerakines et al. 2005; Mastrapa & Brown 2006). In an amorphous sample these features are smooth and symmetric, while in crystalline samples an additional feature appears at about 1.65 μm (6060 cm^{-1}). Laboratory experiments have shown that the relative intensity of this latter feature

increases as the temperature of the crystalline sample decreases. Based on these results Grundy et al. (1999) have studied the possibility to use the $1.65 \mu\text{m}$ feature seen in reflectance spectra obtained by ground based observations to evaluate the surface temperatures on satellites of Jupiter, Saturn and Uranus.

Gas phase deuterated water has been detected in various Solar System objects (e.g., Hartogh et al. 2011). According to current models, at the time of Solar System formation, water in the outer regions of the disc would preserve its original high D/H ratio from the molecular cloud (e.g., Hallis 2017). Thus it cannot be excluded that solid HDO mixed with H_2O is present on icy bodies (such as the satellites of Jupiter, Saturn and Uranus and TNOs) in the outer Solar System. Detection of solid HDO requires observations in the $4 \mu\text{m}$ spectral region which are very challenging with present available instrumentation but which could be obtained in the near future with the JWST. The simultaneous observation of the $1.65 \mu\text{m}$ and $4.1 \mu\text{m}$ features will allow to better constrain the crystalline structure and the temperature of the ice and the $\text{H}_2\text{O}:\text{HDO}$ ratio.

Part III

Synthesis and desorption: the role of energetic processing

Chapter 4

Synthesis of formamide and isocyanic acid after ion irradiation of frozen gas mixtures

Based on Kaňuchová, Z., Urso, R. G., Baratta, G. A., Brucato, J. R., Palumbo, M. E. & Strazzulla, G. 2016, *Astronomy & Astrophysics*, 585, A155

4.1 The role of energetic processing in the synthesis of prebiotic molecules

It is commonly thought that energetic processing of interstellar and planetary ices plays a relevant role in astrochemistry and astrobiology. There is also wide consensus that many complex molecules possibly formed in ice mantles on interstellar grains are not observable in the solid phase by IR spectroscopy (Allodi et al. 2013). It is also believed that the desorption of grain mantle species into the gas phase after warming by a protostar or sputtering by energetic cosmic ions, for example, gives an important contribution to the gas phase composition (Modica & Palumbo 2010; Palumbo et al. 2008). In this chapter we present the formation of formamide (NH_2CHO) and isocyanic acid (HNCO) after ion irradiation of ice mixtures ($\text{H}_2\text{O}:\text{CH}_4:\text{N}_2$, $\text{H}_2\text{O}:\text{CH}_4:\text{NH}_3$ and $\text{CH}_3\text{OH}:\text{N}_2$).

Formamide is of considerable interest in prebiotic chemistry. Formamide and isocyanic acid have been observed as gaseous species in several astronomical environments such as cometary comae (e.g. Bockelèe-Morvan et al. 2000; Biver et al. 2014); a new and extended set of recent gas phase observations of several high-, intermediate-, and low-mass pre- and protostellar objects has reinforced the interest in these molecules (Mendoza et al. 2014; López-Sepulcre et al. 2015). Formamide has also been tentatively identified in the solid phase in ISO-SWS infrared spectra (Schutte et al. 1999; Raunier et al. 2004). As a result of observations, some authors (Mendoza et al. 2014; López-Sepulcre et al. 2015) concluded that these two species are chemically related in star-forming regions and that at least formamide has to be produced in the solid phase and then released in the gas phase by ther-

mal annealing. We note, however, that this view has recently been challenged by Barone et al. (2015), who have shown on the basis of theoretical calculations that formamide can be formed in the gas phase provided that its precursors, NH_2 and H_2CO , are available.

This scenario stimulates the experimental studies of solid phase chemistry and in particular of the two main mechanisms that drive the chemical evolution of icy mantles in the interstellar medium (ISM), namely surface chemistry and energetic processing. Recent experiments of hydrogenation of isocyanic acid exclude the possibility that noteworthy quantities of formamide can be formed (Noble et al. 2015).

On the other hand, previous studies have shown that processing of various ice mixtures by UV photons (Bernstein et al. 1995; Henderson & Gudipati 2015), energetic electrons (Jones et al. 2011; Bergantini et al. 2014; Henderson & Gudipati 2015), and ions (Gerakines et al. 2004; Demyk et al. 1998) produce both formamide and isocyanic acid. The experimental results obtained so far are discussed in some detail in Sect. .

Here we extend these results and present a detailed quantitative measurement of the amount of synthesized formamide and isocyanic acid after ion bombardment of ice mixtures ($\text{H}_2\text{O}:\text{CH}_4:\text{N}_2$, $\text{H}_2\text{O}:\text{CH}_4:\text{NH}_3$, and $\text{CH}_3\text{OH}:\text{N}_2$). In addition, some experiments performed on pure frozen formamide that have been published (Brucato et al. 2006) are re-analysed here. The results are discussed in the light of their astrophysical relevance, and we demonstrate that energetic processing of ice can quantitatively reproduce the amount of NH_2CHO observed in cometary comae and in many circumstellar regions. HNCO is also formed, but additional formation mechanisms are required to quantitatively account for the astronomical observations.

4.2 Energetic processing

4.2.1 Previous experiments

Because it is generally agreed that hydrogenation reactions dominate the grain surface chemistry by saturating the molecules present in ice mantles, it seems obvious to assume that formamide is formed by hydrogenation of HNCO. Surprisingly, however, recent experiments have demonstrated that the hydrogenation of HNCO does not produce detectable amounts of formamide (Noble et al. 2015).

Several studies of energetic processing, with photons, electrons, and ions of different icy mixtures, have shown the formation of formamide and isocyanic acid. Bernstein et al. (1995) demonstrated the formation of formamide, acetamide, ethanol, and nitriles during the warming up of photolyzed samples made of ice mixtures containing H₂O, CH₃OH, CO, and NH₃. Henderson & Gudipati (2015) have recently detected formamide produced by UV Lyman-alpha photons and energetic electrons by two-step laser ablation and ionization mass spectrometry. A detailed mechanistical study of the production of formamide after energetic electron bombardment of several CO:NH₃ ice mixtures has been presented by Jones et al. (2011). It has also been suggested that formamide is one of the products of ion irradiation and photolysis of H₂O:HCN (Gerakines et al. 2004) or CO:NH₃ (Demyk et al. 1998) at low temperature (18 K). In addition, samples of pure formamide ice were irradiated with 200 keV protons (Brucato et al. 2006), and new molecules were synthesized, among which CO, CO₂, N₂O, HNCO, NH₄⁺ and OCN⁻.

This work adds new experimental data on energetic processing of ice mixtures, and it is also the first to furnish a quantitative measurement

of the molecular number ratio $\text{HNCO}/\text{NH}_2\text{CHO}$ obtained from experiments that can be usefully compared with astronomical observations.

4.2.2 Experimental apparatus

Gaseous mixtures ($\text{H}_2\text{O}:\text{CH}_4:\text{N}_2$, and $\text{H}_2\text{O}:\text{CH}_4:\text{NH}_3$ and $\text{CH}_3\text{OH}:\text{N}_2$) were prepared in a vacuum chamber and were admitted through a needle valve into the scattering chamber ($P < 10^{-7}$ mbar), where they accreted onto a cold (10–20 K) silicon or KBr substrate. Infrared transmittance spectra (resolution of 1 cm^{-1}) were obtained before and after several steps of ion bombardment by FTIR spectrophotometers (Bruker Equinox 55 or Bruker Vertex 70). The substrates were in thermal contact with a closed-cycle helium cryostat (10–300 K).

An ion implanter (200 kV; Danfysik 1080-200) generated energetic ions (up to 200 keV per single ionization) that irradiated the sample on a spot greater than the area probed by the infrared beam (for more details on the experimental set-up see Strazzulla et al. 2001).

We here present experiments obtained by irradiating the samples with 30–200 keV H^+ or He^+ ions. The ion fluence in ions cm^{-2} was measured by a charge integrator and continuously monitored during irradiation. The substrate plane was placed at an angle of 45 degrees with respect to the IR beam and the ion beam so that spectra were taken in situ, even during irradiation, without tilting the sample.

The IR bands of a given molecule were used to measure the column density N in units of molecules cm^{-2} through the formula:

$$N = \frac{\int \tau(\nu) d\nu}{A}, \quad (4.1)$$

where τ_ν is the optical depth and A is the band strength (cm molecule^{-1}). The band strengths are listed in Table 4.1 together with band peak positions, assignments, and references.

Some of the experiments were performed by preparing frozen samples thinner than the penetration depth of the impinging ions that pass

through the target and by obtaining the IR spectra at various steps of irradiation. Other experiments were made by irradiating the sample during its deposition, building up a larger thickness of processed material. In this way, the resulting spectrum better shows the weaker bands of the newly synthesized molecules. In the first case the energy deposited by incoming ions was obtained by calculating the stopping power (i.e. the amount of energy deposited per unit path length; $\text{eV cm}^2/\text{molecule}$) of a given ion in a given target (SRIM code, Ziegler et al. 2008). By multiplying this number times the number of bombarding ions per square centimeter, we obtained the amount of energy released to the sample (dose) in eV per molecule. As usual, we express the dose in $\text{eV}/16\text{u}$, a convenient way to characterize chemical changes and to enable a comparison with other experiments with different samples.

Other samples are thicker than the penetration depth of the impinging ions that remain implanted in the target. In this case the dose was calculated by assuming that the energy of the incoming ion is uniformly absorbed by target molecule along the penetration depth of the ion.

For a simultaneous deposition of ices and irradiation, the energy released to the target molecules is estimated from the measurement of the ion flux ($\text{ions cm}^{-2}\text{s}^{-1}$), the energy of impinging ions (eV), and the accretion rate of the frozen film ($\text{molecules cm}^{-2} \text{s}^{-1}$). In all of the experiments we used low current densities ($0.001\text{--}0.1 \mu\text{A cm}^{-2}$) to avoid macroscopic heating of the target.

Table 4.1: Peak positions, vibration modes, molecule assignments, and band strengths. References: (1) *Bru-
cato et al. (2006)*; (2) *van Broekhuizen et al. (2004)*

Peak position cm^{-1}	Vibration	Assign.	Band strengths ($\times 10^{-17} \text{cm molecule}^{-1}$)	Ref.
1388	ν_6 in plane CH sc.	NH ₂ CHO	0.68	(1)
2260	N=C=O stretch	HNCO	7.2	(2)

4.2.3 Results

Formamide

Frozen layers of pure formamide were deposited at low temperature (20 K) and irradiated with 200 keV H^+ ions. In Fig. 4.1 (top panel) we show IR transmittance spectra ($2400\text{--}1250\text{ cm}^{-1}$ ($4.17\text{--}8.0\text{ }\mu\text{m}$)), in optical depth scale, of a deposited layer of formamide before and after irradiation at a dose of $12\text{ eV}/16\text{u}$. The thickness of the deposited layer was about 4900 \AA , that is, less than the penetration depth of 200 keV H^+ ions (about $2\text{ }\mu\text{m}$) in formamide, as calculated using the SRIM software (Ziegler et al. 2008).

The spectrum of formamide in the considered spectral range exhibits four bands at 1708 , 1631 , 1388 , and 1328 cm^{-1} before radiation (for more detail see Brucato et al. 2006). The decrease of the intensity of these bands and the appearance of new bands is evident from the figure and testifies to the formation of molecular species as indicated in the labels of Fig. 4.1 (top panel).

In the spectral range considered in Fig. 4.1, CO and CO_2 absorption bands are observed at 2140 and 2342 cm^{-1} , respectively. The bands observed at 2260 cm^{-1} and 2240 cm^{-1} are assigned to isocyanic acid (HNCO) and nitrous oxide (N_2O), respectively. The weak band at 2083 cm^{-1} is due to the CN stretching mode in HCN. The presence of the SiH stretching band observed at 1997 cm^{-1} is owing to the fraction of protons that entirely cross the ice sample and are implanted into the silicon substrate. Another intense band, located at 2165 cm^{-1} , is commonly assigned to the cyanate anion OCN^- (Grim and Greenberg

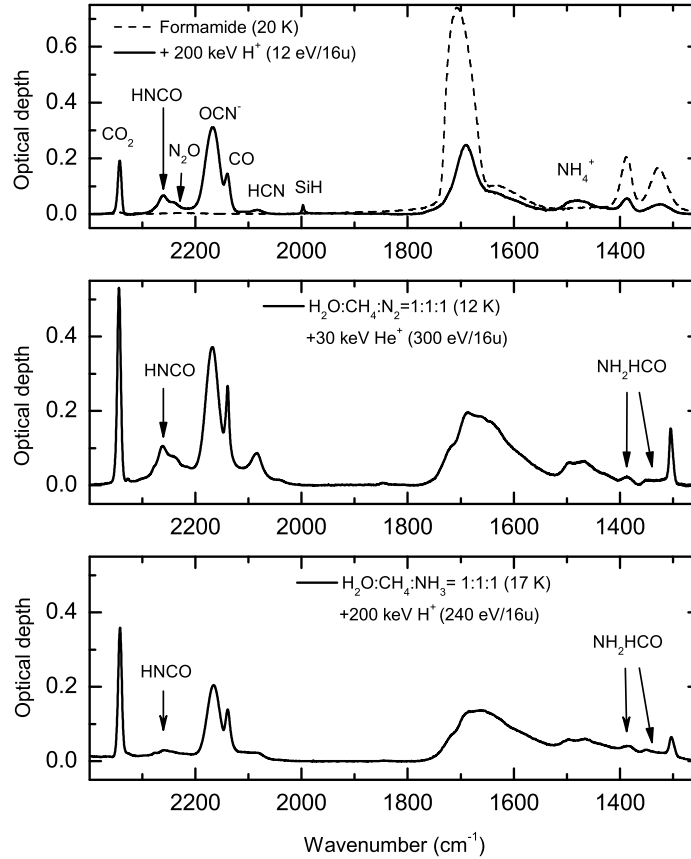


Figure 4.1: IR transmittance spectra ($2400\text{--}1250\text{ cm}^{-1}$ ($4.17\text{--}8.0\text{ }\mu\text{m}$)), in optical depth scale. The top panel shows the spectrum of formamide (20 K) after irradiation at a dose of 12 eV/16u with 200 keV H⁺ ions (full line). The main species formed after irradiation are labelled. The spectrum obtained before irradiation is also shown for comparison (dotted line). The middle panel shows the spectrum of a mixture H₂O:CH₄:N₂ (1:1:1) deposited at 12 K and while being irradiated by ions at a dose of about 300 eV/16u. Absorption features assigned to HNCO and NH₂CHO are labelled. The bottom panel shows the spectrum of a mixture H₂O:CH₄:NH₃ (1:1:1) as deposited at 17 K and after irradiation with 200 keV H⁺ of about 240 eV/16u. Absorption features assigned to HNCO and NH₂CHO are labelled.

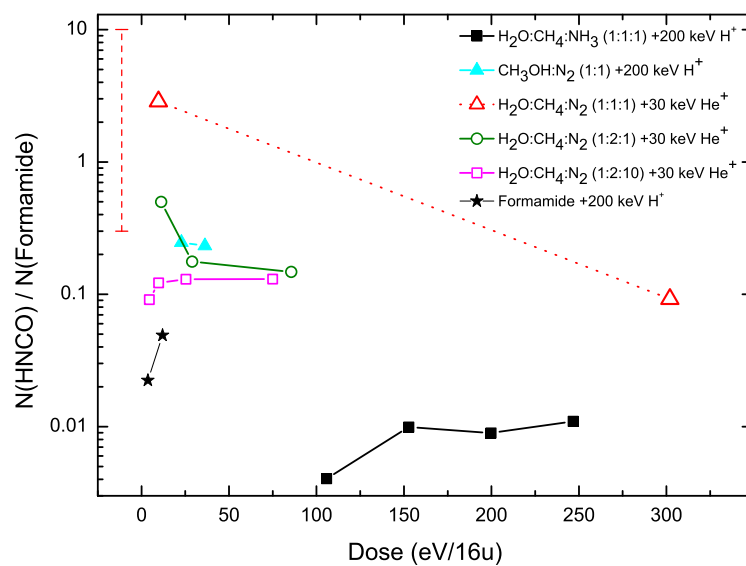


Figure 4.2: Molecular number ratio $\text{HNCO}/\text{NH}_2\text{CHO}$ obtained after ion bombardment of different frozen ice mixtures is plotted vs irradiation dose ($\text{eV}/16\text{u}$). The dashed vertical line represents the range of values measured in astronomical sources.

1987; Hudson et al. 2001; van Broekhuizen et al. 2004). Evidence that the ammonium cyanate complex $\text{NH}_4^+\text{OCN}^-$ is formed is given by the band at 1478 cm^{-1} , which is ascribed to NH_4^+ (Raunier et al. 2004).

Figure 4.2 gives the column density ratio of $\text{HNCO}/\text{NH}_2\text{CHO}$ as a function of irradiation dose. It was obtained from the bands at 2260 cm^{-1} (HNCO) and 1388 cm^{-1} (NH_2CHO) using the band strength values reported in Table 1. The HNCO band area was obtained by fitting the feature in the spectral range between $2270\text{--}2220\text{ cm}^{-1}$ with two Gaussian curves peaked at 2260 cm^{-1} and 2240 cm^{-1} that are assigned to HNCO and N_2O , respectively. The resulting error on the HNCO integrated optical depth is of the order of a few percent.

$\text{H}_2\text{O}:\text{CH}_4:\text{N}_2$ mixtures

Mixtures of $\text{H}_2\text{O}:\text{CH}_4:\text{N}_2$ (1:1:1) were deposited at 12 K and were at the same time irradiated with 30 keV He^+ beams. Experiments were conducted at low (about $10\text{ eV}/16\text{u}$) and high (about $300\text{ eV}/16\text{u}$) dose. In Fig. 4.1 (middle panel) we present the IR transmittance spectrum ($2400\text{--}1250\text{ cm}^{-1}$ ($4.17\text{--}8.0\ \mu\text{m}$)) of such a mixture while it was irradiated by ions at a dose of about $300\text{ eV}/16\text{u}$. This spectrum clearly shows two features at 1388 and 1330 cm^{-1} that demonstrate the formation of formamide after ion bombardment. In the spectrum of the irradiated mixture we observe bands at about 1310 cm^{-1} and at about 1600 cm^{-1} , which are due to the original frozen methane and water molecules, respectively. All of the other bands are formed after ion bombardment. In addition to formamide, we observe the appearance of the same bands observed after irradiation of formamide, although with different relative abundances: CO and CO_2 at 2140 and $2342\text{ cm}^{-1}\text{u}$, respectively; HNCO (2260 cm^{-1}), N_2O (2240 cm^{-1}), OCN^- (2165 cm^{-1}), HCN (2083 cm^{-1}), and NH_4^+ (1478 cm^{-1}).

The column density ratio of $\text{HNCO}/\text{NH}_2\text{CHO}$ was obtained by mea-

asuring their column density according to Eq.1 using the area of the bands at 2260 cm^{-1} (HNCO) and at 1388 cm^{-1} (formamide) and their band strengths given in Table 1. The results are reported in Fig. 4.2: the ratio at a low dose of irradiation values is about 3 and decreases to about 0.1 for high-dose irradiation. Moreover, in this case the HNCO band area was obtained by fitting the feature in the spectral range between $2270\text{--}2220\text{ cm}^{-1}$ with two Gaussian curves peaked at 2260 cm^{-1} and 2240 cm^{-1} , which are assigned to HNCO and N_2O , respectively.

We performed additional experiments by changing the stoichiometry of the initial mixtures: $\text{H}_2\text{O}:\text{CH}_4:\text{N}_2=1:2:1$; $=1:2:10$; and $=1:2:100$. These experiments were conducted with thick targets (i.e. larger than the penetration depth of the used ions) deposited at low T ($15\text{--}20\text{ K}$) and then irradiated with 30 keV He^+ beams. The obtained column density ratios are plotted in Fig. 4.2. For these mixtures we also measured the total amount of deposited nitrogen atoms from which we obtained the fraction of nitrogen atoms that react to form HNCO and formamide. The results are plotted in Fig. 4.3 where the column density of HNCO and formamide formed after ion bombardment of the different mixtures is presented as the ratio to the total nitrogen atoms present before irradiation and plotted vs irradiation dose ($\text{eV}/16\text{u}$).

Figure 4.2 shows that the ratio of $\text{HNCO}/\text{NH}_2\text{CHO}$ decreases with the increase of nitrogen content (it is not measurable for the $1:2:100$ mixture). Figure 4.3 clearly shows that both HNCO and formamide are formed less efficiently when the mixture is dominated by nitrogen; formamide is below the detection limit of our technique for the $1:2:100$ mixture. The results are expected: it is reasonable that molecules that need H, C, N and O to be formed are less efficiently formed when one of the atoms dominates the mixture and the C- and O-bearing species are dispersed in a matrix dominated by nitrogen.

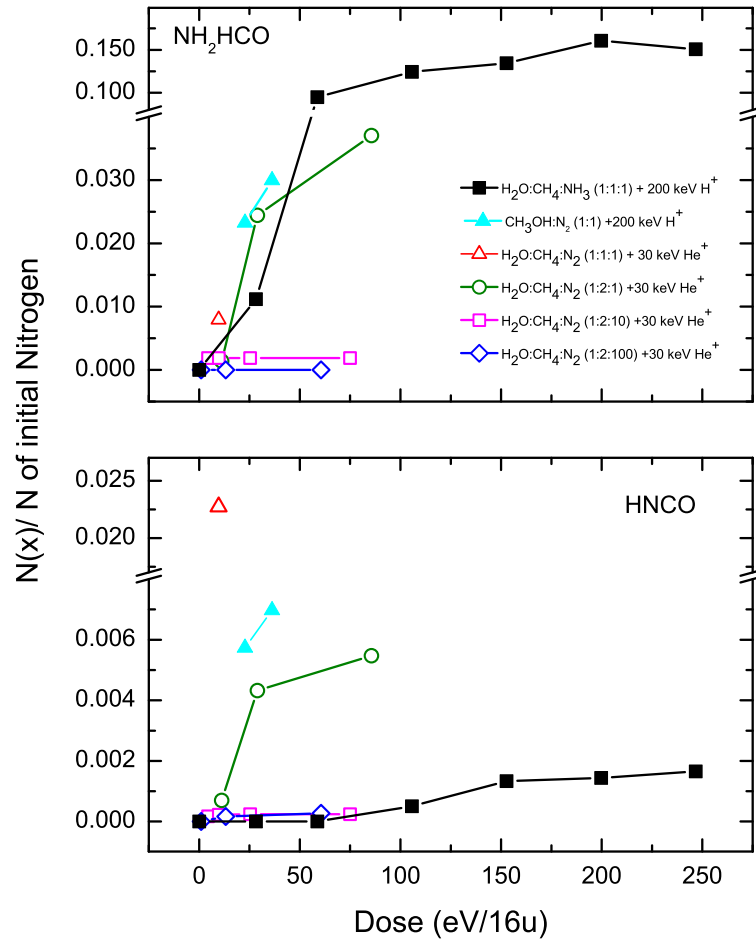


Figure 4.3: Column density of HNCO and formamide formed after ion bombardment of different frozen ice mixtures shown as the ratio to the total nitrogen atoms present in the mixtures before irradiation and plotted vs irradiation dose (eV/16u).

H₂O:CH₄:NH₃ mixture

We prepared a thin frozen mixture of H₂O:CH₄:NH₃ (1:1:1) at 17 K and after deposition irradiated it with 200 keV H⁺ beams. From a qualitative point of view we observe the formation of the same bands as for the previous mixtures, but with different relative intensities. A comparison of the spectra in Fig. 4.1 shows that substituting molecular nitrogen with ammonia causes a noteworthy increase in the relative amount of formamide with respect to that of isocyanic acid. This is made more clear in Fig. 4.2 where the ratio of the two species (HNCO/NH₂CHO) shows a behaviour completely different from the one of the mixtures with molecular nitrogen.

When ammonia is present, the amount of formed HNCO is much lower than that of formamide. Figure 4.3 shows that formamide is efficiently produced by incorporating up to about 15% of the initial nitrogen. HNCO is detected only at high dose, probably formed from species different from those deposited in the mixtures such as formamide itself.

CH₃OH:N₂ mixture

We prepared a frozen mixture of CH₃OH:N₂ (1:1) as a thin film at 16 K and after deposition irradiated it with 200 keV H⁺ beams. We here also observe the formation of isocyanic acid and formamide, whose column density ratio is plotted in Fig. 4.2. The obtained values are clearly similar to those obtained with the molecular nitrogen containing ternary mixtures. This consistency is confirmed by the data reported in Fig. 4.3, which show a ratio of HNCO/(initial nitrogen atoms) of about 6–7 per mill and a ratio of 2–3 per cent for formamide/(initial nitrogen atoms).

The quantitative results reported in Fig. 4.3 are consistent with pre-

vious experimental results. Bernstein et al. (1995) reported a quantity of about 1.8% (with respect to original nitrogen) of formamide in the residue formed after UV photolysis and thermal processing of methanol-containing interstellar ice analogues. Jones et al. (2011) found an abundance of formamide of about 1-2% after 60 minutes of electron bombardment of CO:NH₃ mixtures at 12 K. Gerakines et al. (2004) found an abundance of about 2% after 0.8 MeV proton irradiation of H₂O:HCN and H₂O:NH₃:HCN ice mixture at a dose of 10 eV/mol.

4.3 Discussion

Water (H_2O), carbon monoxide (CO), carbon dioxide (CO_2), methanol (CH_3OH), methane (CH_4), and ammonia (NH_3) are the most abundant molecular species detected in the interstellar medium in the solid phase (e.g. Gibb et al. 2004; Öberg et al. 2011). These species are also observed in cometary comae (e.g. Bockelèe-Morvan et al. 2000). Molecular nitrogen, being a homonuclear molecule without any infrared active band, cannot be directly observed in icy grain mantles, but its presence is deduced from the depletion of gas-phase species (e.g. Caselli et al. 2002; Bergin et al. 2002). Recently, molecular nitrogen has been detected in comet 67P/Churyumov-Gerasimenko (Rubin et al. 2015). In the present study we have considered binary and ternary mixtures with H- O- C- and N-bearing species (i.e. H_2O , CH_3OH , CH_4 , NH_3 and N_2). All these mixtures are reasonably representative of the composition of interstellar icy grain mantles and cometary ices. For the $\text{H}_2\text{O}:\text{CH}_4:\text{N}_2$ mixture we also considered different initial ratios to investigate how the relative abundance of a given species can affect the results.

4.3.1 Pre- and proto-stellar regions

Solid-phase formamide has been tentatively identified in ISO-SWS infrared spectra of the protostellar objects NGC 7538 IRS9 and W33A (Rubin et al. 2015; Raunier et al. 2004). The observations in the gaseous phase are more reliable. Its first detection was towards Sgr B2 (Rubin et al. 1971), and it was subsequently observed in molecular clouds and high-mass star-forming regions (Nummelin et al. 2000; Bisschop et al. 2007; Motiyenko et al. 2012). HNCO has not yet been observed in the solid phase, although it is believed to be present, formed by surface

chemistry or energetic processing, and to be responsible for the formation of the abundant cyanate ion OCN^- (e.g. Soifer et al. 1979; Demyk et al. 1998; Lowenthal et al. 2002; van Broekhuizen et al. 2005). It has been observed in the gas phase in numerous pre- and proto-stellar regions (Bisschop et al. 2007; Marcelino et al. 2009; Rodríguez-Fernández et al. 2010).

An extended set of recent observations of both formamide and isocyanic acid have renewed the interest in these molecules (Mendoza et al. 2014; López-Sepulcre et al. 2015). Mendoza et al. (2014) studied these molecules and observed their emission in the protostellar shock regions L1157-B1 and L1157-B2 with the IRAM 30 m radio-telescope. By comparing their results with those already available, they found a linear correlation between the abundances of the two molecules, with HNCO being about three times more abundant than NH_2CHO . This implies that the two species are chemically related. The authors suggested molecule formation on icy grain mantles. Further observations of ten low- and intermediate-mass pre- and proto-stellar objects allowed detecting HNCO in all of the sources and NH_2CHO in only five of them (López-Sepulcre et al. 2015). An almost linear correlation between HNCO and NH_2CHO abundances was confirmed. The fractional abundance (with respect to molecular hydrogen) of HNCO varies from source to source between 2×10^{-10} and 10^{-7} and the fractional abundance of NH_2CHO varies between 2×10^{-11} and 10^{-8} (Mendoza et al. 2014).

When all of the available observations are considered in a graph where the ratio $\text{HNCO}/\text{NH}_2\text{CHO}$ is plotted vs the luminosity of the source (which spans over six orders of magnitude; see the bottom panel of Fig. 3 in López-Sepulcre et al. 2015), the objects are concentrated in two regions. The first contains objects with a very high ratio (i.e. no or very few formamide has been detected), the other region con-

tains sources for which the two molecules are observed and the ratio spans between about 10 and 0.3. The sources without formamide detection are also the coldest and devoid of hot corinos. The authors concluded that while HNCO can be formed in the gas-phase during the cold stages of star formation, formamide forms mostly on the mantles of dust grains at low temperatures and is expelled into the gas phase when the temperature rises enough to sublimate the icy grain mantles.

Recently, Barone et al. (2015) have studied the reaction $\text{NH}_2 + \text{H}_2\text{CO} \rightarrow \text{NH}_2\text{CHO} + \text{H}$ in theory and found that it can efficiently form formamide in the gas-phase in star-forming regions. They therefore concluded that there is no need to invoke grain-surface chemistry to explain the presence of formamide provided that its precursors NH_2 and H_2CO are available in the gas phase.

Here we presented the results of laboratory experiments that show the formation of HNCO and NH_2CHO after ion bombardment of astrophysical relevant ice mixtures. We have found that at low dose (about 10 eV/16u; Fig. 4.3), the amount of NH_2CHO formed is of the order of a few percent with respect to available nitrogen in the ice mixtures, while the amount of HNCO formed is about one order of magnitude less. The cosmic abundance of nitrogen, as reported by Asplund et al. (2009), is 6.8×10^{-5} . In their study of dark clouds, Maret et al. (2006) adopted an elemental nitrogen fractional abundance of 2×10^{-5} . If we take into account the value given by Maret et al. (2006), and if we assume that in dense cold protostellar regions most nitrogen is in the solid phase, then the amount of NH_2CHO that can be formed in icy grain mantles can be as high as 10^{-7} with respect to hydrogen. Similarly, the amount of HNCO can be as high as 10^{-8} with respect to hydrogen. When the column density ratio HNCO/ NH_2CHO is plotted versus dose (see Fig. 2), we note that at the dose values we investigated, the ratio obtained in laboratory is in most cases lower than the ratio observed in star-forming

regions (López-Sepulcre et al. 2015). These experimental results indicate that while the observed amount of formamide can be accounted for by cosmic-ray bombardment of icy grain mantles, other processes (such as gas-phase and grain-surface reactions) have to be taken into account to explain the observed gas-phase abundance of HNC. This suggestion is based on the assumption that after desorption of ice grain mantles, molecules released to the gas phase do not suffer from further processing.

To estimate the time necessary to obtain in star-forming regions the effects observed in the laboratory, we considered the approximation of effective monoenergetic 1 MeV protons (Mennella et al. 2003). Furthermore, our experimental results were obtained using 200 keV protons or 30 keV He ions. To extrapolate the laboratory results to the interstellar medium conditions, we therefore assumed that they scale with the stopping power (S , energy loss per unit path length) of impinging ions (e.g. Palumbo 2006; Sicilia et al. 2012). Then the time is given by

$$t_{ISM} = \frac{S_{lab} \times Fluence_{lab}}{S_{ISM} \times \Phi_{ISM}}, \quad (4.2)$$

where S_{lab} and S_{ISM} are the stopping power of 200 keV protons (or 30 keV He⁺) and 1 MeV protons as obtained from SRIM software (Ziegler et al. 2008), respectively. $Fluence_{lab}$ is the fluence (ions cm⁻²) as measured during the experiments, and Φ_{ISM} is the flux (ions cm⁻² s⁻¹) of 1 MeV protons in star-forming regions. This has to be regarded as an effective quantity: it represents the equivalent flux of 1 MeV protons that gives rise to the ionization rate produced by the cosmic ray spectrum if 1 MeV protons were the only source for ionization (Mennella et al. 2003). Table 4.2 gives the time required in star-forming regions calculated assuming different values of the ionization rate (ζ^{H_2} (s⁻¹)), as reported by Mennella et al. (2003), Podio et al. (2014), and Woods et al. (2015). The ionization rate values we considered fall in the range

Table 4.2: *Time scales (years) to accumulate a dose of 1, 10 and 100 eV/16u by cosmic ion irradiation of icy mantles of dust grains in pre- and proto-stellar regions. The time scales have been estimated for different hydrogen ionization rates (ζ^{H_2} (s^{-1})) in the range measured in different regions.*

dose (eV/16u)	timescale (years)			
	ionization rate (s^{-1})			
	1.3×10^{-17}	6×10^{-17}	3×10^{-16}	1.3×10^{-15}
1	1.1×10^7	2.5×10^6	5.0×10^5	1.1×10^5
10	1.1×10^8	2.5×10^7	5.0×10^6	1.1×10^6
100	1.1×10^9	2.5×10^8	5.0×10^7	1.1×10^7

predicted by models (e.g. Padovani et al. 2009, 2013).

The lifetime of pre- and proto-stellar phases have been estimated to be of the order of 10^5 – 10^7 years (Larson 2003; Caselli & Ceccarelli 2012), thus the results presented in the table demonstrate that the dust has the chance of accumulating a dose of the order of a few eV/16u before the ices desorb. Thus we suggest that most of the formamide observed in these regions is formed by energetic processing of ices.

4.3.2 Comets

Formamide and isocyanic acid have also been observed in the coma of some comets. HNC/NH₂CHO has been measured for three comets: in the long-period C/1995 O1 Hale-Bopp (Bockelè-Morvan et al. 2000), and recently in comets C/2012 F6 (Lemmon) and C/2013 R1 (Lovejoy) (Biver et al. 2014). It is interesting to note that the molecular number ratios HNC/NH₂CHO are 5 (in the coma of Hale-Bopp), 1.6 (Lemmon), and 1 (Lovejoy). These values are interestingly compatible with those measured in the pre- and proto-stellar regions of young stars. The existence of a link between the composition of the interstellar material and comets has been suggested for a long time (e.g. Greenberg 1982).

The hypothesis is that when interstellar grains accrete onto planetesimals and small bodies, they preserve their composition, at least in part.

It is also known, however, that comets are continuously exposed to energetic processes such as cosmic ion and UV photon irradiation, which are able to alter the original cometary material and induce chemical and physical changes, including the formation of molecules that were not originally present. As an example applying experimental results to a specific molecule, it has been suggested that methyl formate is formed in comets after ion bombardment of methanol-bearing ices. It has been evaluated that such a process can account for about 12% of the methyl formate observed in comet Hale-Bopp (Modica et al. 2012). The chemical changes studied in the laboratory have also been used to predict the development of a refractory organic crust that inhibits a direct exposure of ices at the surface (Strazzulla et al. 1991), as presently observed for comet 67P/Churyumov-Gerasimenko by the VIRTIS instrument on the Rosetta spacecraft (Capaccioni et al. 2015). At deeper layers, until about a depth of 5 meters, the nucleus is depleted in volatiles and would have a considerable fraction of organic molecules formed because of irradiation along with unrecombined radicals (Strazzulla & Johnson 1991). Near the surface the dose deposited by cosmic ions is high (hundreds of eV/16u) and decreases with the depth. Doses as low as a few eV/16u are accumulated at depth of the order of tens of meters. In addition to the external flux of cosmic ions, the decay of incorporated radioactive elements also produces chemical effects in comets. The radiation from radionuclides consists of the contribution of long-lived (e.g. ^{129}I , ^{247}Cm , ^{244}Pu) and shorted-lived (e.g. ^{10}Be , ^{237}Np , and ^{26}Al) radionuclides. The absorbed dose that has been accumulated throughout the nucleus over the comet lifetime (4.6×10^9 years) has been estimated to be about 2.3 eV/16u, of which about 0.5 eV/16u are due to long-living

nuclides and about 1.8 eV/16u to the shorter living ^{26}Al (Draganić and Draganić 1984). In the first meter of depth this dose is much lower than that due to cosmic rays. Nevertheless, it is important for the total amount of ionizing energy accumulated throughout the nucleus over the comet lifetime because its action is not limited to surface layers, but extends along the entire cometary nucleus that is uniformly irradiated. As demonstrated in this chapter and in the literature quoted in Sect. , formamide and HNCO are formed by energetic processing of frozen mixtures containing simple H-, C-, N-, and O-bearing molecules.

Table 4.3: Abundances (with respect to water) of relevant molecules measured for the three comets where HNCO and formamide have been observed. The ratios of HNCO and formamide with respect to nitrogen atoms in N₂ or in NH₃ are also reported. References: (1) Bockelée-Morvan et al. (2000); Biver et al. (2014). (2) estimated from Rubin et al. (2015) (3) Bockelée-Morvan et al. (2000); Paganini et al. (2014a) (4) Bockelée-Morvan et al. (2000); Biver et al. (2014) (5) Biver et al. (2014); Paganini et al. (2014a); Paganini et al. (2014b)

Species	Abundance (% of H ₂ O)			Ref.
	Hale-Bopp	Lemmon	Lovejoy	
CO	2.3	4.0	7.2	(1)
N ₂	0.013	0.023	0.041	(2)
HNCO	0.1	0.025	0.021	(3)
NH ₂ CHO	0.02	0.06	0.021	(4)
NH ₃	1-1.8	≤ 0.63	≤ 1.86	
HNCO/N in N ₂	3.85	0.55	0.26	
NH ₂ CHO/N in N ₂	0.77	1.3	0.26	
HNCO/NH ₃	0.06-0.1	≥ 0.04	≥ 0.01	
NH ₂ CHO/NH ₃	0.01-0.02	≥ 0.01	≥ 0.01	

Therefore it makes sense to investigate whether energetic processing of comets can contribute to the formation of the two N-bearing molecules. In comet Hale-Bopp ammonia has been detected in the coma with an abundance of about 1–1.8% with respect to water (Bird et al. 1997; Crovisier and Bockelée-Morvan 1999). Molecular nitrogen is thought to have been the most abundant form of nitrogen in the proto-solar nebula, although it has only recently been observed in situ in comet 67P/Churyumov-Gerasimenko by the Rosetta Orbiter Spectrometer for Ion and Neutral Analysis mass spectrometer onboard the Rosetta spacecraft (Rubin et al. 2015). The molecular number ratio for N_2/CO of $5.70 \pm 0.66 \times 10^{-3}$ implies a depletion of 25.4 ± 8.9 with respect to the available pre-solar nitrogen. In Table 3 we report the abundances of relevant molecules measured for the only three comets where HNCO and formamide have been observed. We have scaled the abundance of N_2 from that of CO assuming the same ratio as measured for comet 67P/Churyumov-Gerasimenko by Rubin et al. (2015). In Table 3 we also report the ratios of HNCO and formamide with respect to nitrogen atoms in N_2 or in NH_3 . This number can be compared with the results presented in Fig. 4.3, with the caution that in the figure the ratio refers to the nitrogen originally present, while from the astronomical observations it is not possible to determine to which extent the observed molecular abundances are pristine or modified by post-formation processing. With this in mind, we see, however, that in comets HNCO cannot be produced by energetic processing of the studied ices in significant amount. In addition, assuming that all of the pre-solar molecular nitrogen was incorporated into comets, the ratios in the table would be divided by a factor 25, which is still higher than measured in the laboratory. We then conclude that either HNCO is incorporated in the comet directly from the gas in the solar nebula or it has to be produced by processing of ice mixtures different from those considered here. The case

of formamide is different: assuming, conservatively, that the observed ammonia is the pristine one, the results shown in Fig. 4.3 indicate that the observed ratio of formamide/ammonia can be obtained after a dose of about a few eV/16u.

4.3.3 Astrobiological relevance of formamide

Among the different theories for the prebiotic chemistry, the extraterrestrial synthesis of organic compounds and their delivery to the Earth's surface is seen as one of more probable scenarios that occurred on the early Earth and that was responsible for the origin of life. A considerable amount of extraterrestrial material was and is continuously delivered to Earth (between 10^7 and 10^9 kg yr⁻¹ of organics in the first billion years; Chyba and Sagan 1992).

Formamide is the simplest naturally occurring amide. This compound contains in its structure all the elements that are required for the synthesis of biomolecules, specifically, hydrogen, carbon, oxygen, and nitrogen, with the only exception of phosphorus and sulphur. Although formamide is easily formed by the reaction of hydrogen cyanide with water, we here suggest that it can be directly delivered to Earth by comets and cometary debris. It is a polar solvent like water with the characteristic that many species that are unstable in water with respect to hydrolysis are spontaneously synthesized in formamide. This includes nucleosides (from ribose borates and nucleobases), peptides (from amino acids), and even oligoribonucleotides. Thus its presence on the early Earth could have favoured a further chemical evolution.

An intense experimental analysis has in fact demonstrated that formamide is a very active molecule in the synthesis of fundamental compounds of biochemistry, such as nucleobases and carboxylic acids.

Thus, formamide chemistry is an extremely promising pathway to provide a plausible unitary frame for the origin of the genetic polymers and metabolic cycles in the extant forms of life (Saladino et al. 2012).

Chapter 5

Infrared study on the thermal evolution of solid state formamide

Based on Urso, R. G., Scirè, C., Baratta, G. A., Brucato, J. R., Compagnini, G., Kaňuchová,
Z., Palumbo, M. E. & Strazzulla, G. 2017, *Physical Chemistry Chemical Physics*, 19, 21759

5.1 From the solid-phase synthesis to the gas-phase detection

Formamide, also known as methanimide (NH_2CHO), is a molecule that belongs to the amide family and includes a peptide bond. It has been shown that it can act as a precursor in the synthesis of many interesting compounds from a biological point of view, such as amino and nucleic acids (Saladino et al. 2005, 2009, 2012; Pino et al. 2015), making it one of the possible players in pre-biotic chemistry. Formamide has been detected in several astrophysical environments. In particular, it has been observed in the gas phase in some star-forming regions in space (e.g., Rubin et al. 1971; Mendoza et al. 2014; López-Sepulcre et al. 2015). In these regions gas and dust start to accumulate toward the centre of a cold cloud, so that a star eventually forms. About 200 molecules¹ have been detected in the gas phase toward these regions by means of ground based radio telescopes. Using both ground- and space-based infrared telescopes, a few molecules have been detected also in the solid phase, where they are found on the surface of silicates or carbonaceous dust grains, forming the so-called *icy grain mantles*.

During the star formation process, the chemical complexity of icy grain mantles increases because of their interaction with other gas-phase species (mainly atomic hydrogen), UV-photons and cosmic rays. In particular, cosmic rays are highly energetic charged particles that bombard the icy mantles and release a fraction of their energy to the target, modifying their chemical composition (Greenberg 1973; Rothard et al. 2017). During the latter stages of stellar formation, a protoplanetary

¹<https://www.astro.uni-koeln.de/cdms/molecules>

disk forms and temperature increases in the region closer to the star. Because of the heating, molecules that were frozen on the icy grain mantles sublime in the gas-phase, where they can further react and form new and more complex species. Only dust grains that are in the outer region of the protoplanetary disk can preserve at least partially their icy mantles. Moreover, they can also be enriched of newly formed species coming from the gas-phase. Thanks to the comparison between the spectra acquired by means of infrared telescopes toward several sources in space and the data coming from laboratory experiments in which icy grain mantles analogues are synthesized, it has been possible to determine their physical structure (Dartois & d’Hendecourt 2001; Dartois et al. 2003) and chemical composition. In particular, it has been possible to detect water and carbon monoxide as the main constituents of icy mantles, together with carbon dioxide, methane, methanol and ammonia (Boogert et al. 1997; Gibb et al. 2004; Dartois 2005; Öberg et al. 2011; Boogert et al. 2015). Other species, such as formaldehyde, sulfur dioxide and carbonyl sulfide have been likely detected (Schutte et al. 1994; Boogert et al. 1997; Palumbo et al. 1997). Furthermore, Schutte et al. (1999) and Raunier et al. (2004) reported a tentative detection of solid formamide in the line-of-sight of young stellar objects observed with the Infrared Space Observatory-Short Wavelength Spectrometer (ISO-SWS). It is generally accepted that dust grains coagulate into larger objects named planetesimals that are the building blocks of future planets, comets and asteroids (Caselli & Ceccarelli 2012). In this scenario, it is interesting to note the detection of formamide in the coma of comets C/1995 O1 Hale-Bopp (Bockelée-Morvan et al. 2000), C/2012 F6 Lemmon and C/2013 R1 Lovejoy (Biver et al. 2014).

To date, there is an open debate about formamide synthesis in space, in particular if it occurs directly in the gas phase in star-forming regions, where it has been firmly detected, or in the solid phase, i.e.,

on the icy mantles of dust grains or on the surface of comets. Recent thermochemical and kinetic computations have shown that formamide can be produced at low temperature in the gas-phase by the reaction of formaldehyde (H_2CO) with NH_2 (Barone et al. 2015; Vazart et al. 2016). On the other hand, laboratory experiments have shown that formamide is produced after the energetic processing, i.e., ion and electron bombardment and UV-photolysis that simulate the effects of cosmic rays and UV-photons in space, of mixtures that are thought to be representative of icy mantles and cometary surfaces (e.g., Gerakines et al. 2004; Jones et al. 2011; Henderson & Gudipati 2015; Kaňuchová et al. 2016; Fedoseev et al. 2016).

In Chapter IV we have shown that the irradiation with protons or helium ions of different solid mixtures containing water, methane, ammonia or nitrogen at low temperatures drives the synthesis of formamide together with isocyanic acid (HNCO). We compared the $\text{HNCO}/\text{NH}_2\text{CHO}$ molecular number ratio obtained from laboratory data with that obtained from observations. The results showed that in most cases the ratio obtained in laboratory experiments is lower than the ratio observed in star-forming regions, suggesting that the abundance of formamide in star-forming regions can be ascribed to energetic processing of icy mantles while other processes, such as gas-phase and grain surface reactions, have to be taken into account to explain the observed abundances of isocyanic acid. Also, concerning comets, we showed that energetic processing can explain the observed amount of formamide, while HNCO cannot be produced in significant amounts.

Once it has been proved that energetic processing is efficient in the formation of NH_2CHO , it is important to understand how this molecule is injected into the gas phase. Dawley et al. (2014) have reported on the thermal desorption of pure formamide. In their experiments, they have deposited the amide on porous silicon oxide nanoparticles at 70 K

and they have followed by means of infrared spectroscopy the sample warm up until its complete desorption. They have observed that formamide crystallize at about 165 K and it starts to desorb from the SiO₂ substrate at 210 K. The complete desorption requires about 380 K. They have also investigated the desorption of a H₂O:NH₂CHO=2:1 mixture. In this experiment water sublimates at about 160 K, leaving formamide on the substrate that then follows the same behaviour shown when deposited in pure form.

Several laboratory experiments have been carried out to study the crystallization and desorption of other astrophysical relevant molecules. As an example, amorphous solid water (ASW) crystallizes to form cubic ice (I_c) above 125 K in laboratory time scales (e.g., Baragiola 2003). Schmitt et al. (1989) studied the profile of the OH stretching mode band of water ice (at about 3300 cm⁻¹) and they derived the activation law that links the crystallization time (t_c) with temperature (T):

$t_c = A \cdot \exp(-E_A/kT)$, where A is a constant = 9.54×10^{-14} s, $-E_A/k$ is the activation energy=5370 K. Also Baragiola (2003) reported that in water ice the amorphous to crystalline transition does not occur at a particular temperature, but over a temperature range as a function of the heating rate. The lower is the heating rate, the lower will be the crystallization temperature. Also the desorption temperature depends on the heating rate.

To the best of our knowledge, there is a lack of data about the thermal desorption of formamide when in mixture with other astrophysical relevant molecules. In this chapter, we report the data we collected during experiments about the sublimation of solid films containing pure formamide and formamide in mixture with water and carbon monoxide, the most abundant solid phase molecules in space, in order to simulate its desorption from the icy grain mantles and cometary surfaces. We also show experimental results about the ion bombardment with 200

keV H^+ of a mixture containing nitrogen, methane and water to discuss about the desorption of formamide when synthesised after energetic processing at low temperature. The experiments allowed us to determine the crystallization and desorption temperature of formamide when pure and in mixtures and to apply these results to an astrophysical context. Note that in this work we did not perform a programmed warm up, as in typical temperature programmed desorption (TPD) experiments. We searched for the temperature at which the formamide crystallization and desorption take place by monitoring any variation in its infrared spectra.

5.2 Experimental methods

The experiments here shown have been performed in the Laboratory for Experimental Astrophysics at INAF-Osservatorio Astrofisico di Catania (Italy). We carried out two different sets of experiments, one to investigate the thermal evolution of formamide when pure and in mixture with water and carbon monoxide, and one to study its desorption when synthesised after irradiation of the sample with energetic ions (200 keV H^+). All the experiments have been performed in an ultra-high vacuum (UHV) chamber ($P \leq 10^{-9}$ mbar) shown in Fig.5.1. Inside the UHV chamber a KBr substrate is placed in thermal contact with the final tail of a closed-cycle helium Cryocooler (CTI) such that its temperature can be varied between 17 and 300 K. In the first set of experiments, to avoid any interaction between gases before deposition, we introduced the species in two separate chambers at room temperature and $P < 10^{-7}$ mbar. A chamber was dedicated to both water or CO, with an inlet in the UHV chamber (Inlet A in Fig.5.1), while in a second chamber we introduced formamide only, that was then admitted in the UHV chamber by an inlet mounted on its lateral wall (Inlet B in Fig.5.1) simultaneously with water or CO. This set-up allowed us to obtain pure NH_2CHO , $\text{NH}_2\text{CHO}:\text{H}_2\text{O}$ and $\text{NH}_2\text{CHO}:\text{CO}$ mixtures.

In the second set of experiments, a $\text{N}_2:\text{CH}_4:\text{H}_2\text{O}$ mixture has been prepared in a vacuum chamber ($P < 10^{-7}$ mbar) and introduced in the UHV chamber by the Inlet A in Fig.5.1. Once inside the UHV chamber, molecular species to be investigated condense on the cold substrate forming a solid film. The $\text{N}_2:\text{CH}_4:\text{H}_2\text{O}$ film thickness has been measured during the deposition following the procedure described in Fulvio et al. (2009) and Urso et al. (2016). An He-Ne laser beam ($\lambda = 543.5$ nm)

is directed toward the sample and reflected at near normal incidence (2.9°) both by the vacuum-sample and sample-substrate interfaces. The reflected beam is detected by an external silicon diode detector. There is a difference in the optical path between the reflected components of the laser beam that varies with the thickness of the film, so that an interference curve is produced. It is possible to follow the accretion of the film by looking at the interference curve (intensity vs. time) of the reflected laser beam (e.g., Urso et al. 2016).

After deposition, the $\text{N}_2:\text{CH}_4:\text{H}_2\text{O}=1:1:1$ mixture was irradiated with 200 keV H^+ . The vacuum chamber is connected to a 200 kV Danfysik ion implanter. The ion beam is electrostatically swept to ensure a uniform coverage on the target. In order to prevent a macroscopic heating of the sample we used an ion current density between 100 nA cm^{-2} and a few $\mu\text{A cm}^{-2}$. The ion fluence (ions cm^{-2}) was measured by integrating the ion current monitored during irradiation. We calculated the energy deposited by incoming ions to the sample (dose) by multiplying the fluence and stopping power (i.e., the amount of energy deposited per unit path length; $\text{eV cm}^2/\text{molecule}$) given by the SRIM code (Ziegler et al. 2008). The dose is given in $\text{eV}/16\text{u}$, which is a convenient way to characterize chemical changes and also to allow a comparison with other irradiation experiments (Strazzulla et al. 1991).

All the samples were analyzed using infrared spectroscopy. Infrared transmission spectra were acquired at oblique incidence (45°) by a Fourier transform infrared (FTIR) spectrometer (Bruker Vertex 70) with a resolution of 1 cm^{-1} and sampling of 0.25 cm^{-1} . A rotatable polarizer placed along the path of the IR beam allows us to take spectra both with the electric vector parallel (P-polarized) and perpendicular (S-polarized) to the plane of incidence of the infrared beam. Except from Fig.5.3, in this work we will show the spectra acquired in P-polarization because of a better signal-to-noise ratio. In fact, the

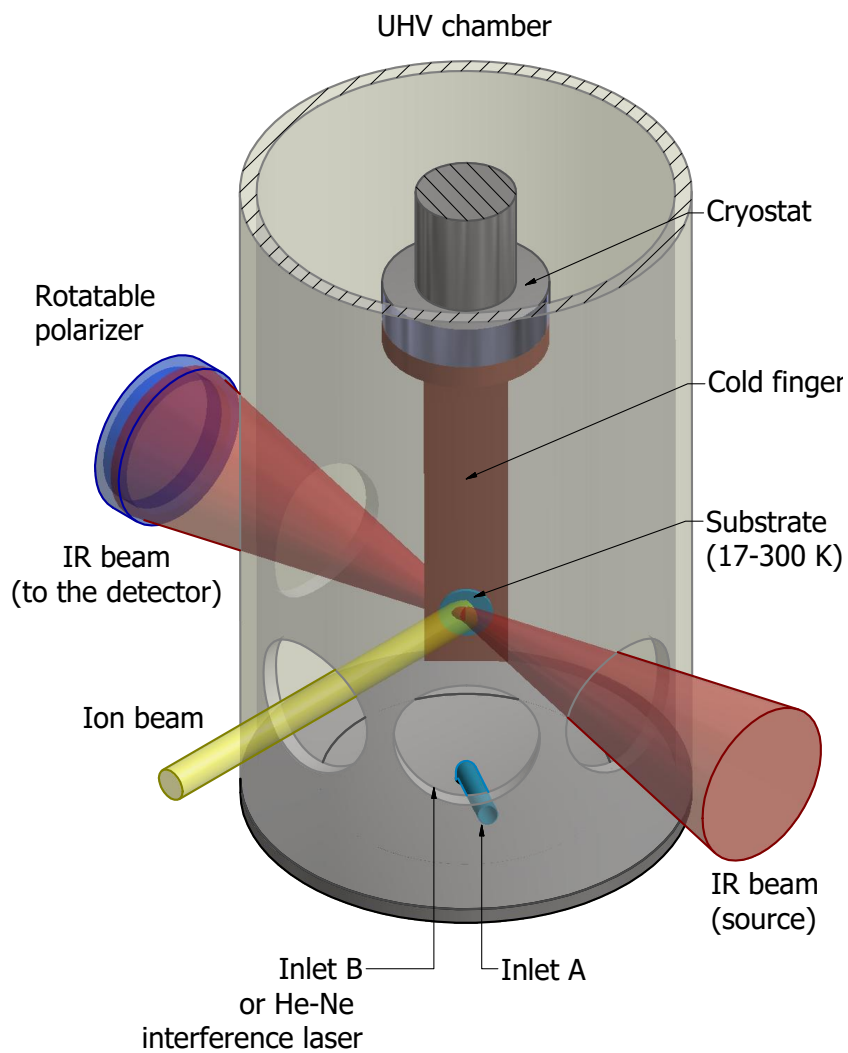


Figure 5.1: Schematic view of the UHV chamber and the geometry used to irradiate the sample and to acquire infrared spectra.

transmitted signal in P-polarization is higher than the transmitted signal in S-polarization(Bohren & Huffman 1983).

We performed several steps of warm up for each sample to determine the formamide thermal evolution and desorption temperature. We acquired transmission infrared spectra of the samples as deposited and after each step of irradiation and warm up. Also, during the experiments we set the spectrometer in a monitoring configuration that allows to check the infrared spectrum of the sample by means of fast and continuous acquisitions. In this way it was possible to stop the warm up and acquire a spectrum if some change would appear. See Palumbo et al. (2006) and Kaňuchová et al. (2016) for further details about the experimental procedure.

5.3 Results

Three experiments have been carried out by depositing pure NH_2CHO and mixtures $\text{NH}_2\text{CHO}:\text{H}_2\text{O}=1:14$ and $\text{NH}_2\text{CHO}:\text{CO}=1:40$ at 17 K and warming up the samples until their complete desorption from the substrate. The mixtures we deposited contain formamide in the highest dilution we have been able to obtain in our experimental conditions, in order to be as close as possible to the astrophysical context where this molecule is expected to be highly diluted. Furthermore, we performed an irradiation experiment in which we deposited a $\text{N}_2:\text{CH}_4:\text{H}_2\text{O}=1:1:1$ mixture at 17 K that has been bombarded with 200 keV H^+ to simulate the effects of cosmic-rays on icy grain mantles and comets. After irradiation we warmed up the sample to study the desorption of the synthesized formamide.

In Fig.5.2 we show the IR spectra of pure formamide, formamide in mixture with water and formamide in mixture with carbon monoxide at 17 K (left panel) and at 170 K (right panel). After the deposition, we started the desorption experiment in a step-by-step procedure: we increased the cryostat temperature up to a certain value, then we waited for the temperature stabilization before spectra acquisitions. For clarity, we do not show the region without vibrational bands attributed to formamide, i.e. between 2700 and 1840 cm^{-1} .

5.3.1 Pure formamide

In Fig.5.2 A we show the IR spectrum of pure formamide deposited at 17 K. All the known vibrational features are labelled. Spectra have been acquired at 17, 30, 35, 140, 160 and 170 K. We chose these temperatures because formamide is stable until about 160 K, when a structural

change starts to take place, as reported by Dawley et al. (2014). In our experiments no changes appeared in the infrared spectra until the sample reached 170 K. At this temperature we observed a remarkable difference in the profile of the infrared bands, as it is possible to see in Fig.5.2 B. This difference is due to the structural change of the sample. The main vibrational features appear sharper and narrower if compared to those observed in Fig. 5.2 A. As an example, the C=O stretching mode band centred at about 1690 cm^{-1} shows a FWHM of about 64 cm^{-1} at 17 K, while it decreases to about 25 cm^{-1} at 170 K. Other remarkable differences are the appearance of at least four components in the feature centred between 3040 and 3460 cm^{-1} , the sharpening and increasing intensity of the C-H stretching mode band centred at 2884 cm^{-1} and the higher intensity of the C-N stretching mode band at 1328 cm^{-1} . These band changes are attributed to a transition between a disordered phase to a much ordered one, i.e., an amorphous to crystalline transition. A similar behaviour has been reported for many molecules, and some examples are reported by Hudgins et al. (1993), Palumbo et al. (1999), Modica & Palumbo (2010), Moore et al. (2010) and Abdulgalil et al. (2013).

After the sample structural change, the acquired spectra did not show remarkable differences at higher temperatures and formamide started to sublime from the substrate at about 220 K.

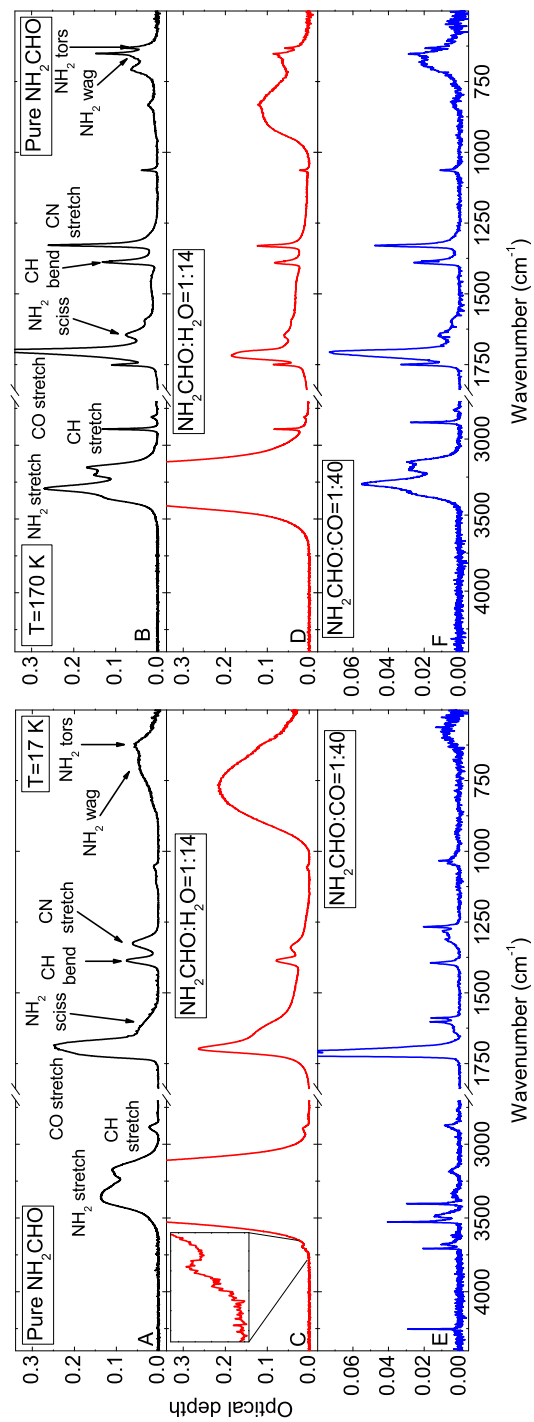


Figure 5.2: Infrared spectra in optical depth scale of pure formamide (black line, A and B) and formamide in mixture with water (red line, C and D) and carbon monoxide (blue line, E and F) acquired at 17 K (left panel) and at 170 K (right panel).

LO-TO splitting in pure formamide

It is well known that band profiles of solid phase molecules in transmittance spectra at oblique incidence could show both the transverse optical (TO) and longitudinal optical (LO) modes referred to as the LO-TO splitting (e.g., Baratta & Palumbo 1998; Baratta et al. 2000; Palumbo et al. 2006). As discussed by Palumbo et al. (2006) the occurrence of the splitting and the wavenumber position of the LO and TO modes depend on the dielectric function of the sample ($\varepsilon = \varepsilon' + i\varepsilon''$). In particular the LO mode is present if the real part of the dielectric function (ε') across a given absorption band becomes negative and occurs at the position where ε' crosses the zero value at higher wavenumbers after the minimum. Spectra taken at normal incidence only show the TO mode because no longitudinal vibration can be excited. When a polarizer is used, spectra taken in S-polarization are equivalent to spectra taken at normal incidence.

Among the bands present in the transmittance spectrum of pure formamide, only the C=O stretching mode at about 1700 cm^{-1} shows the LO-TO splitting. In Fig. 5.3 we present the spectra acquired in P-polarization and S-polarization in the C=O stretching mode band region of pure formamide as deposited at 17 K (panel A), and after warm up to 170 K, when the sample is crystalline (panel B). Vertical dashed lines correspond to the TO mode positions, while dotted lines indicate the LO mode positions. The spectrum acquired at 17 K in S-polarization (red line in panel A) shows a band whose peak is found at 1684 cm^{-1} . At the same temperature, the spectrum acquired in P-polarization (black line in panel A) shows a broader band that results from the superposition of both the TO mode, whose peak is centred at 1684 cm^{-1} , and the LO mode, peaked at about 1720 cm^{-1} . Warm-

ing up the sample, formamide undergoes crystallization and the C=O stretching mode band profile change significantly. Red line in panel B shows the spectrum acquired at 170 K in S-polarization. An intense band is centred at 1700 cm^{-1} , while a weak feature is observed at about 1748 cm^{-1} , in agreement with the C=O stretching mode band positions in solid formamide at 165 K reported by Dawley et al. (2014) (see Table 1 in their paper). At the same temperature, when the spectrum is acquired in P-polarization (black line), we observed that the band on the higher wavenumber side is centred at 1751 cm^{-1} and is due to the superposition of two bands peaked at 1748 and 1751 cm^{-1} , respectively. This latter feature is assigned to the LO mode of the intense 1700 cm^{-1} band. Also, at the same temperature, the NH_2 bending feature at about 1645 cm^{-1} appears (Dawley et al. 2014).

5.3.2 Formamide in water

In Fig.5.2 C and D we show the spectra of a mixture $\text{NH}_2\text{CHO}:\text{H}_2\text{O}=1:14$ deposited at 17 K and warmed up to 170 K, respectively. It should be noticed that some characteristic vibrational mode bands attributed to water overlap with those due to formamide, as in the case of the O-H stretching mode and the NH_2 stretching mode bands at about 3300 cm^{-1} , the bending mode of water and the CO stretching mode bands at about 1660 cm^{-1} , and finally the libration mode of water centred at about 770 cm^{-1} and the NH_2 wagging and torsion modes bands.

The spectrum gives useful information about the structure of the sample. In particular, the O-H dangling bonds feature centred at about 3700 cm^{-1} present in the spectrum acquired at 17 K (see the inset in Fig.5.2 C) points out that the sample is a porous amorphous film. Two different components are distinguishable, one centred at 3694 cm^{-1} and one at 3716 cm^{-1} attributed to three- and two-coordinate water molecules, respectively (Palumbo 2006). These features are not present

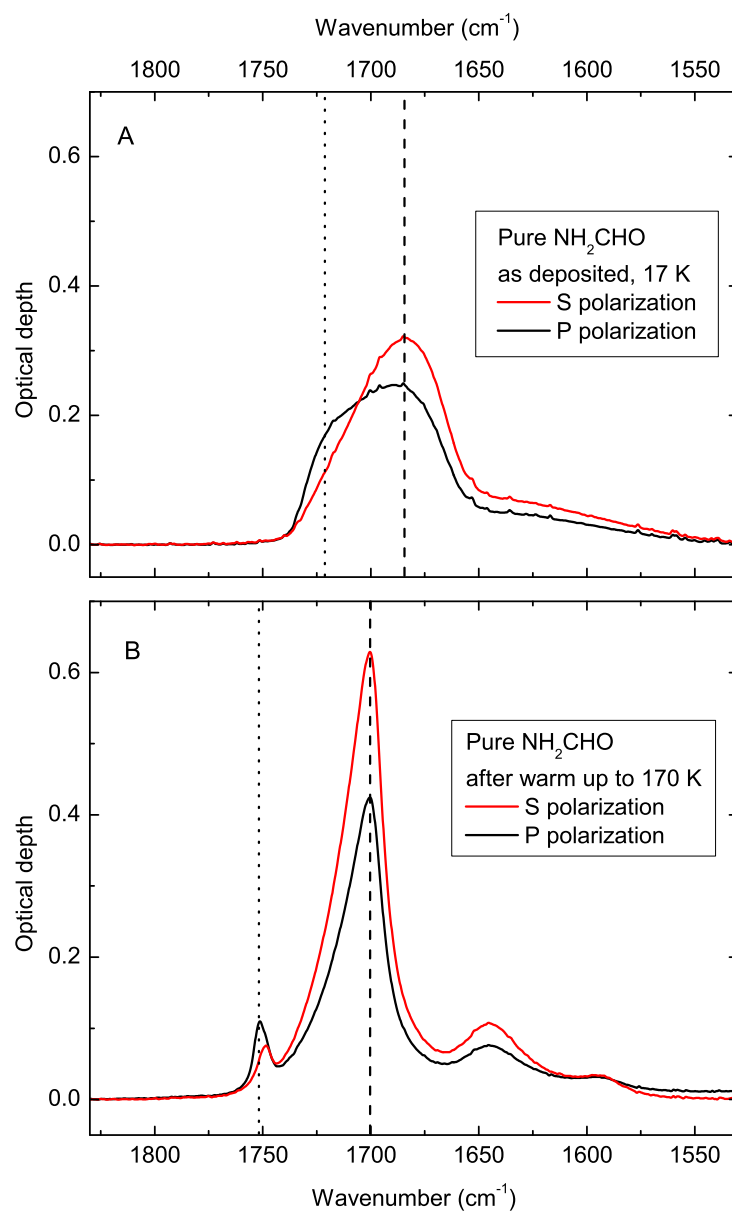


Figure 5.3: Infrared spectra in optical depth scale of pure formamide as deposited at 17 K (panel A) and after warm up to 170 K (panel B). Red solid lines: spectra acquired in S-polarization; black solid lines: spectra acquired in P-polarization. Vertical dashed lines: TO modes; vertical dotted lines: LO modes

in the spectrum acquired at 140 K because of the compaction and the crystallization of the sample (Bossa et al. 2012).

In our experimental conditions pure water sublimates at about 160 K, but in this experiment its vibrational features were still visible in the spectrum we acquired at 170 K (Fig.5.2 panel D), even if with lower intensity. An explanation is that a fraction of the deposited water molecules interact via H-bonds with formamide, that is the major component of the sample at this temperature. As a result, a higher temperature is required to complete the water sublimation, that occurs at 180 K. Excluding the vibrational features of water, the spectrum in Fig.5.4 D is superimposable to the one of pure crystalline formamide at 170 K shown in the same figure (panel B). Finally, the experiment has been completed with the desorption of formamide at about 220 K.

5.3.3 Formamide in a CO matrix

In Fig.5.2 E we show the spectrum of a mixture $\text{NH}_2\text{CHO}:\text{CO}=1:40$ deposited at 17 K. Here the attribution of the vibrational bands is not straightforward as in the cases we have shown previously. The same spectrum is better shown in Fig.5.4, where most of the vibrational bands have been assigned. The spectrum include also the frequency range where the vibrations due to carbon monoxide and its isotopologues are found. For more details about CO infrared vibration modes see Baratta & Palumbo (1998) and Urso et al. (2016). In our sample, formamide is highly diluted in carbon monoxide. The narrow vibrational bands that appear in the spectra are due to the presence of monomers and dimers, i.e., one isolated molecule or two molecules of formamide interacting with each other, respectively, and surrounded by CO molecules. This effect has been observed also for other mixtures (e.g., Ehrenfreund et al. 1996). The labels in the figure have been attributed following the works by Räsänen (1983a,b), Torrie & Brown (1994), Lundell et al. (1998),

Mardyukov et al. (2007) and Sivaraman et al. (2013). The vibrational bands assigned to water monomers and dimers (between 3600 and 3700 cm^{-1} and at about 1600 cm^{-1}) and CO_2 (at 2347 cm^{-1}) are due to contaminants.

In our experimental conditions, pure carbon monoxide desorbs at about 32 K. In the warm up experiment of the $\text{NH}_2\text{CHO}:\text{CO}=1:40$ mixture, the 2140 cm^{-1} CO stretching mode band completely disappeared at a temperature higher than 100 K, because some CO remains trapped inside the layer of formamide that is left on the substrate. At higher temperature only formamide remains, as shown in the spectrum acquired at 170 K (Fig. 5.2 F). Within experimental uncertainties, this spectrum is identical to the one shown in the panel B of the same figure.

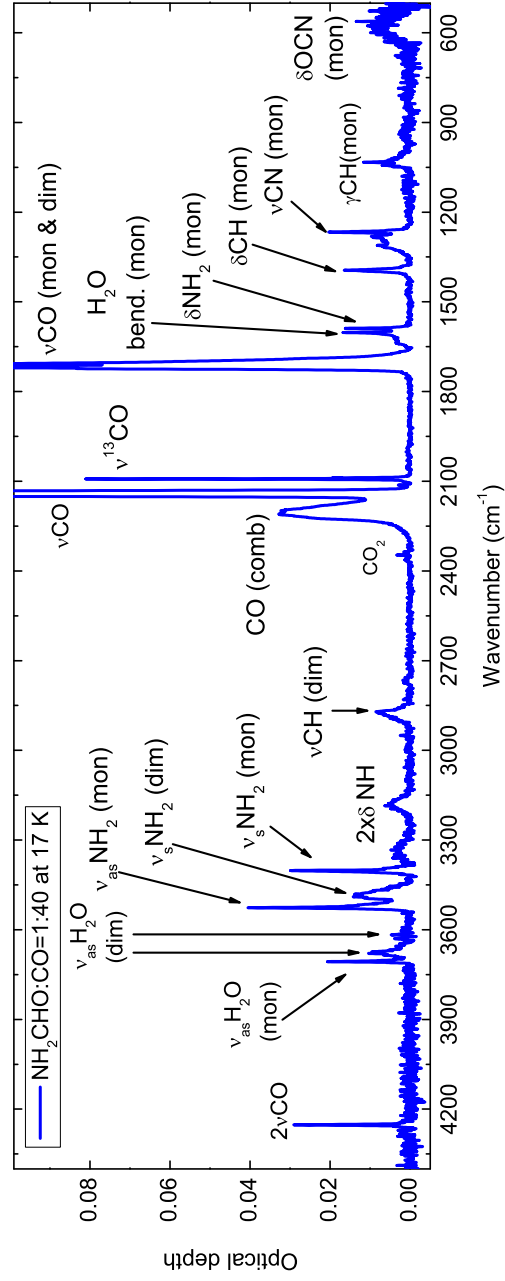


Figure 5.4: Infrared spectrum in optical depth scale of a NH₂CHO:CO=1:40 mixture. Labels indicate the known vibrational bands attributed to formamide, carbon monoxide and contaminants water and carbon dioxide. (mon): monomers; (dim): dimers.

5.3.4 Irradiation of a $\text{N}_2:\text{CH}_4:\text{H}_2\text{O}=1:1:1$ mixture

In Chapter IV we reported that the irradiation of a frozen mixture containing nitrogen, methane, and water with 30 keV He^+ drives to the formation of formamide. To extend the previous work, in this paragraph we show the results obtained after the irradiation of the same mixture with 200 keV H^+ up to a final dose of 122 eV/16u and its warm up to determine the desorption temperature of the newly synthesised formamide.

In Fig. 5.5 we show a comparison between the infrared spectra of pure formamide (panel A), formamide in mixture with water (panel B) and the $\text{N}_2:\text{CH}_4:\text{H}_2\text{O}$ mixture (panel C) as deposited (magenta dashed line) and after the H^+ bombardment (green line) at 17 K. The spectrum acquired after the irradiation exhibits not only the vibrational bands related to the deposited species, but also those due to the presence of newly formed molecules. The chemistry induced by ion bombardment is well studied for various mixtures (e.g., Trottier & Brooks 2004; Seperuelo-Duarte et al. 2010; Islam et al. 2014). Rothard et al. (2017) described the effects occurring when energetic particles interact with matter along the so-called ion track, i.e. the projectile's trajectory. The changes observed in the samples are due to transfer of energy and momentum from the projectile to the target. Both elastic and inelastic collisions take place. The overall process happens within about 10^{-14} s. The action of the high energy ions (200 keV H^+ in the present experimental case) on the sample causes the breaking of about 10^5 molecular bonds (few eV/bond), leading to a chain of recombination reactions. These reactions do not take place in thermodynamic equilibrium (e.g., Woods et al. 2015).

The spectrum in Fig. 5.5 C can be easily compared also to those

reported by Palumbo et al. (2004) for the same mixture after irradiation with 30 keV He⁺ ions. Several bands fall at frequencies that have been associated to the vibrational modes of formamide by Dawley et al. (2014) (see Table 1 in their paper). The band positions are pointed out by dashed vertical lines in Fig. 5.6. The spectrum acquired at the end of the irradiation (a) is compared to those acquired during the subsequent warm up of the sample. Because of the heating, volatile species leave the substrate determining the changes observed in the spectra during the experiment. On the other hand, non-volatile species remain on the substrate as a refractory residue (e.g., Ferini et al. 2004; Palumbo et al. 2004; Baratta et al. 2015).

As discussed in the previous sections, formamide desorbs at about 220 K, so its contribution should not appear in the infrared spectra acquired at higher temperature. However, the bands we used for its identification are still present in our sample even in the spectrum acquired after we kept the sample under vacuum at 296 K for 24 hours.

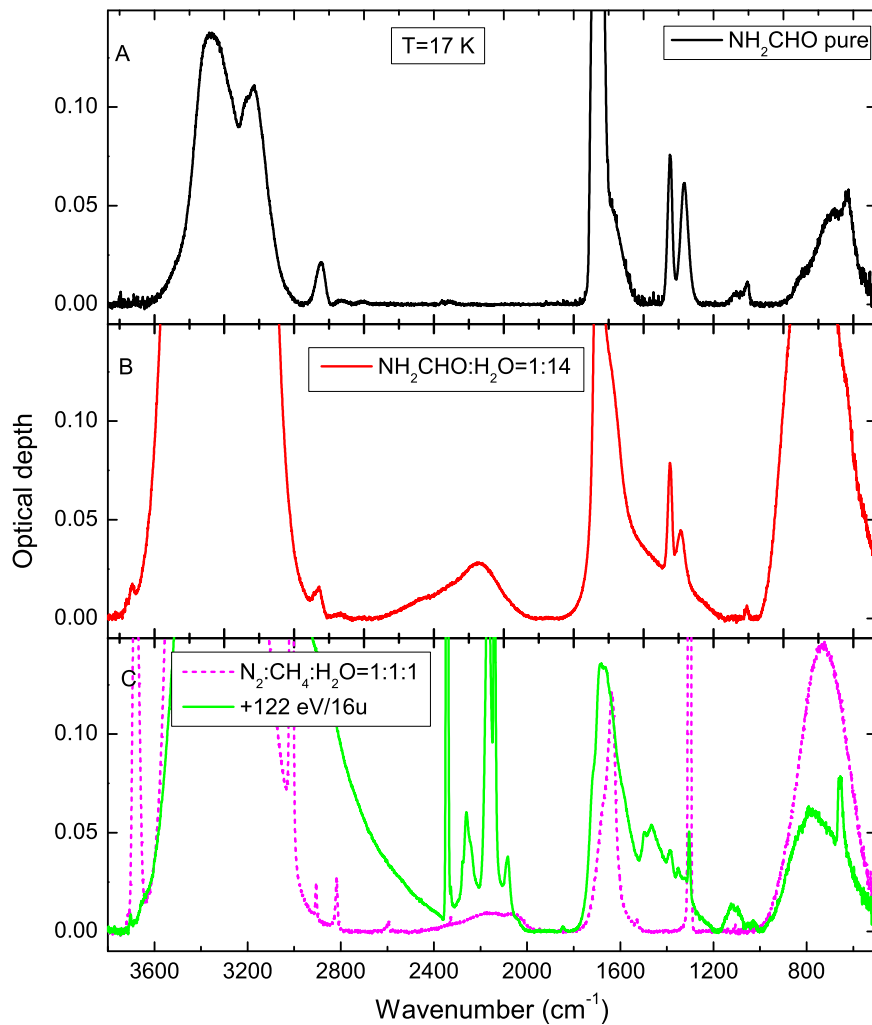


Figure 5.5: Comparison between spectra acquired at 17 K for pure formamide (panel A), formamide in water (panel B) and a mixture containing nitrogen, water and methane (panel C) as deposited (magenta dashed line) and after irradiation with 200 keV H⁺ up to 122 eV/16 u (green line).

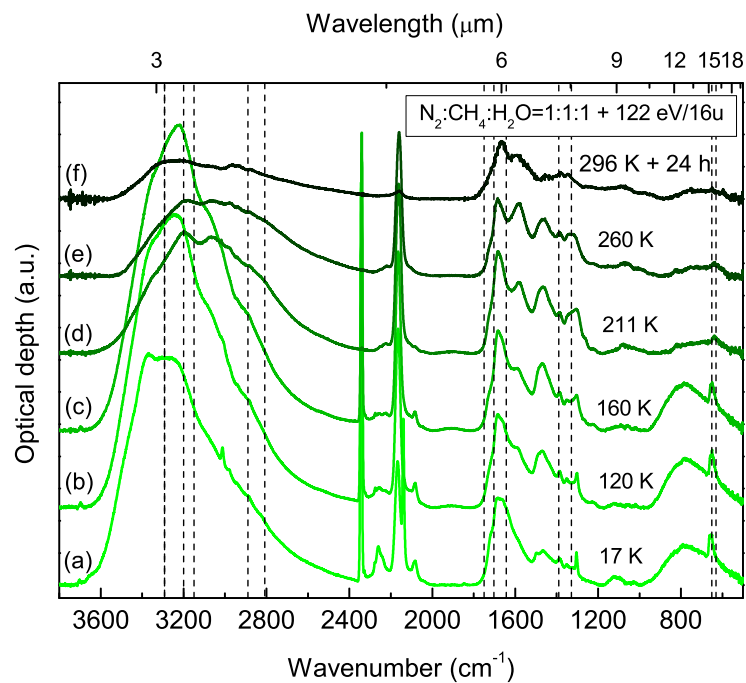


Figure 5.6: IR spectra of a $N_2:CH_4:H_2O=1:1:1$ mixture irradiated with 200 keV H^+ at 17 K up to 122 eV/16u and warmed up to 296 K. All the spectra are shown in optical depth scale and displaced by an arbitrary offset for clarity. Vertical dashed lines represent the vibrational frequencies of pure formamide at 165 K as reported by Dawley et al. (2014)

5.4 Discussion

According to our experimental results, pure formamide crystallize at 170 K and desorbs from the substrate at about 220 K. Also, infrared spectra acquired in both P- and S- polarization allowed us to detect the LO-TO splitting in the CO stretching feature in formamide. We have not observed remarkable differences in the crystallization temperature of formamide when in mixture with water, the latter sublimating at 180 K and leaving pure crystalline formamide on the substrate up to about 220 K. When formamide has been diluted in CO, its infrared spectral features allowed us to determine the presence of monomers and dimers in the sample. CO started to desorb at about 40 K, and completely left the sample at a temperature higher than 100 K. Because of the high dilution of formamide, we expected that during the sublimation of CO, it could drag also formamide into the gas phase. However, we observed that formamide remained on the substrate up to 220 K. Other examples concerning molecules diluted in a volatile matrix which do not desorb when the matrix sublimates have been reported in literature. Brucato et al. (1997) showed that carbonic acid is produced after the irradiation of mixtures containing water and carbon dioxide with 1.5-3 keV H or He ions. Carbonic acid remains on the substrate as a residual film up to 247 K, while volatile species sublime at lower temperatures. Burke et al. (2015) reported about experiments in which methyl formate, acetic acid and glycolaldehyde were mixed or adsorbed on water ice at 20 K and warmed up until the complete sublimation of the sample. In their Time Programmed Desorption (TPD) experiments, they observed that methyl formate desorbs at about 145 K, when it is released by the pores in the water ice and glycolaldehyde co-

desorbs with water at about 160 K. For the acetic acid:water mixture they observed that the acid can remain on the substrate up to about 175 K, after water desorption.

As reported in the previous section, the changes observed in the spectra of formamide acquired at 170 K have been attributed to the crystallization of the samples. In particular, the NH_2 stretching bands that appear as two distinct features overlapped at about 3250 cm^{-1} show a splitting in four narrower overlapped bands. This variation is ascribed to dimerization in the unit cell of crystalline formamide. In fact, according to Ladell & Post (1954) and Suhai (1996), the molecular arrangement in crystalline formamide consists of cyclic dimers interacting via H bonds, associated to form a puckered structure of sheets. As already reported by Sivaraman et al. (2012, 2013) the warm up determines a reorganization of molecules within the sample. As a consequence, the dimerization progressively takes place approaching the crystallization temperature of formamide.

The irradiation of the $\text{N}_2:\text{CH}_4:\text{H}_2\text{O}$ mixture with 200 keV H^+ allowed us to detect formamide among the synthesised molecules in the sample, confirming the results reported in Chapter IV. During the warm up of the sample, after the volatiles sublimation, the formamide vibrational features were detectable up to 296 K in the residue that has been formed on the substrate. This result strongly suggests that once formamide is formed because energetic processing, it remains trapped inside the refractory organic residue.

It is possible to notice a remarkable difference in the desorption temperature of formamide as pure or in mixtures we reported if compared to the experiments reported by Dawley et al. (2014). In their experiments the complete desorption requires about 380 K. In our opinion, the higher temperature required for the formamide desorption is due to the porous substrate they used to simulate the dust grains, so

that molecules penetrates it during the deposition, remaining trapped through the warm up. In our experiments the deposition is limited on the KBr substrate surface, allowing the desorption at a lower temperature. However, the irradiation experiment and the subsequent heating of the sample have shown that formamide remains trapped in the refractory residue. This effect can be somehow compared to the trapping observed by Dawley et al. (2014) into the porous substrate. Even if the chemical and physical properties of these materials are completely different, both slow down the sublimation because they act as physical barriers, requiring a higher temperature to allow the desorption.

These results can be applied in an astrophysical context. As already said, formamide has been detected in the gas phase in the line-of-sight to star-forming regions and tentatively identified in the solid phase in ISO-SWS infrared spectra of proto-stars, as reported by Schutte et al. (1999) and Raunier et al. (2004). Calculations have suggested that it can be formed directly in the gas phase (Barone et al. 2015; Vazart et al. 2016). Also, energetic processing experiments have shown that its formation is efficient on the icy mantles of dust grains and can explain the observed gas phase abundances if a desorption mechanism is taken into account. The sublimation temperature we determined in laboratory experiments for formamide when pure and in mixture is about 220 K. In the case of its formation after energetic processing of icy mantles analogues, because of its trapping in the residue, the temperature required is higher than 296 K.

It is interesting to couple these data with the work reported by López-Sepulcre et al. (2015). By means of the 30 m IRAM radio telescope they searched for formamide rotational lines toward several star-forming regions within the large program Astrochemical Surveys At IRAM (ASAI). Among them, in proto-stellar objects IRAS 4A, SVS13A, OMC-2 FOR 4, Cep E and I16293 they have been able to

detect formamide and to estimate its column density. For what concern colder sources, i.e., L1544, TMC1, B1, L1527 and L1157-mm, they have detected no formamide. These results suggest that temperatures of a few tens K would determine the non-desorption or a very slow desorption of formamide, explaining its absence in the gas-phase of dark cold clouds, while in hotter sources like pre- and proto-stellar clouds, where the temperature can be higher than 100 K, the sublimation takes place in the time scale of stellar formation, so that it is possible to detect its rotational lines. Also, other desorption mechanisms have to be taken into account if temperature is not high enough to explain formamide sublimation. As an example, cosmic-ray ion erosion of volatiles from dust grains (Bringa & Johnson 2004) and mantle explosions due to impulsive spot heating on grains (Ivlev et al. 2015) could drag formamide into the gas-phase together with other solid phase molecules.

Formamide has been found in the coma of comet C/1995 O1 Hale-Bopp (Bockelèe-Morvan et al. 2000), comet C/2012 F6 Lemmon and comet C/2013 R1 Lovejoy (Biver et al. 2014). These detections are interesting because comets are the result of grain accretion, and our experimental data strengthen the hypothesis that formamide is there since the early stage of the Solar System formation, when these objects formed. Also, the exposure to radioactive element decay and cosmic rays may have contributed to increase its abundance. More recently, new results have been obtained by the European Space Agency Rosetta mission. Rosetta orbited the comet 67P/Churyumov-Gerasimenko and sent the lander Philae on its surface. Both the orbiter and the lander were equipped with several instruments that allowed to investigate the physical and chemical properties of the comet and its coma. Le Roy et al. (2015) reported an inventory of the volatile species detected by the Double Focusing Mass Spectrometer (DFMS) of the ROSINA experiment on board of Rosetta. Among the detected molecules, they have

been able to establish only upper limits for the presence of formamide, found to be $<1 \times 10^{-4}$ and $<1 \times 10^{-3}$ w.r.t. water (in %) in the summer and in the winter hemisphere, respectively. On the other hand, Goesmann et al. (2015) used formamide, among the other molecules, to fit the Cometary Sampling and Composition (COSAC) mass spectrum obtained by the Philae lander on the comet surface. They reported that the abundance of this molecule can be as high as 1.8% w.r.t. water. It is generally accepted that the dark refractory surface of a comet, i.e., the crust, is formed after cosmic-ray bombardment (Strazzulla et al. 1991). Taking into account our data, we suggest that the missing detection of formamide in the coma of comet 67P/Churyumov-Gerasimenko (Le Roy et al. 2015) and its simultaneous presence on the surface (Goesmann et al. 2015) is due to the fact that formamide is trapped in the crust of the comet because the temperature experienced throughout its orbit was not high enough to determine its sublimation.

To strengthen this work, the detection of solid-state formamide in star-forming regions would be of great importance. By this point of view, we expect that interesting results will be collected by the Near Infrared Spectrograph (NIRSpec) and the Mid-Infrared Instrument (MIRI) on board the James Webb Space Telescope (JWST), which launch is expected between March and June 2019.

Part IV

From the solid-phase synthesis to the gas-phase detections

Chapter 6

C_2O and C_3O in star-forming regions

Based on Urso, R. G., Palumbo, M. E., Ceccarelli, C. et al. in prep.

6.1 Carbon chain oxides

Although its harsh conditions, chemistry thrives in the interstellar medium (ISM), in particular in star-forming regions. Indeed, more than 200 interstellar molecules have been detected so far, most of them in regions of active star formation¹. In general, three different processes are invoked to explain the formation of molecules observed in the gas phase in star forming regions: (1) reactions taking place on the grain surfaces during the cold prestellar period of grain mantle formation (e.g., Tielens & Hagen 1982) and existence (e.g., Garrod & Herbst 2006); (2) gas-phase reactions taking place in the protostellar phase, once the icy mantles sublimate in the warm regions (e.g., Charnley et al. 1995); (3) energetic processing (i.e. ion irradiation and UV photolysis) of the mantles during the star formation process (e.g., Palumbo & Strazzulla 1993). When processes (1) and (3) occur, molecules formed in the solid phase are observed in the gas phase after desorption of the icy grain mantles. Although all three processes are very likely at work, it is not clear whether and when each of them is the dominant process. Yet, distinguishing what process operates in what conditions is crucial if we want to understand how the molecular complexity builds up in the ISM in general, and, more specifically, in regions where planetary systems like the Solar one will eventually form. Likewise, this might as well shed light on the formation of our own Solar System.

C_2O and C_3O , namely dicarbon monoxide or ketenylidene and tri-carbon monoxide, are particularly useful species in the game of understanding the respective importance of processes (2) and (3), namely the role of energetic processing on the grain mantles with respect to gas-phase reactions. On the one hand, Matthews et al. (1984) and Ohishi et

¹<http://www.astro.uni-koeln.de/cdms/molecules>

al. (1991) explained the observed abundances of both dicarbon and tri-carbon monoxide by electron recombination and ion-molecule gas-phase reactions. On the other hand, solid phase laboratory experiments have shown that several carbon chain oxides, among which C_2O and C_3O , are formed after ion irradiation and UV photolysis of CO-rich mixtures that simulate the icy mantles of dust grains (Strazzulla et al. 1997; Gerakines & Moore 2001; Trottier & Brooks 2004; Loeffler et al. 2005; Palumbo et al. 2008; Sicilia et al. 2012).

C_2O and C_3O belong to the linear carbon chain oxides family, molecules with the general formula C_nO , with $n \geq 2$. When n is an odd number, the molecules possess a closed shell electronic structure, while for even n they have an open shell electronic structure. This implies that the species with an odd number of carbon atoms are more stable and less reactive than those with an even number of carbons (Jamieson et al. 2006). Due to the high instability of these two molecules under ordinary pressures and temperatures, their properties have been investigated mostly by quantum chemical computations (e.g., Woon & Herbst 2009). Also, Etim et al. (2016) calculated the enthalpy of formation of both molecules showing that C_3O is more stable with respect to C_2O .

Both molecules have been detected in the gas phase in space. In particular, the first detection of C_3O was reported by Matthews et al. (1984) toward the dense molecular cloud TMC-1, while the first detection of C_2O was reported by Ohishi et al. (1991) in the same object. Later, C_3O was also detected toward Elias 18 (Palumbo et al. 2008), IRC +10216 (Tenenbaum et al. 2006) and L1544 (Vastel et al. 2014).

The goal of this work is to study the contribution of gas-phase reactions and energetic processing of icy mantles to the formation of both C_2O and C_3O . Thus, to better understand the formation and destruction routes of carbon chain oxides in the ISM, we used a multi-faced

and multi-disciplinary approach. We used observations carried out by means of different radio telescopes toward several sources, some of which reported here for the first time, and compared them with (i) the predictions obtained via an astrochemical model to simulate the gas-phase reactions, and (ii) the results from new laboratory experiments on ion irradiation of icy mantles analogues.

This chapter is organised as follows. In § 6.2 we present observational data on C_2O and C_3O , available in literature and new ones, toward several sources and estimate their abundance in each source. In § 6.3 we present the results of gas-phase modelling, the reaction network we used, and a parametric study of the predicted fractional abundances of C_2O and C_3O ratios as a function of time. In § 6.4 we present the experimental results obtained after ion bombardment of CO-rich solid films to simulate the energetic processing of icy mantles, the spectra acquired and the relative abundances of both molecules as a function of the fluence that we correlate to the time scale of stellar evolution. In § 6.5 we put together and discuss all the data obtained to infer the formation routes of dicarbon and tricarbon monoxide and the limits to our conclusions related to the modelling method we used.

6.2 Observations

Our data set consists of new and published observations of C₂O and C₃O. Our goal is to collect the measured column density of both species toward several sources and to calculate their fractional abundances with respect to H₂ and their relative abundance ratio. Please note that our goal is to investigate about the presence of both molecules during the star formation process, i.e. from a dark cloud to a protostar, so we only considered sources in star-forming regions².

C₂O and C₃O were previously observed in TMC-1, L1544 and Elias 18. In this work, we also obtained new observations (see next) towards L1498, L1544 and Elias18. Finally, we searched for the presence of C₂O and C₃O in the spectra of IRAS16293-2422 (Caux et al. 2011) and of the sources of the ASAI project (*Astrochemical Surveys At Iram*, Lefloch et al. 2017, <http://www.oan.es/asai/>), L1157-mm, L1157-B1, SVS13A, OMC-2 FIR4, and NGC1333-IRAS4A.

We first describe the source sample (§ 6.2.1), then the details on the new observations (§ 6.2.2), and finally we present the estimates abundances of C₂O and C₃O (§ 6.2.3).

6.2.1 Source sample

All sample sources are briefly described in the following section.

TMC-1 is a cold, quiet and dense dark cloud which is unusually carbon-rich and where both C₂O and C₃O were first detected (Matthews et al. 1984; Ohishi et al. 1991; Kaifu et al. 2004).

L1544 is a cold prestellar core on the verge of gravitational collapse

²We therefore excluded IRC +10216 from the discussion as it is an asymptotic giant branch (AGB) carbon-rich star Miller (1970).

(Caselli et al. 2002). Recently, one line attributed to C_3O has been reported by Vastel et al. (2014).

L1498 is a cold and dense pre/protostellar core, likely in the Class 0 phase Kuiper et al. (1996). Here we report about two C_3O lines detected toward this object (see § 6.2.2).

Elias 18 is a Class I protostar with a circumstellar disk oriented close to the edge-on. Tegler et al. (1995) suggested that it is in transition between an embedded young stellar object and an exposed T-Tauri star. Most of CO is still incorporated in icy mantles, as reported by Tielens et al. (1991), Chiar et al. (1995) and Nummelin et al. (2001). Palumbo et al. (2008) reported the detection of one C_3O line towards this object.

IRAS 16293-2422 is a Class 0 protostar in which a cold envelope surrounds two sources named I16293-A and -B (e.g., Wootten et al. 1989; Mundy et al. 1992; Jørgensen et al. 2016). The cold and extended envelope is very rich in molecules (e.g., Jaber et al. 2016). This source is the focus of the project *The IRAS 16293-2422 Millimeter And Submillimeter Spectral Survey* (TIMASSS, Caux et al. 2011).

L1157-mm is a edge-on Class 0 protostar within the L1157 dark cloud that drives a bipolar outflow (e.g., Bachiller et al. 2001; Chiang et al. 2012).

L1157-B1 is a shocked region that has been extensively studied because of its richness in molecules, mostly caused by the partial sputtering of the grain mantles (Lefloch et al. 2012, 2017; Codella et al. 2015; Fontani et al. 2014, e.g.). Codella et al. (2010) defined it as an ideal laboratory to study the effects of shocks on the gas chemistry. It is an ASAI source.

NGC1333-SVS13-A is one of the two brightest sources, named SVS13-A and -B, found in a small cluster of protostars. It is a Class I protostar associated with an extended outflow (Lefloch et al. 1998). A compact, hot and dense region detected toward SVS13A with IRAM

30-m, hints the presence of a hot corino, the first detected in a Class I source (Codella et al. 2016).

OMC-2 FIR4 is a young protocluster containing several protostars and clumps (Shimajiri et al. 2008; López-Sepulcre et al. 2013) in the Orion Molecular Complex. Due to the fact that the Sun formed in a cluster of stars (Adams 2010), FIR4 is considered an analogue of the Sun progenitor. Also, during its first formation steps, the Solar System experienced an intense irradiation of energetic particles (Gounelle et al. 2006), and a similar irradiation dose is found close to FIR4, producing an enhanced degree of ionisation (Ceccarelli et al. 2014; Fontani et al. 2017). Moreover, Shimajiri et al. (2015) suggested that FIR4 is an outflow-shocked region.

NGC1333-IRAS4A is a binary system in which two Class 0 objects are found, named IRAS4-A1 and IRAS4-A2 (e.g., Looney et al. 2000). IRAS4A was the second discovered hot corino (Bottinelli et al. 2004). It shows a spectrum rich in complex organic molecules (COMs) (e.g., Caselli & Ceccarelli 2012). The two sources are in different evolutionary stages, and among them IRAS4-A1 is the youngest. It drives a fast collimated jet associated with bright H₂ emission (Santangelo et al. 2015).

6.2.2 New observations

In Table 6.1 we summarize the sources that we investigated, the rotational frequencies of the C₂O and C₃O lines, the radiotelescope used, the status of the detection and the relevant references. For the ASAI sources (see above), we used the relevant spectra obtained via the observations described in Lefloch et al. (2017) and López-Sepulcre et al. (2015). For IRAS16293-2422, we used the publicly available dataset of TIMASSS (Caux et al. 2011).

Finally, we obtained new observations of C₂O and C₃O lines toward

L1498 and Elias 18 in 2009 May 3-4 and in 2011 July 23, using the IRAM telescope, and toward L1498 in 2008 July 23, using the IRA-Noto 32 m telescope.

Detection of the 38486.891 MHz C_3O line towards L1498 was achieved on 2008, July 23 with the 32 m radiotelescope in Noto (Italy) operated by INAF-Istituto di Radioastronomia. The observations were carried out using the 43 GHz receiver (that can be tuned in the 38-47 GHz range). The telescope has an active surface system that compensates the gravitational deformation of the primary mirror. The beam size of the telescope (HPBW) was about $54''$ at 43 GHz; The aperture efficiency of the telescope was about 0.28 at 43 GHz. The spectra were acquired with the ARCOS autocorrelator (Comoretto et al. 1990) in beam switch mode; two spectra, one for each polarization, were acquired simultaneously. The spectra were reduced by using the software XSpettro for the on-off difference, then CLASS software for the baseline subtraction and temperature calibration. More details can be found in Palumbo et al. (2008).

Detection of the 92227.853 MHz C_2O line and the 86593.685 MHz C_3O line towards Elias18 and the 86593.685 MHz C_3O line towards L1498 were achieved with the 30 m IRAM radiotelescope on 2011 July 23, 2009 May 3 and 2009 May 4, respectively. Detected lines were fitted by a gaussian curve, Table 6.2 reports frequencies, transitions and line parameters.

Table 6.1: Sources in which lines from C_2O and C_3O were searched for, their rotational frequencies, the single-dish telescope used and the project when relevant, the status of the detection, and the references. Please note that for the ASAI and TIMASSS sources (see text) we searched for the C_2O and C_3O in the entire IRAM spectra but give here only the expected brightest line frequency.

Source	Frequency (MHz)	Telescope Project	Detection	Reference
C_2O				
TMC-1	45826.7	Nobeyama	Y	Ohishi et al. (1991)
	22258.1	Green Bank	Y	"
L1544	92227.8	IRAM-ASAI	Y	This work
Elias 18	92227.8	IRAM	Y	This work
IRAS16293-2422	92227.8	IRAM-TIMASSS	N	This work
L1157-mm	92227.8	IRAM-ASAI	N	This work
L1157-B1	92227.8	IRAM-ASAI	N	This work
SVS13A	92227.8	IRAM-ASAI	N	This work
IRAS4A	92227.8	IRAM-ASAI	N	This work
OMC-2 FIR4	92227.8	IRAM-ASAI	N	This work
C_3O				
TMC-1	19243.5	Green Bank	Y	Matthews et al. (1984)
	48108.5	Nobeyama	Y	Brown et al. (1985)
	76972.6	Kitt Peak	Y	"
	86593.7	Kitt Peak	Y	"
	86593.7	FCRAO	Y	"
L1544	86593.7	IRAM-ASAI	Y	Vastel et al. (2014)
	96214.6	IRAM-ASAI	Y	"
L1498	38486.9	IRA-Noto	Y	This work
	86593.7	IRAM	Y	This work
Elias 18	38486.9	IRA-Noto	Y	Palumbo et al. (2008)
	86593.7	IRAM	Y	This work
IRAS 16293-2422	86593.7	IRAM-TIMASSS	N	This work
L1157-mm	86593.7	IRAM-ASAI	N	This work
L1157-B1	86593.7	IRAM-ASAI	N	This work
SVS13A	86593.7	IRAM-ASAI	N	This work
IRAS4A	86593.7	IRAM-ASAI	N	This work
OMC-2 FIR4	86593.7	IRAM-ASAI	N	This work

Table 6.2: Frequencies, transitions and line parameters of new detected lines

Species	Source	Frequency (MHz)	Transition	Line intensity (mK)	rms (mK)	FWHM (km/s)	V_{LSR} (km/s)
C ₂ O	Elias18	92227.853	4 ₅ - 3 ₄	9.1	2.4	0.697±0.193	6.540±0.077
	L1544	92227.853	4 ₅ - 3 ₄	16.2	2.8	0.351±0.084	7.191±0.042
	L1544	92363.286	4 ₄ - 3 ₃	11.7	2.7	0.351±0.064	7.179±0.028
	L1544	92718.800	4 ₃ - 3 ₂	9.5	3.3	0.349 ±0.070	7.206±0.035
C ₃ O	L1498	38486.891	4-3	12.7	3.8	1.083±0.097	7.17±0.50
	L1498	86593.685	9-8	12.1	2.2	0.452±0.069	7.884±0.031
	Elias18	86593.685	9-8	13.5	2.5	0.539±0.098	6.022±0.034

The column density was estimated from the line intensity following the procedure described by Goldsmith & Langer (1999), assuming that the source fills the antenna beam, that the line is optically thin and that $T_{ex}=20$ K. Figure 6.1 shows the C_3O lines detected towards L1498 and Elias 18, while Fig. 6.2 shows the C_2O lines detected toward L1544.

For IRAS16293-2422, the lines are not detected with a 2σ rms of 10 mK, while in the ASAI sources the 2σ rms is about 6 mK.

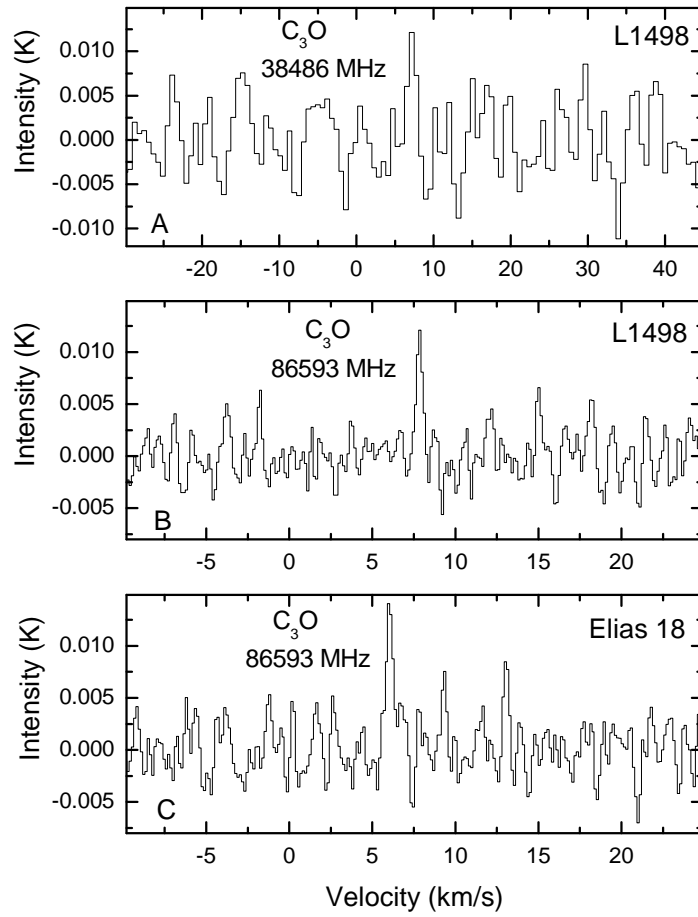


Figure 6.1: C_3O lines detected towards L1498 at: panel A) 38486 MHz (Noto-32m, 23 July 2008); panel B) 86593 MHz (IRAM-30m, 4 May 2009) C_3O line detected towards L1498 at: panel C) 86593 MHz (IRAM-30m, 3 May 2009).

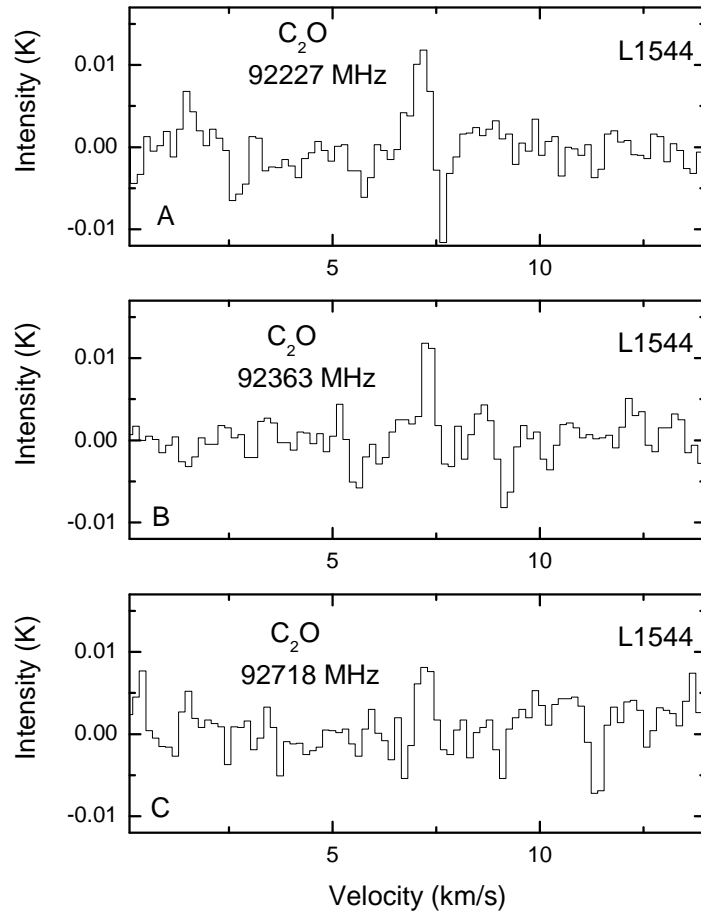


Figure 6.2: C_2O lines detected with IRAM 30 m towards L1544 at: panel A) 92227 MHz; panel B) 92363 MHz; panel C) 92718 MHz.

6.2.3 C₂O and C₃O abundances

In Table 6.3 we list the hydrogen column density for each source where either C₂O or C₃O are detected, the derived fractional abundances of C₂O and C₃O, and their abundance ratio.

Table 6.3: List of the source where C_2O or C_3O are detected. For each source we also list the molecular hydrogen column density (from literature estimates, also listed), the derived fractional abundances (with respect to H_2) of C_2O and C_3O and their relative abundance ratio. References: 1- Irvine et al. (1987); 2- Ohishi et al. (1991); 3- Brown et al. (1985); 4- Vastel et al. (2014); 5- Willacy et al. (1998); 6- Guelin et al. (1982); 7- this work.

Source	$N(H_2)$ ($\times 10^{22} \text{ cm}^{-2}$)	$x(C_2O)$ $\times 10^{-11}$	$x(C_3O)$ $\times 10^{-11}$	C_2O/C_3O	Reference
TMC-1	1	6.0	14	~ 0.4	1, 2, 3
L1544	0.5	20	5	~ 4	4, 7
L1498	5	–	0.7		5, 7
Elias 18	1	1.2	0.7	~ 1.7	6, 7

The analysis of the detections reported in Table 6.3 shows that C_2O and C_3O are only detected in a few sources of Table 6.1. Somehow surprising, all of them are cold prestellar objects (see the discussion in e.g. Loison et al. 2014). A possible exception could be represented by Elias 18, which is a more evolved object, but since the observations used a large beam we cannot exclude that the emission arises, also in this case, from the cold gas surrounding the object. Therefore, C_2O and C_3O are either connected with cold conditions or with early evolutionary times.

6.3 Modelling

The goal of this section is to provide predictions of C₂O and C₃O abundances, assuming that they are governed by gas-phase chemistry. We describe the astrochemical model that we used to this scope (§ 6.3.1), the chemical network (§ 6.3.2), and the resulting predictions obtained varying some crucial parameters (§ 6.3.3).

6.3.1 Model description

We ran a time-dependent, pure gas-phase chemistry model. To this end, we used the code Nahoon³, modified to improve its usage flexibility.

We model a molecular cloud completely shielded from the UV photons of the interstellar radiation field ($A_v=150$ mag), with a constant density of H nuclei, n_H , and a constant temperature T . We started with a partially atomic cloud, meaning that all elements are in the atomic form (neutral or ionised depending on their ionisation potential) except hydrogen, which is assumed to be in the molecular form. This mimics the pseudo-evolution of a cloud from neutral to molecular. The chemical composition of the cloud is left to evolve up to 5×10^6 years. The assumed elemental abundances are reported in Table 6.4.

In order to test the sensibility of the resulting predictions on the crucial parameters of the model, we varied: (i) the carbon abundance so to obtain a C/O elemental abundance ratio of 0.4, 0.65, 0.8 and 0.9, respectively; (ii) the cloud density between $2 \times 10^4 \text{ cm}^{-3}$ and $1 \times 10^5 \text{ cm}^{-3}$; (iii) the temperature T between 10 and 30 K; (iv) the cosmic-ray ion-

³The original code is publicly available at <http://kida.obs.u-bordeaux1.fr> (Wakeham et al. 2012)

ization rate ζ between 1×10^{-17} and $1 \times 10^{-16} \text{ s}^{-1}$. Finally, we also ran a few models to simulate the warm regions, called hot corinos, where the iced grain mantles sublimate.

Table 6.4: *Initial elemental abundances used in the models.*

Element or molecule	Initial abundance w.r.t. total H				
	C/O=0.4	C/O=0.8	C/O=0.663	C/O=0.9	C/O=0.8
H ₂	5.00×10^{-1}	5.00×10^{-1}	5.00×10^{-1}	5.00×10^{-1}	5.00×10^{-1}
He	9.00×10^{-2}	9.00×10^{-2}	9.00×10^{-2}	9.00×10^{-2}	9.00×10^{-2}
O	3.52×10^{-4}	1.83×10^{-4}	2.56×10^{-4}	1.89×10^{-4}	7.08×10^{-5}
C	1.46×10^{-4}	1.46×10^{-4}	1.70×10^{-4}	1.70×10^{-4}	5.67×10^{-5}
N	4.28×10^{-5}	4.28×10^{-5}	6.20×10^{-5}	6.20×10^{-5}	6.20×10^{-5}
S ⁺	1.60×10^{-7}	1.60×10^{-7}	8.00×10^{-8}	8.00×10^{-8}	8.00×10^{-8}
Si ⁺	1.60×10^{-8}	1.60×10^{-8}	8.00×10^{-9}	8.00×10^{-9}	8.00×10^{-9}
Fe ⁺	1.60×10^{-8}	1.60×10^{-8}	3.00×10^{-9}	3.00×10^{-9}	3.00×10^{-9}
Mg ⁺	1.40×10^{-8}	1.40×10^{-8}	7.00×10^{-9}	7.00×10^{-9}	7.00×10^{-9}
Cl ⁺	8.00×10^{-9}	8.00×10^{-9}	1.00×10^{-9}	1.00×10^{-9}	1.00×10^{-9}
P ⁺	6.00×10^{-9}	6.00×10^{-9}	2.00×10^{-10}	2.00×10^{-10}	2.00×10^{-10}
Na ⁺	4.00×10^{-9}	4.00×10^{-9}	2.00×10^{-9}	2.00×10^{-9}	2.00×10^{-9}
F	1.80×10^{-10}	1.80×10^{-10}	$(F^+) 1.00 \times 10^{-9}$	$(F^+) 1.00 \times 10^{-9}$	$(F^+) 1.00 \times 10^{-9}$

6.3.2 Chemical network

For the reactions occurring in the gas phase, we used the KIDA 2014 network², updated to take into account the carbon chains chemistry described in Loison et al. (2014), and other reactions involving C-bearing complex species described by Balucani et al. (2015) and Skouteris et al. (2017). In total, the network contains 507 species connected by 7210 reactions.

Fig. 6.3 shows a schematic diagram of the most important reactions involving C_2O and C_3O . The scheme was obtained a posteriori, looking at the most important formation and destruction reactions within the range of parameters used (see § 6.3.3). In the figure, all the chemical species that are connected by solid arrows show the formation reactions, while dashed arrows show the destruction pathways. As it is possible to notice, no reaction directly connecting C_2O and C_3O exists. In other words, the chemical network that we used does not contain any reaction in which C_2O is a reactant to form C_3O . Also, although a destruction reaction of C_3O that produces C_2O is included in the network, in practice it is completely negligible, its rate being from 10 to 15 orders of magnitude lower than the other reactions shown in the diagram.

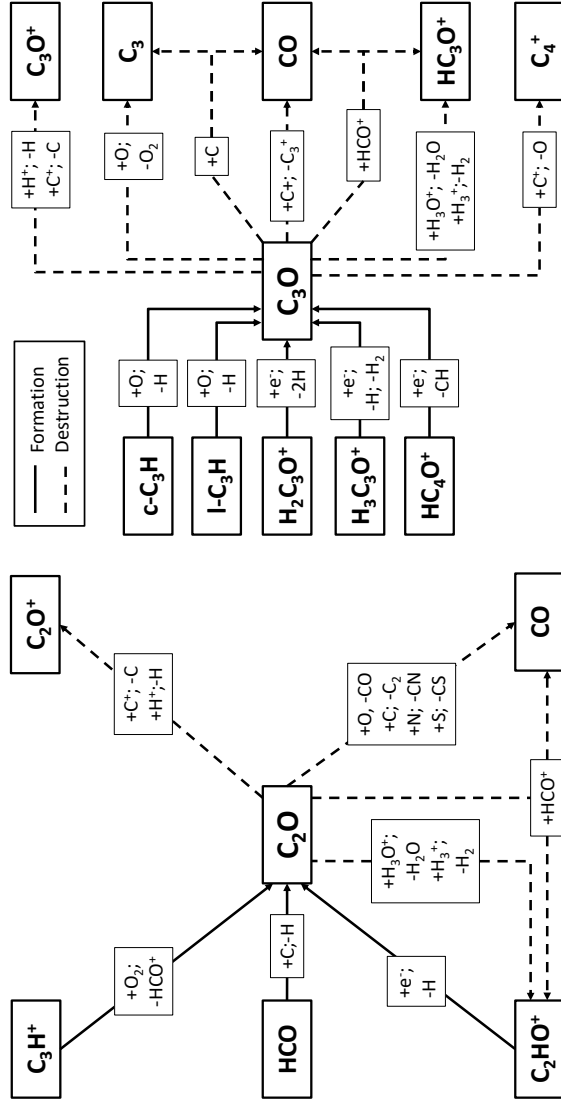


Figure 6.3: Reaction network including formation (solid lines) and destruction (dashed lines) of C_2O and C_3O . The boxes intercepting the arrows list the reactants, preceded by a plus sign, and other products, preceded by a minus sign, of the relevant reaction in which C_2O and C_3O are involved.

6.3.3 Results of the modeling

As mentioned at the beginning of the section, we ran two classes of models, which approximately described the two classes of objects where C_2O and C_3O were searched for: cold clouds and warm gas and hot corinos. We describe the predicted C_2O and C_3O abundances in the two cases separately. The results of the modeling are shown in Fig. 6.4, Fig. 6.5 and Fig. 6.6.

Cold cloud model

In Fig. 6.4 we show the predicted fractional abundances of C_3O (top panel) that have been computed for a cosmic-ray ionization rate of $1 \times 10^{-16} \text{ s}^{-1}$ and for 10, 20 and 30 K. The red boxes represent the range of observed fractional abundances toward the sources we consider in this work. Our results show that C_3O formation reach its maximum (about 10^{-9}) between 10^4 and 10^5 years. In most cases, at about $10^5 - 10^6$ years, the fractional abundances are in agreement with the observed values. For what concern C_2O , the model does not fit the observed abundances between 10^5 and 10^6 years (it predicts fractional abundances in the range $10^{-12} - 10^{-15}$), while it fits the observed range of fractional abundances at lower times, that are not consistent with the time scale of star formation, thus we do not show the results. The computation we carried out allowed us to obtain the C_2O over C_3O ratios as a function of time, shown in the bottom panels in Fig. 6.4. Here, green boxes represent the range of observed C_2O/C_3O ratios.

In Fig. 6.5 (top panels) the fractional abundance of C_3O have been computed for a lower cosmic-ray ionization rate, $1 \times 10^{-17} \text{ s}^{-1}$. Red boxes represent the range of observed fractional abundances. The lower ζ determines a shift in the formation maximum at about 10^5 years. At higher times and low temperatures (10 K) in most cases the fractional abundances fit the observed range; simulations show that the fractional abundances are progressively lowered with increasing temperature. Also in this case, the predicted abundances of C_2O do not fit the observed values. The bottom panels in Fig. 6.5 report the C_2O/C_3O ratios at the same. The green boxes represent the range of values obtained from the fractional abundance of C_2O and C_3O reported in Table 6.3. Both figures clearly points out that the modelled ratios do not

fit the range of values obtained by observations.

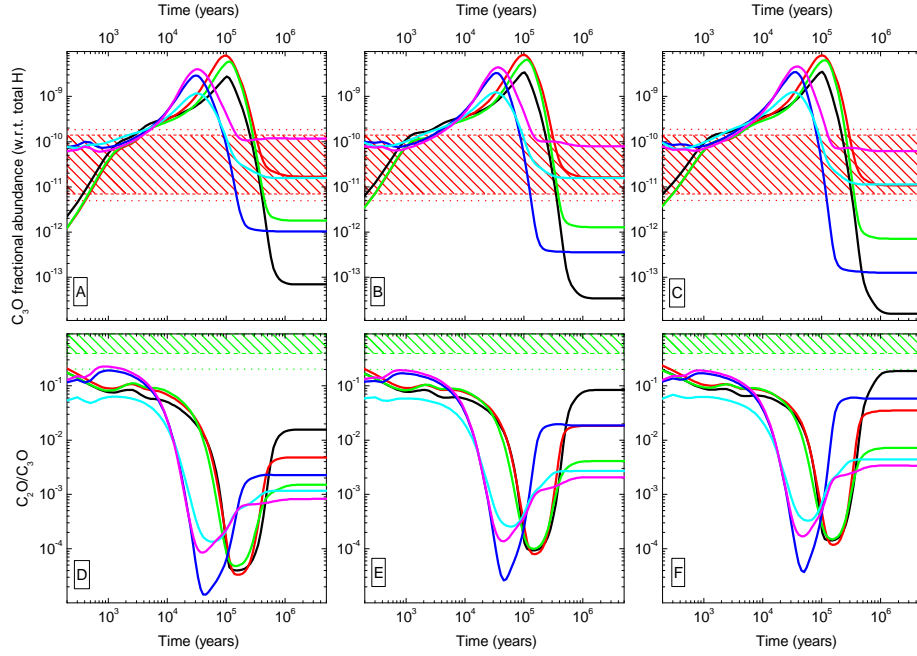


Figure 6.4: Computed abundance of C_3O (top panels) and C_2O/C_3O ratios (bottom panels) as a function of time (in years) for $\zeta=1\times 10^{-16} s^{-1}$ at: 10 K (panel A and D); 20 K (panel B and E); 30 K (panel C and F). Red boxes in top panel represent the range of observed fractional abundances for C_3O toward the sources considered in this work. Green boxes in bottom panel represent the range of observed ratios. The model has been run for different C/O initial ratios and hydrogen number density. Black line: $C/O=0.4$, $n_H=2\times 10^4 cm^{-3}$; red line: $C/O=0.8$, $n_H=2\times 10^4 cm^{-3}$; green line: $C/O=0.65$, $n_H=2\times 10^4 cm^{-3}$; blue line: $C/O=0.65$, $n_H=2\times 10^5 cm^{-3}$; cyan line: $C/O=0.8$, $n_H=2\times 10^5 cm^{-3}$; magenta line: $C/O=0.9$, $n_H=2\times 10^5 cm^{-3}$.

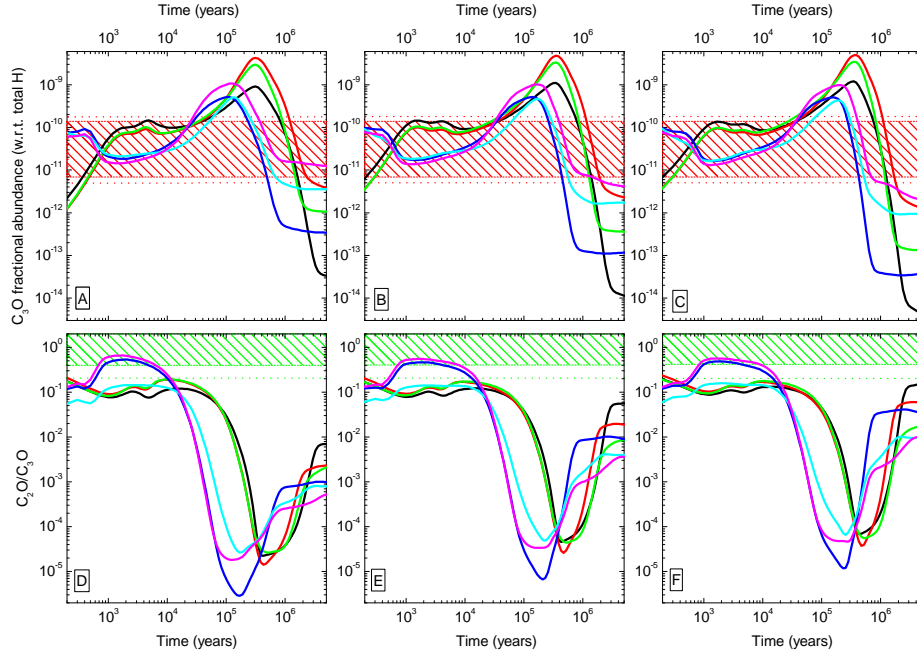


Figure 6.5: Computed abundance of C_3O (top panels) and C_2O/C_3O ratios (bottom panels) as a function of time (in years) for $\zeta=1\times 10^{-17} s^{-1}$ at: 10 K (panel A and D); 20 K (panel B and E); 30 K (panel C and F). Red boxes in top panel represent the range of observed fractional abundances for C_3O toward the sources considered in this work. Green boxes in bottom panel represent the range of observed ratios. The model has been run for different C/O initial ratios and hydrogen number density. Black line: $C/O=0.4$, $n_H=2\times 10^4 cm^{-3}$; red line: $C/O=0.8$, $n_H=2\times 10^4 cm^{-3}$; green line: $C/O=0.65$, $n_H=2\times 10^4 cm^{-3}$; blue line: $C/O=0.65$, $n_H=2\times 10^5 cm^{-3}$; cyan line: $C/O=0.8$, $n_H=2\times 10^5 cm^{-3}$; magenta line: $C/O=0.9$, $n_H=2\times 10^5 cm^{-3}$.

Warm gas and hot corino models

In Section , we showed that neither C_2O or C_3O are detected in warm sources, shock sites (like L1157-B1), warm clouds (OMC-2 FIR4) and hot corinos (IRAS16293-2422, SVS13A, IRAS4A). We, therefore, modeled also those regions, in order to understand why C_2O and C_3O are absent in warm gas.

In fact, is also important to understand the destruction pathways that can take place under the typical ISM conditions. With this in mind, we used the fractional abundances at the steady state as computed by the modelling at 10 K and for $n_H=1\times 10^7\text{ cm}^{-3}$ and $\zeta=3\times 10^{-17}\text{ s}^{-1}$ as input abundances. We wanted to know the time required for both molecules to be destroyed at higher temperature and density, to simulate the typical conditions of a protostellar envelope and an hot corino as given by Caselli & Ceccarelli (2012). Also, we modified the reaction network by setting the initial fractional abundance of both C_2O and C_3O at 10^{-9} . Simulations have been performed at 40 K (Fig. 6.6 panel A) and 100 K (Fig. 6.6 panel B). According to the model, even if the initial abundance for both molecules is set to 10^{-9} , at about 10^2 years they fall to 10^{-13} for C_3O and to 10^{-16} for C_2O . This trend is noticeable also for simulations at 100 K.

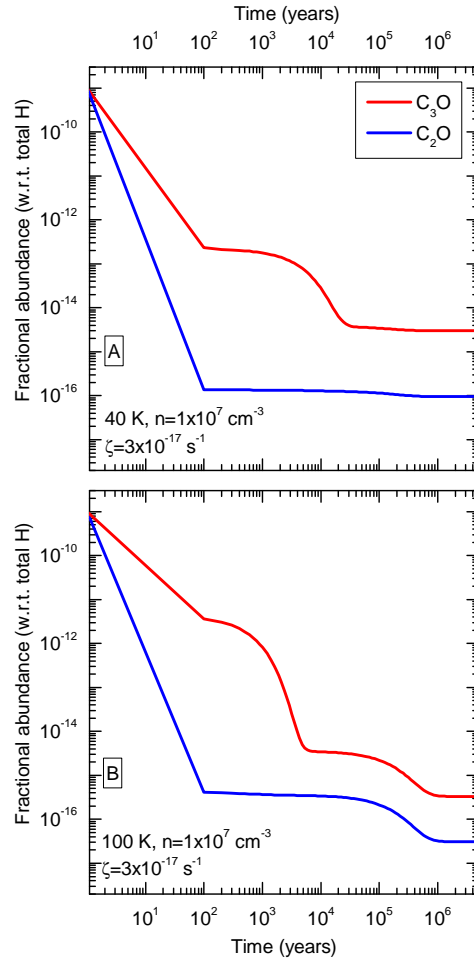


Figure 6.6: Computations to simulate the destruction of C_2O and C_3O for an hydrogen number density of $1 \times 10^7\text{ cm}^{-3}$, a cosmic-ray ionization rate of $3 \times 10^{-17}\text{ s}^{-1}$ at 40 K (panel A) and 100 K (panel B). Red line: C_3O ; blue line: C_2O .

6.4 Experimental results

The experimental results we show in this section are meant to extend the work by Palumbo et al. (2008) and Sicilia et al. (2012) about the effect of ion irradiation on frozen carbon monoxide when pure and in mixture with nitrogen films under high vacuum and at low temperature. These experiments simulate the effects due to the interaction between cosmic rays and icy mantles on dust grains, and they have been performed to study the formation of C_2O , C_3O and other carbon chain oxides after ion irradiation of CO-rich solid mixtures.

Experiments were performed in the Laboratory for Experimental Astrophysics (LAsp) at INAF-Osservatorio Astrofisico di Catania (Italy). The samples were prepared in a stainless steel high vacuum (HV) chamber (pressure $<10^{-7}$ mbar) in which a KBr substrate is placed in thermal contact with a cold finger whose temperature can vary between 16 K and 300 K. Once pure CO (Aldrich, 99.0%) and CO:N₂ (N₂ from Alphagaz, 99.9999%) mixtures were deposited on the substrate, we performed the irradiation with 200 keV H⁺. The samples were analyzed before, during and after ion irradiation using transmission infrared spectroscopy (2.5-25 μ m) to follow the modification induced by the ion beam. For more details about the experimental setup and methods please refer to Palumbo et al. (2008), Sicilia et al. (2012) and Urso et al. (2016).

In Fig. 6.7 we show the infrared spectra acquired during our experiment on ion irradiation of pure solid CO. Black dashed line shows the spectrum of a 990 nm CO ice deposited at 16 K. The vibrational band centred at about 2140 cm^{-1} is due to the fundamental CO stretching mode (e.g., Urso et al. 2016). Also, the high film thickness allows to

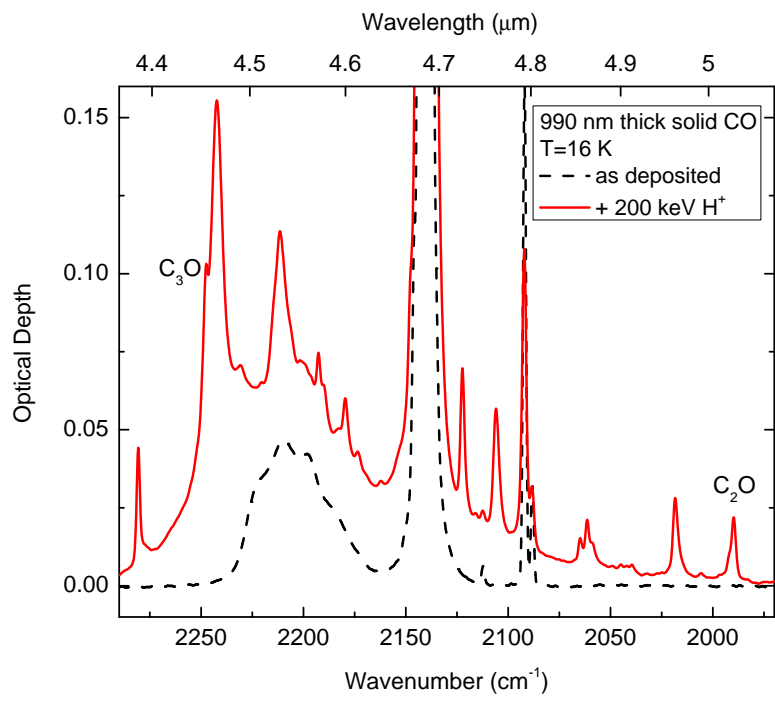


Figure 6.7: Infrared transmission spectra of solid CO as deposited at 16 K (black dashed line) and after irradiation with 200 keV H^+ (red solid line).

distinguish a broad feature between 2240 and 2160 cm^{-1} that is due to a combination of the fundamental CO stretching mode and a lattice vibration. The two blended peaks at about 2092 cm^{-1} are attributed to the stretching modes of the isotopologues $^{13}\text{C}^{16}\text{O}$ and $^{12}\text{C}^{18}\text{O}$, while the 2112 cm^{-1} band is due to $^{12}\text{C}^{17}\text{O}$ (Baratta & Palumbo 1998; Palumbo et al. 2008). The same figure shows the spectrum acquired after irradiation with 200 keV H^+ (red solid line) and it is possible to observe the appearance of several new features. The most intense band, observed at 2340 cm^{-1} (4.27 μm) is due to the formation of CO_2 (not shown), which is the most abundant molecule formed after the energetic processing of CO samples (e.g., Trottier & Brooks 2004; Loeffler et al. 2005; Seperuelo-Duarte et al. 2010). Other bands are due to the synthesis of more complex molecules. Most of them have been attributed to several carbon chain oxides (Palumbo et al. 2008; Sicilia et al. 2012). Among them, the stretching modes of C_2O and C_3O lay at 1988 and 2247 cm^{-1} , respectively.

We used these stretching mode bands to obtain the column density of both molecules synthesized after ion irradiation of solid CO. We calculated their column densities in units of molecules cm^{-2} through the formula

$$N = \frac{\int \tau(\nu) d\nu}{A} \quad (6.1)$$

where $\tau(\nu)$ is the optical depth and A is the band strength (cm molecule $^{-1}$). For both IR modes we used a band strength value of 1×10^{-17} cm molecule $^{-1}$, as reported by Palumbo et al. (2008).

Also ion irradiation of CO:N_2 solid mixtures drives to the formation of both dicarbon and tricarbon monoxide. The infrared spectra of different mixtures and the band assignment have been already shown in Sicilia et al. (2012), so we do not report about them in this work.

Fig.6.8 shows the column densities of C_2O and C_3O w.r.t. initial

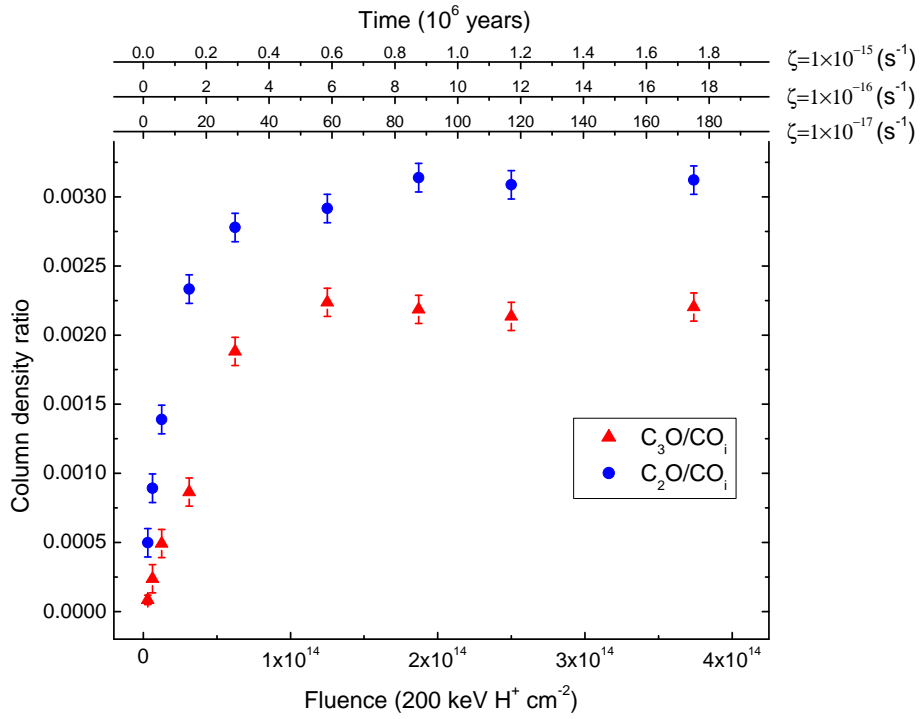


Figure 6.8: C_2O (blue circles) and C_3O (red triangles) column densities with respect to the initial CO column density (CO_i) as a function of fluence (ions cm^{-2} , bottom x-axis). Top x-axes give an estimate of the time (in 10^6 years) necessary for interstellar ices to undergo the effects observed in the laboratory. Values of cosmic-ray ionization rate used to calculate time scales are reported near each x-axis in the figure.

CO as a function of ion fluence after irradiation of CO at 16 K. The column densities have been obtained from the 1989 cm^{-1} and 2247 cm^{-1} bands, for C_2O and C_3O respectively, in the same procedure reported by Palumbo et al. (2008). Being the 2140 cm^{-1} band saturated, the CO initial column density has been calculated from the sample thickness that has been obtained from the interference curve given by a He-Ne laser during the deposition (e.g., Fulvio et al. 2009; Urso et al. 2016), assuming a sample density of 0.8 g cm^{-3} (Loeffler et al. 2005). The top axis gives an estimation of the time necessary for interstellar ices to undergo the effects observed in laboratory.

In Fig.6.9 we show the ratio between the column densities of C_2O and C_3O as a function of ion fluence in cm^{-2} we obtained after ion irradiation of pure CO, $\text{CO:N}_2=1:1$, $\text{CO:N}_2=8:1$ and $\text{CO:N}_2=1:8$ mixtures. The green box represent the range of observed $\text{C}_2\text{O}/\text{C}_3\text{O}$ ratios (given in Table 6.3). The top x-axis gives an estimate of the time (in 10^6 years) necessary for interstellar ices to undergo the effects observed in laboratory. To extrapolate the experimental results to the typical ISM conditions, we followed the method described in Palumbo (2006) and Kaňuchová et al. (2016) and the approximation for cosmic-ions energy reported by Mennella et al. (2003). The time scales on top x-axis have been calculated considering three values of cosmic-ray ionization rate, 1×10^{-15} , 1×10^{-16} and $1\times 10^{-17}\text{ s}^{-1}$, as reported on the right hand side of each axis. It is possible to observe that the higher ratio between C_2O and C_3O has been reached after the first ion irradiation step, i.e. at the lower fluence value of $3.2\times 10^{12}\text{ H}^+\text{cm}^{-2}$. We also observed that the $\text{C}_2\text{O}/\text{C}_3\text{O}$ ratio decreases as the fluence increases.

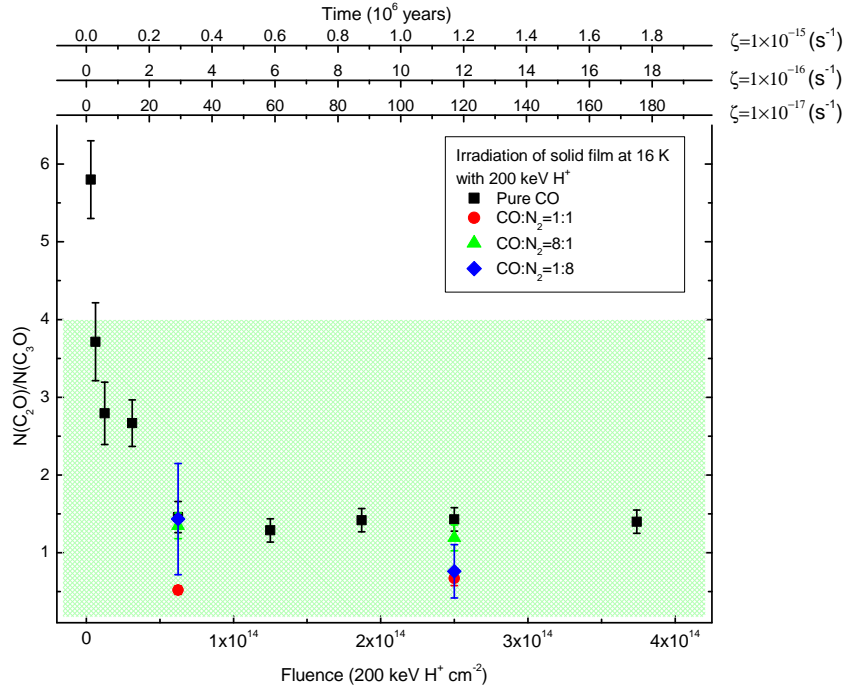


Figure 6.9: C_2O/C_3O ratio as a function of fluence (ions cm^{-2} , bottom x-axis) obtained after ion irradiation of pure CO (black squares), CO:N₂=1:1 mixture (red circles), CO:N₂=8:1 (green triangles) and CO:N₂=1:8 (blue rhombus). Top x-axes give an estimate of the time (in 10^6 years) necessary for interstellar ices to undergo the effects observed in the laboratory. Values of cosmic-ray ionization rate used to calculate time scales are reported near each x-axis in the figure. The green box represent the range of observed C_2O/C_3O ratios in space.

6.5 Discussion

Let's now assemble all the information we obtained from observations, modelling and laboratory experiments. We have shown that dicarbon and tricarbon monoxide have been detected in TMC-1, L1544, L1498 and Elias 18. The results we obtained modelling the formation and destruction of both molecules predict that their observed fractional abundances cannot be explained only taking into account gas-phase reactions occurring at the typical physical and chemical parameters of the ISM. This means that other processes have to be involved to explain the presence of C_2O and C_3O in the gas phase. According to our results, the interaction of cosmic rays with icy mantles is a possible candidate. In fact, in Fig. 6.7 we shown that ion irradiation of CO-rich films produce both C_2O and C_3O .

Taking into account the examined sources, the C_2O and C_3O fractional abundance is of the order of 10^{-11} - 10^{-10} . In dense molecular clouds, the CO fractional abundance is in the order of 10^{-4} , thus the carbon chain oxides abundance w.r.t. CO is about 10^{-7} - 10^{-6} . We carried out quantitative analysis to infer the amount of both species produced after ion bombardment. In Fig. 6.8 we show the results of calculation we made to assess the amount of both chain oxides produced during the irradiation of solid CO at 16 K. C_2O and C_3O resulted to be 3×10^{-3} and 2×10^{-3} w.r.t. the CO initial abundance, respectively. If we assume high CO depletion from interstellar ices, and that the C_2O and C_3O over CO ratio obtained in the experiments is maintained in the gas phase after the icy grain mantles desorption, we find that about 10^3 years would be necessary to form the observed column densities for both carbon chain oxides (see the top x-axis in the figure). Taking into

account that the evolution timescale of dense clouds is much longer, the observed gas-phase abundances could be reached even if only a fraction of icy grain mantles desorption occurs or if CO is not completely depleted.

Moreover, in Fig. 6.9, we have shown that the ratios between C₂O and C₃O produced after ion irradiation are comparable with those observed toward the sources in exam. These new results strengthen the hypothesis suggested by Palumbo et al. (2008), i.e. that both molecules are produced in the solid phase and then injected in the gas phase because of icy mantle desorption.

We also correlated the measured fluence to the time needed for ices to undergo the same effects observed experimentally. Taking into account a $\zeta=1\times 10^{-17} \text{ s}^{-1}$, the lower value we considered, the time required to observe the same ratio obtained in laboratory is about 2×10^6 years. Increasing ζ to $1\times 10^{-16} \text{ s}^{-1}$ the time needed is about 2×10^5 years.

Our results are also in agreement with the fact that both dicarbon and tricarbon monoxide have been detected in cold sources, in which there is not a central object warming up the material. In fact, we suggest that both molecules are formed in the solid phase. When non-thermal desorption mechanisms take place in young objects they occur at low temperature, as an example, because of photodesorption, grain-grain collisions, turbulence, sputtering or grain explosion induced by cosmic-rays (e.g., Boland & de Jong 1982; Hasegawa & Herbst 1993; Bringa & Johnson 2004; Ivlev et al. 2015); then, C₂O and C₃O are injected in the gas phase where they are detected and even if they are destroyed, they are continuously injected by the solid phase. Icy mantles rich in CO are processed by energetic cosmic ions, giving rise to both dicarbon and tricarbon monoxide, that are then released to the gas phase where they are destroyed but continuously re-injected by solid phase desorption, allowing the detection by means of radio telescopes.

The sublimation temperature of several C_nO species has been investigated by Jamieson et al. (2006). After ion irradiation of solid CO at 10 K they performed Temperature Programmed Desorption (TPD) analysis. They have shown that C_3O sublimate together with the matrix at about 42 K, while CO_2 , C_3O_2 and C_5O_2 remain in the ice. After irradiation, ketenylidene is unstable also at 10 K in the solid phase, and it probably undergoes a reaction with CO from the matrix to form C_3O_2 (Jamieson et al. 2006), thus it has to be continuously produced by the interaction of icy mantles with cosmic-rays to explain its presence in the gas phase.

In more evolved objects, such as IRAS 162593-2422 and L1157-B1, the higher temperature or the presence of shocks cause the complete sublimation of icy grain mantles. As a consequence, the bare grains cannot act as a reservoir of molecules, and we have shown that gas-phase reactions are not able to produce the right amount of C_2O and C_3O . So, even if both molecules were injected in the gas phase in a previous stage of star formation, after their destruction they cannot be produced in a reasonable amount, as suggested by the modelling we ran at 40 and 100 K shown in Fig.6.6. In this discussion, Elias 18 could appear as an anomaly. In fact, even if it is a low mass protostar, both molecules have been detected. These detections have been possible because a circumstellar disk oriented close to the edge-on is present, and most of CO is still incorporated in icy grain mantles, as reported by Tielens et al. (1991), Chiar et al. (1995) and Nummelin et al. (2001). Solid CO is then processed by cosmic rays or stellar wind ions, giving rise to both C_2O and C_3O that are then injected in the gas phase.

It is well known that icy mantles are not made of pure CO; IR spectra acquired toward several sources revealed they are mixtures or layered films containing water and carbon monoxide as major components. Also other molecules are present, such as methanol and carbon

dioxide (Boogert et al. 2015). N_2 cannot be detected in the solid phase, but is depleted from the gas phase (Caselli et al. 2002; Bergin et al. 2002). Laboratory experiments have shown that carbon chain oxides are produced even in mixtures containing CO and N_2 in different ratio, together with NO, N_2O , NO_2 , OCN and NCO, after irradiation with 200 keV H^+ at low temperature (Sicilia et al. 2012).

Once we gave this picture about the reasons beneath the detections we have shown, or the missing detections, about C_2O and C_3O in the gas phase of several sources in the ISM, we also want to expose the problems we faced when modelling the gas-phase reactions. As said in §6.3 we coupled the Nahoon code with an updated version of the KIDA network. The reaction diagram we proposed in Fig. 6.3 is based on the results carried out by this model. We have shown 26 reactions that form and destroy both C_2O and C_3O . But only less than 27% of these reactions have been positively evaluated on the KIDA website, while the remaining are not evaluated, and, as reported by Wakelam et al. (2012) being obtained from another database (OSU) that relies more heavily on unstudied radical-neutral reactions. Of course, even if it is a powerful tool to investigate the gas phase of the ISM, this lack of both experimental and theoretical data about possible reactions and their rates could imply huge inaccuracies. Also, neither the standard KIDA network nor our version contain reactions in which C_2O is involved as a reactant to produce C_3O through a reaction with atomic carbon. As an example, Jamieson et al. (2006) proposed a solid phase reaction occurring between C_2O and carbon atoms present in a CO matrix after ion irradiation experiments and giving rise to C_3O . Of course, there are no evidences that this reaction could occur also in the gas phase of the ISM, and its evaluation is not among the purposes of this work.

In conclusion, laboratory experiments and modelling here shown suggest that the observed fractional abundances of dicarbon and tri-

carbon monoxide in the gas phase of the ISM are due to the energetic processing of CO-rich icy mantles and their subsequent desorption because of non thermal processes. Once in the gas phase, both molecules are easily destroyed. The low reaction rates to produce both molecules hinder their formation directly in the gas phase, thus their detection would not be possible, unless the continuous re-injection from the solid phase occurs.

Chapter 7

Conclusions

The results reported in this work point out the fundamental role of energetic processing in modifying the structure of icy bodies, such as icy grain mantles and comets (part II), their composition (part III) and also the composition of the gas phase, due to sublimation or sputtering of species synthesised on grains (part IV). In chapter 2 we have shown experimental results that mainly have implication on the study of the icy grain mantles structure. In particular, based on the laboratory results presented, we conclude that the profile of the stretching mode band of solid CO obtained following the thin-film deposition technique both in IR and Raman spectra does not provide evidence for any modification after warm up or ion irradiation. As a consequence, the comparison between laboratory and astronomical spectra acquired by infrared telescopes cannot be used to draw any conclusion on the structure of solid CO in space. Also, Raman analysis performed after the irradiation of solid CO allowed us to detect two features, one at 1767 cm^{-1} that remains unidentified and the second one at 1817 cm^{-1} that we attribute to C_2 .

In Chapter 3 we have presented a study on the profile of the O-D stretching mode band in various solid mixtures containing water and

deuterated water. We have investigated the role of the dilution, of the structure of the sample (porous, amorphous or crystalline) and of ion bombardment (200 keV H^+). We have found that the above parameters may influence the ratio between the O-D and the O-H stretching mode band. As a consequence, to estimate the $\text{HDO}/\text{H}_2\text{O}$ ratio in astrophysical ices requires the observations of both the O-H stretching mode band and the O-D stretching mode band. The profile of the non saturated O-H feature gives an estimation of the fraction of crystalline ice along the line of sight, which in turn gives an estimation of the average temperature along the line of sight. As it has been shown, the ratio between the O-H and O-D stretching mode band areas is independent of the temperature of the sample when the concentration of HDO is of the order of few percent while it strongly depends on the sample temperature when the concentration of HDO is of the order of 0.1 % or less.

In part III the role of the energetic processing in the synthesis of new species within ices has been shown. In particular, we investigated the formation of HNCO and NH_2CHO after the bombardment with 30 keV He^+ and 200 keV H^+ of solid mixtures that are thought to be representative of icy grain mantles and cometary surfaces composition. The results pointed out that energetic processing of ice can quantitatively reproduce the amount of NH_2CHO observed in cometary comae and in many circumstellar regions. HNCO is also formed, but additional formation mechanisms are requested to quantitatively account for the astronomical observations. We suggest that energetic processing of ices in pre- and protostellar regions and in comets is the main mechanism to produce formamide, which, once it is released in the gas phase because of desorption of ices, is observed in the gas phase in these astrophysical environments.

In chapter 5, we have shown experimental results on the thermal

evolution of solid state formamide as a pure sample, in mixture with water or carbon monoxide and after its synthesis in interstellar ice analogues. Amorphous formamide crystallizes at 170 K. We observed the presence of the LO-TO splitting in the CO stretching mode band of both amorphous and crystalline samples. When deposited in mixtures, we observed that some water and CO molecules can remain trapped in the formamide layer at temperatures higher than their desorption temperatures. In the high dilution experiments, we have been able to detect vibrational bands attributed to formamide monomers and dimers isolated in a CO matrix. In all these experiments, formamide desorption has been observed at 220 K. The irradiation experiment with 200 keV H^+ on a mixture containing nitrogen, methane and water shows that formamide is synthesized and that after heating to 296 K molecules remain trapped within the refractory residue. Our results indicate that the injection of formamide in the gas phase in star-forming regions requires temperature as high as 300 K or non-thermal processes, such as grain explosion and sputtering. Also, we suggest that the missing detection of formamide in the coma of comet 67P/Churyumov-Gerasimenko and its presence on the surface is due to the trapping in the crust.

In part IV we reported about observations, laboratory experiments and models with the aim to understand how both C_2O and C_3O are synthesised in star-forming regions. The results suggest that the fractional abundances observed toward the investigated regions in space are due to the energetic processing of CO-rich icy mantles and their subsequent desorption because of non thermal processes. Once in the gas phase, both molecules are easily destroyed. The low reaction rates to produce both molecules hinder their formation directly in the gas phase, thus their detection would not be possible, unless the continuous re-injection from the solid phase occurs.

The experimental results here shown have been obtained using in-

frared and Raman spectroscopy. As discussed, the main advantages of both techniques are the in-situ analysis, fundamental to investigate frozen matter at low temperature, and the direct comparison with infrared astronomical spectra. However, more sensitive techniques are required to study the formation of minor species in the irradiated samples. In the near future, the LAsp experimental setup will be upgraded with an additional UHV chamber in which a Time Of Flight Ion Mass Spectrometer will allow to perform both qualitative and quantitative in-situ analysis with an higher sensitivity with respect to IR spectroscopy. Also, other techniques are required to better understand the physical and chemical properties of refractory residues. As an example, X-ray Photoelectron Spectroscopy (XPS) and Atomic Force Microscopy (AFM) are in use to analyse residues that have been exposed to both laboratory irradiation and space irradiation on board of the International Space Station within the Photochemistry on the Space Station (PSS) project (Baratta et al. 2015, *Planetary and Space Science*, 211-220).

Finally, the results reported acquire particular relevance in view of the James Webb Space Telescope (JWST) launch, that is scheduled in between March and June 2019. We expect that the Near Infrared Spectrograph (NIRSpec) and the Mid-Infrared Instrument (MIRI) on board, covering the wavelength range from $0.6 \mu\text{m}$ to $28 \mu\text{m}$, will provide intriguing data that will be largely used to study the chemical composition and physical structure of different objects in space and, among them, of the icy mantles of dust grains in the ISM. Thus, the constrains given in this work could contribute to a better interpretation of future data.

Bibliography

- Abdulgalil, A. G. M., Marchione, D., Thrower, J. D. et al. 2013, *Physical and Engineering Sciences*, 371
- Accolla, M. Congiu, E., Dulieu, F., et al. 2011, *PCCP*, 13, 8037-8045
- Adams, F. C. 2010, *ARAA*, 48, 47
- Aikawa, Y., Kamuro, D., Saikon, I., Itoh, Y., Terada, H., Noble, J. A., Pontoppidan, K. M., Fraser, H. J., Tamura, M., Kandori, R., Kawamura, A. and Ueno, M. 2012, *A&A*, 538, A57
- Allamandola, L. J., Sandford, S. A. & Tielens, A. G. G. M. 1992, *ApJ*, 399, 134-146
- Allodi, M. A., Baragiola, R. A., Baratta, G. A. et al. 2013, *Space Sci. Rev.*, 180, 101-175
- Bachiller, R., Gutiérrez, M., Kumar, M. S. N. and Tafalla, M. 2001, *A&A*, 372, 899
- Balucani, N., Ceccarelli, C., Taquet, V. 2015, *MNRAS*, 449, L-16
- Baragiola, R. A. 2003, *Planet. Space Sci.*, 51, 953-961
- Baratta, G. A., Leto, G., Spinella, F. et al. 1991, *A&A*, 252, 421
- Barone, V., Latouche, C., Skouteris, D., Vazart, F., Balucani, N., Ceccarelli, C., Lefloch, B. 2015, *MNRAS*, 453, L31, doi:10.1093/mnras/slv094
- Baratta G. A., Arena M. M., Strazzulla G. et al. 1996, *NIMPB*, 116, 195
- Baratta, G.A. and Palumbo, M.E. 1998, *Journal of the Optical Society of America A*, 15, 12, 3076
- Baratta, G. A., Palumbo, M. E. & Strazzulla, G. 2000, *A&A*, 357, 1045
- Baratta, G. A., Chaput, D., Cottin, H. et al. 2015, *Planet. Space Sci.*, 118, 211
- Bennett, C. J., Chen, S. H., Sun, B. J., Chang, A. H. H. & Kaiser, R. I. 2007, *ApJ*, 660, 1588
- Bennett, C. J. & Kaiser, R. I. 2007, *ApJ*, 661, 899
- Bergantini, A., Pilling, S., Nair B. G., et al. 2014, *A&A* 570, A120
- Bergin, E.A., Alves, J., Huard, T., & Lada, C.J. 2002, *ApJ*, 570, L101
- Bernstein, M. P., Sandford, S. A., Allamandola, L. J., et al. 1995, *ApJ*, 454, 327

- Bernstein, M. P., Dworkin, J. P., Sandford, S. A., Cooper, G. W. & Allamandola, L. J. 2002, *Nature*, 416, 401
- Bird, M. K., Huchtmeier, W. K., Gensheimer, P., et al. 1997, *A&A*, 325, L5
- Bisschop S. E., Jorgensen J. K., van Dishoeck E. F., et al. 2007, *A&A*, 465, 913
- Biver, N., Bockelée-Morvan, D., Debout V., et al. 2014, *A&A*, 566, L5
- Bockelée-Morvan, D., Lis, D. C., Wink, J. E. et al. 2000, *A&A*, 353, 1101-1114
- Bohren, C. F. & Huffman, D. R. 1983, *Absorption and Scattering of Light by Small Particles*, Wiley, New York
- Boland, W., & de Jong, T. 1982, *ApJ*, 261, 110
- Boogert, A. C. A., Schutte, W. A., Helmich, F. P., Tielens A. G. G. M. and Wooden, D. H. 1997 *A&A*, 317, 929
- Boogert, A. C. A., Ehrenfreund, P., Gerakines, P. A., Tielens, A. G. G. M. et al. 2000, *A&A*, 353, 349
- Boogert, A. C. A., Blake, G. A. and Tielens, A. G. G. M. 2002, *ApJ*, 577, 271-280
- Boogert, A. C. A., Pontoppidan, K. M., Knez, C. et al. 2008, *ApJ*, 678, 985-1004
- Boogert, A.C., Gerakines, P.A., & Whittet, D.C.B. 2015, *ARAA*, 53, 541
- Bottinelli, S., Ceccarelli, C. Lefloch, B., Williams, J. P. et al. 2004, *ApJ*, 615, 354
- Bossa, J.-B., Isokoski, K., de Valois M.S. et al. 2012, *A&A*, 545, A82
- Bringa, E.M., & Johnson, R.E. 2004, *ApJ*, 603, 159
- Brown, R. D., Godfrey, P. D., Cragg D. M. and Rice, E. H. N. 1985, *ApJ*, 297, 302
- Brown, R. H., Cruikshank, D. P., Veverka, J., Helfenstein, P. & Eluszkiewicz, J. 1995, *Neptune and Triton* (Tucson: University of Arizona Press), p. 991
- Brucato, J. R., Palumbo, M. E. & Strazzulla, G. 1997, *Icarus*, 125, 135
- Brucato, J. R., Baratta, G. A. & Strazzulla, G. 2006, *A&A*, 455, 395
- Butner, H. M., Charnley, S. B., Ceccarelli, C., Rodgers, S. D., Pardo, J. R., Parise, B., Cernicharo, J. and Davis, G. R. 2007, *ApJ*, 659, L137-L140
- Burke, D. J., Puletti, F., Woods, P. M. et al. 2015, *J. Chem. Phys.*, 143, 164704
- Calvin, W. M., Clark, R. N., Brown, R. H. & Spencer, J. R. 1995, *J. Geophys. Res.*, 100, 19041
- Capaccioni, F., Corradini, A., Filacchione, G., et al. 2015, *Science* 347, aaa0628
- Caselli, P., Walmsley, C.M., Zucconi, A., Tafalla, M., Dore, L., Myers, P.C. 2002, *ApJ*, 565, 331
- Caselli, P., van der Tak, F. F. S., Ceccarelli, C., Bacmann, A. 2003, *A&A*, 403, L37

- Caselli, P. 2005, *Chemical Processes in Star Forming Regions, Cores to Clusters: A Scientific Autobiography*, ed. Kumar, M. S. N., Tafalla, M. and Caselli, P., Springer, New York, 47-66
- Caselli, P. & Ceccarelli, C. 2012, *A&A Rev.*, 20, 56
- Cazaux, S., Caselli, P. & Spaans, M. 2011, *ApJ Letters*, 741, L34
- Ceccarelli, C., Dominik, C., López-Sepulcre, A., Kama, M., Padovani, M., Caux, E. & Caselli, P. 2014, *ApJ*, 790, L1
- Ceccarelli, C.,
- Caux, E., Kahane, C., Castets, A., Coutens, A., Ceccarelli, C. et al. 2011, *A&A*, 532, A23
- Chang, H.C, Richardson, H. H., Ewing, G. E., 1988, *J. Chem. Phys.*, 89, 7561
- Charnley, S. B., Kress, M.E., Tielens, A. G. G. M., & Millar, T. J. 1995, *ApJ* 448, 232
- Chiar, J. E., Adamson, A. J., Kerr, T. H., & Whittet, D. C. B. 1995, *ApJ*, 455, 234
- Chiang, H.-F., Looney, L. W. and Tobin, J. J. 2012, *ApJ*, 756, 168
- Chyba, C. & Sagan, C. 1992, *Nature*, 355, 125-132
- Codella, C., Lefloch, B., Ceccarelli, C., Cernicharo, J., Caux, E., Lorenzani, A., Viti, S., Hily-Blant, P. et al. 2010, *A&A*, 518, L112
- Codella, C., Fontani, F. Ceccarelli, C., Podio, L., Viti, S., Bachiller, R., Benedettini, M., Lefloch, B. 2015, *MNRAS*, 449, L11
- Codella, C., Ceccarelli, C., Bianchi, E., Podio, L., Bachiller, R., Lefloch, B., Fontani, F. Taquet, V. & Testi, L. 2016, *MNRAS*, 462, L75
- Collings, M. P., Anderson, M. A., Chen, R. et al. 2004, *MNRAS*, 354, 1133
- Combes, M., Moroz, V. I., Crovisier, J. et al. 1988, *Icarus*, 76, 3, 404-436
- Comoretto, G., Palagi, F., Cesaroni, R. et al. 1990, *A&ASS*, 84, 179
- Costantini J.-M., Couvreur F., Salvetat J.P. et al. 2002, *NIMPB*, 194, 132
- Coutens, A., Vastel, C., Hincelin, U., Herbst, E. et al. 2014, *MNRAS*, 445, 1299
- Crimer, N., Ceccarelli, C., Lefloch, B. and Faure, A. 2009, *A&A*, 506, 1229
- Crovisier, J. 1997, *Earth, Moon, and Planets*, 79, 1-3, 125-143
- Crovisier, J. & Bockelée-Morvan, D. 1999, *SpSciRev* 90, 19
- Cruikshank, D. P., Veverka, J. & Lebofsky, L. A. 1984, *Saturn* (Tucson: University of Arizona Press), p. 640
- Cruikshank, D. P., Brown, R. H., Calvin, W. M., Roush, T. L. & Bartholomew, M. J. 1995, *Solar System Ices* vol. 227 (Dordrecht: Kluwer Academic Publisher - ASSL Series) p. 579
- Cuppen, H. M., Penteado, E. M., Isokoski, K. et al. 2011, *MNRAS*, 417, 2809

- Dalgarno, A. 2006, PNAS, 103, 33, 12269
- Dartois, E. & d'Hendecourt, L. 2001, A&A, 365, 144
- Dartois, E., Thi, W.-F., Geballe, T. R., Deboffle, D., d'Hendecourt, L. and van Dischoeck, E. 2003, A&A, 399, 1009-1020
- Dartois, E. 2005, Space Sci Rev, 119, 293
- Dartois, E. 2006, A&A, 445, 959
- Dartois, E., Ding, J. J., de Barros, A. L. F., et al. 2013, A&A, 557, A97
- Dartois, E., Augé, B., Boduch, P. et al. 2015, A&A, 576, A125
- Dawley, M. M., Pirim, C. & Orlando, T. M. 2014, J. Phys. Chem. A, 118, 1220
- Demyk, K., Dartois, E., d'Hendecourt, L., & al. 1998, A&A 339, 553
- d'Hendecourt, L. & Allamandola, J. L. 1986, A&A Suppl. 64, 453
- Douglas, A. E. & Herzberg, G. 1941, ApJ 94, 381
- Draganić, I. G., Draganić, Z. D. 1984, AdvSpaceRes 4, 115
- Dutrey, A., Despois, D., Bockelée-Morvan, D., et al. 1996, IAU Circ., 6364
- Ehrenfreund, P., Gerakines, P. A., Schutte, W. A. et al. 1996, A&A, 312, 263
- Elman B. S., Dresselhaus M. S., Dresselhaus G. et al. 1981, PhRvB, 24, 1027
- Etim, E. E., Gorai, P., Das, A., Chakrabarti, S. K., Arunan, E. 2016, ApJ, 832, 144
- Famá, M., Loeffler, M. J., Raut, U., Baragiola, R. A. 2009, Icarus, 207, 1, 314
- Fedoseev, G., Cuppen, H. M. Ioppolo et al. 2015, MNRAS, 448, 1288
- Fedoseev, G., Chuand, K. J., van Dischoeck, E. F. et al. 2016, MNRAS, 460, 4297
- Ferini, G., Baratta, G.A. & Palumbo, M.E. 2004, A&A, 414, 757
- Fontani, F., Codella, C., Ceccarelli, C., Lefloch, B., Viti, S., Benedettini, M. 2014, ApJ Letters, 788, L43
- Fontani, F., Caselli, C., Favre, C. Caselli, P. et al. 2017, A&A, in press arXiv:1707.01384
- Fossé, D., Cernicharo, J., Gerin, M., Cox, P., The Astrophysical Journal 2001, 552, 168
- Fraser, H. J., Collings, M. P., Dever, J. W., et al. 2004, MNRAS, 353, 59
- Fresneau, A., Abou Mrad, N., d'Hendecourt, L. L. S., Duvernay, F. et al. 2017, ApJ, 837, 168
- Fuchs, G. W., Acharyya, K., Bisschop, S. E. et al. 2006, Faraday Discuss., 133, 331
- Fuchs, G. W., Cuppen, H. M., Ioppolo, S. et al. 2009, A&A, 505, 629
- Fulvio, D., Sivaraman, B., Baratta, G. A. et al. 2009, Spectrochim. Acta A, 72, 1007

- Füri, E. & Marty, B. 2015, *Nature Geoscience*, 8, 515
- Gálvez, Ó., Maté, B., Herrero, V. J. and Escribano, R. 2011, *ApJ*, 738, 133
- Garrod R.T. & Herbst E. 2006, *A&A* 457, 927
- Gerakines, P. A., Schutte, W. A., Greenberg, J. M. & van Dishoeck, E. F. 1995, *A&A*, 296, 810
- Gerakines, P. A., Schutte, W. A. & Ehrenfreund, P. 1996, *A&A*, 312, 289
- Gerakines, P. A., & Moore, M. H. 2001, *Icarus*, 154, 372
- Gerakines, P. A., Moore, M. H. & Hudson, R. L. 2004, *Icarus*, 170-202
- Gerakines, P. A., Bray, J. J., Davis, A. & Richey, C. R. 2005, *ApJ*, 620, 1140
- Gibb, L., Whittet, D. C. B., Boogert, A. C. A. and Tielens, A. G. G. M. 2004, *ApJSS*, 151, 35-73
- Giguère, P. A. & Falk, M. 1956, *Canadian Journal of Chemistry*, 34, 1833-1835
- Gillett, F. C. and Forrest, W. J. 1973, *ApJ*, 179, 483-491
- Goesmann, F., Rosenbauer, H., Bredhöft, J. H. et al. 2015, *Science*, 349, aab06891
- Goldsmith, P. F. & Langer, W. D. 1999, *ApJ*, 517, 209
- Gould, R. J. and Salpeter, E. E. 1963, *ApJ*, 138, 393-407
- Gounelle, M., Shu, F. H., Shang, H., Glassgold, A. E., Rehm, K. E. Lee, T. 2006, *ApJ*, 640, 1163
- Greenberg, J. M. 1973, *Molecules in the Galactic Environment*, ed. Gordon, M. A., Snyder, L. E., Wiley, NY
- Greenberg, J. M. 1982, in *Comets (A83-13376 03-90)* (Tucson, AZ: University of Arizona Press), 131
- Grim, R. J. A., & Greenberg, J. M. 1987, *ApJ*, 321, L91
- Grim, R. J. A., Greenberg, J. M., de Groot, M. S., Baas, F., Schutte, W. A. & Schmitt, B. 1989, *A&ASS*, 78, 2, 161
- Grundy, W. M. & Schmitt, B. 1998, *J. Geophys. Res.* 103, E11, 25809
- Grundy, W. M., Buie, M. W., Stanberry, J. A., Spencer, J. R. & Schmitt, B. 1999, *Icarus*, 142, 536
- Guelin, M. Langer, W.D., Wilson, R.W. 1982, *A&A*, 107, 107
- Hallis, L. J. 2017, *Phil. Trans. R. Soc. A*, 375, 20150390
- Hartogh, P., Lis, D. C., Bockelée-Morvan, D. et al. 2011, *Nature*, 478, 7368, 218
- Hasegawa, T. I., & Herbst, E. 1993, *MNRAS*, 261, 83
- Henderson, B. L. & Gudipati, M. S. 2015, *ApJ*, 800, 66
- Henderson, B. L. & Gudipati, M. S. 2015, *ApJ*, 800, 66

- Herbst, E. & van Dishoeck, E. F. 2009, *ARAA*, 47, 427-480
- Hollenbach, D. and Salpeter, E. E. 1971, *ApJ*, 163, 155-164
- Hudgins, D. M., Sandford, S. A., Allamandola, L. J. et al. 1993, *ApJS*, 86, 713
- Hudson, R. L., Moore, M. H. & Gerakines, P. A. 2001, *ApJ*, 550, 1140
- Indriolo, N. & McCall, B. J. 2012, *ApJ*, 745, 91
- Irvine, W.M., Goldsmith, P.F., Hjalmarso, A. 1987, *Interstellar Processes*, ed. D. Hollenbach and H. Thronson (Dordrecht:Reidel), 561
- Irvine W.M., Bockelée-Morvan D., Lis D.C., et al. 1996, *Nature*, 382, 418
- Islam, F., Baratta, G. A. & Palumbo, M. E. 2014, *A&A*. 561, A73
- Ivlev, A.V., Röcker, T.B., Vasyunin, A. and Caselli, P. 2015, *ApJ*, 805, 59
- Jaber, A.A., Ceccarelli, C., Kahane, C., Viti, S., Balucani, N., Caux, E., Faure, A., Lefloch, B., Lique, F., Mendoza, E., Quenard, D. & Wiesenfeld, L. 2017, *A&A*, 597, A40
- Jacq, T., Jewell, P. R., Henkel, C., Walmsely, C. M., Baudry, A. 1990, *A&A*, 199, L5-L8
- Jamieson, C. S., Mebel, A. M., & Kaiser, R. I. 2006, *ApJS*, 163, 184
- Jenniskens, P. & Blake, D. F. 1994, *Science*, 265, 753-756
- Jones, B. M., Bennett, C. & Kaiser, R. I. 2011, *ApJ*, 734, 78
- Jørgensen, J. K., van der Wiel, M. H. D., Coutens, A. et al. 2016, *A&A*, 595, A117
- Kaifu, N., Ohishi, M., Kawaguchi, K., Saito, S., Yamamoto, S., Miyaji, T., Miyazawa, K., Ishikawa, S.I., Noumaru, C., Harasawa, S., Okuda, M. 2004, *PASJ*, 56, 69-173
- Katz, A. I., Schiferl, D., Mills, R. L. 1984, *J. Phys. Chem.* 88, 3176
- Kalish R., Reznik A., Nugent K. W. et al. 1999, *NIMPB*, 148, 626
- Kama, M., López-Sepulcre, A., Dominik, C., Ceccarelli, C. et al. 2013, *A&A*, 556, A57
- Kaňuchová, Z., Urso, R.G., Baratta, G.A., Brucato, J.R. Palumbo, M.E. and Strazzulla, G. *A&A*, 585, A155
- Kuiper, T.B.H., Langer, W.D., Velusamy, T. 1996, *The Astrophysical Journal*, 468:761-773
- Ladell, J. & Post, B. 1954, *Acta Crystallogr.*, 7, 599
- Langer, W. D. and Penzias, A. A. 1990, *ApJ*, 357, 477-492
- Lantz, C., Brunetto, R., Barucci, M. A., Fornasier, S., Baklouti, D., Burçois, J. and Godard, M. 2017, *Icarus*, 285, 43-57
- Larson, R. B. 2003, *Rep Prog Phys*, 66, 1651
- Lasne, J., Rosu-Finsen, Al., Cassidy, A. et al. 2015 *PCCP*, 17, 30177

- Lauretta, D.S., Nagahara, H., Alexander, C.M.O. 2006, in Lauretta, D. S. and McSween, H. Y. (Eds.), *Meteorites and the Early Solar System II*, 431-459
- Lefloch, B., Castets, A., Chernicharo, J., Langer, W. D. & Zylka, R. 1999, *A&A*, 334, 269
- Lefloch, B., Cabrit, S., Busquet, G., Codella, C., Ceccarelli, C. et al. 2012, *Apj*, 757, L25
- Lefloch, B., Ceccarelli, C., Codella, C., Favre, C., Podio, L., Vastel, C., Viti, S. and Bachiller, R. 2017, *MNRAS*, 469, L73
- Léger, A., Jura, M., & Omont, A. 1985, *A&A*, 144, 147
- Leto, G. & Baratta, G. A. 2003, *A&A*, 397, 7-13
- Leto, G., Gomis, O. & Strazzulla, G. 2005, *Mem. S.A. It.*, 6, 57
- Le Roy, L., Altwegg, K., Balsiger, H. et al. 2015, *A&A*, 583, A2
- Lindblad, B. 1935, *Nature*, 135, 133-135
- Lis D.C., Keene J., Young T.G., et al. 1997, *Icarus* 130, 355
- Loeffler, M. J., Baratta, G. A., Palumbo, M. E., Strazzulla, G., Baragiola, R. 2005, *A&A*, 435, 587
- Loison, J.C., Wakelam, V., Hickson, K.M., Bergeat, A., Mereau, R. 2014, *MNRAS*, 437, 930-945
- Loison, J.C., Agúndez, M., Marcelino, N., Wakelam, V., Hickson, K.M., Cernicharo, J., Gerin, M., Roueff, E. and Guélin, M. 2016, *MNRAS*, 456, 4101
- Looney, L. W., Mundy, L. G., & Welch, W. J. 2000, *ApJ*, 529, 477
- Loewenschuss, A., Givan, A., Nielsen, C.J. 1997, *J. Mol. Struct.*, 408/409, 533
- López-Sepulcre, A., Taquet, V., Sánchez-Monge, Á., Ceccarelli, C., Dominik, C., Kama, M., Caux, E., Fontani, F., Fuente, A. Ho, P. T. P., Neri, R. & Shimajiri, Y. 2013, *A&A*, 556, A62
- López-Sepulcre, A., Jaber, A. A., Mendoza, E. Lefloch, B., Ceccarelli, C. et al. 2015, *MNRAS*, 449, 2438-2458
- Löwen, H. W., Bier, K. D., Jodl, H. J. 1990, *J. Chem. Phys.*, 93, 8565
- Lowenthal, M. S., Khanna, R. K., & Moore, M. H. 2002, *Spectrochim. Acta Part A*, 58, 73
- Lundell, J., Krajewska, M & Räsänen, M. 1998, *J. Phys. Chem. A*, 102, 6643
- Madden, W. G., Bergren, M. S., McGraw, R., Rice, S. A., & Sceats, M. G.
- Maki, A.G. 1961, *J. Chem. Phys.*, 35, 931
- Mangum, J.G., Wootten, A. 1990 *A&A*, 239, 319-325
- Marcelino N., Cernicharo J., Tercero B. et al. 2009, *ApJ*, 690, L27
- Mardyukov, A., Sánchez-García, E., RÓdziewicz, P. et al. 2007, *J. Phys. Chem. A*, 111, 10552

- Maret, S., Bergin, E. A., & Lada, C. J. 2006, *Nat* 442, 425
- Mason, N. J., Dawes, A., Holtom, P. D. et al. 2006, *Faraday Discussions*, 133,311-329
- Mastrapa, R. M. E. & Brown, R. H. 2006, *Icarus*, 183, 1, 207
- Matthews, H.E., Irvine, W.M., Friberg, P., Brown, R.D., Godfrey, P.D. 1984, *Nature*, 310, 125
- McGuire, B., Carroll, P.B, Loomis, R.A., Blake, G.A., Holliss, J.M., Lovas, F.J., Jewell, P.R., Remijan, A.J.2013, *ApJ*, 774, 56
- McKee, C. F. & Ostriker, E. C. 2007, *ARAA*, 45, 565
- McKellar, A. 1940, *Publ. Astron. Soc. Pac.* 52, 187
- Mendoza E., Lefloch B., López-Sepulcre A., et al. 2014, *MNRAS*, 445, 151
- Mennella, V., Baratta, G. A., Esposito, A. et al. 2003, *ApJ*, 587, 727
- Mennella, V., Hornekær, L., Thrower, J., Accolla, M. 2012, *ApJ*, 745, L2
- Miller, S. L. 1953, *Science*, 117, 528-529,
- Miller, J.S. 1970, *ApJ*, 191, L95
- Miyauchi, N., Hidaka, H., Chigai, T. et al. 2008, *Chem. Phys. Lett.*, 456, 27
- Modica, P., & Palumbo, M. E. 2010, *A&A*, 519, A22
- Modica, P., Palumbo, M. E., & Strazzulla, G. 2012., *PLSpSci* 73, 425
- Moore, M. H., Donn, B., Khanna, R. & A’Hearn, M. F. 1983, *Icarus*, 54, 388
- Moore, M. H. & Hudson, R. L. 1992, *ApJ*, 401, 353
- Moore, M. H., & Hudson, R. L. 2000, *Icarus* 145, 282
- Moore, M. H., Ferrante, R. F., Moore, W. J. et al. 2010, *ApJS*, 191, 96
- Motiyenko R. A., Tercero B., Cernicharo J., et al. 2012, *A&A*, 548, A71
- Morrison, D., Johnson, T. V., Shoemaker, T. M., Soderblom, L. A., Thomas, P., Veverka, J. & Smith, B. A. 1984, *Saturn* (Tucson: University of Arizona Press), p. 609
- Moynier, F., Yin, Q., Jacobsen, B. 2007, *ApJ*, 671, 2, L181-L183
- Mumma M.J., Weissman P.R., Stern A. 1993, In: Levy E.H., Lunine J.I. (eds.) *Protostars and Planets III*, (Tucson, AZ: University of Arizona Press), 1177
- Mundy, L.G., Wootten, A., Wilking, B.A., Blake, G.A., Sargent, A.I. 1992, *ApJ*, 385, 306
- Munõz Caro, G.M., Chen, Y.-J., Aparicio, S. et al. 2016, *A&A*, 589, A19
- Nagy, Z., Choi, Y., Ossenkopf-Okada, V., van der Tak, F. F. S., Bergin, E. A., Gerin, M., Joblin, C., Röllig, M., Simon, R. and Stutzki, J. 2017, *A&A*, 599, A22

- Nash, D. B. & Betts, B. H. 1995, *Solar System Ices*, vol 227 (Dordrecht; Kluwer Academic Publisher - ASSL Series) p.607
- Nealander, B. 1985, *J.Phys. Chem*, 89, 827
- Noble, J. A., Theule, P., Congiu, E., et al. 2015, *A&A* 576, A91
- Nummelin, A., Bergman P., Hjalmarson Å., et al. 2000, *ApJS*, 128, 213
- Nummelin, A., Whittet, D. C. B., Gibb, E. L. et al. 2001, *ApJ*, 558, 185
- Öberg, K. I., van Dishoeck, E. F., Linnartz, H. 2009 *A&A*, 496, 281
- Öberg, K. I., Boogert, A. C. A., Pontoppidan, K. M., van den Broek, S., van Dishoeck, E. F., Bottinelli, S., Blake, G. A. and N. J. Evans II 2011, *ApJ*, 740, 109
- Ohishi, M., Ishikawa, S., Yamada, C., et al. 1991, *ApJ*, 380, L39
- Paardekooper, D. M., Fedoseev, G., Riedo A. and Linnartz, H. 2016, *A&A*, 596, A72
- Padovani, M., Galli, D., & Glassgold, A. E. 2009, *A&A* 501, 619
- Padovani, M., Hennebelle, P., & Galli, D. 2013, *A&A* 560, A114
- Paganini, L., DiSanti, M. A., Mumma, M. J., et al. 2014a, *AJ* 147, 15
- Paganini, L., Mumma, M. J., Villanueva, G. L., et al. 2014b, *ApJ* 791, 122
- Palla, F. & Stalher, S. W. 2002, *ApJ*, 581, 1194
- Palumbo, M. E., & Strazzulla, G. 1993, *A&A*, 269, 568
- Palumbo, M. E., Geballe, T. R. and Tielens, A. G. G. M. 1997, *ApJ*, 479, 839
- Palumbo, M.E., Castorina, A.C. & Strazzulla, G. 1999. *A&A*, 342, 551
- Palumbo, M. E. & Baratta, G. A. 2000, *A&A*, 361, 298
- Palumbo, M. E., Ferini, G. & Baratta, G. A. 2004, *Adv. Space Res.*, 33, 49
- Palumbo, M.E. 2006 *A&A*, 453, 903
- Palumbo, M. E., Baratta, G. A, Collings, M. P. et al. 2006, *PCCP*, 8, 279
- Palumbo, M.E., Leto, P., Siringo, C., Trigilio, C. 2008, *The Astrophysical Journal*, 685:1033-1038
- Palumbo, M.E., Baratta, G.A., Leto, G. et al. 2010, *Journal of Molecular Structure*, 972, 1-3, 64
- Palumbo, M. E., Urso, R. G., Kanuchova, Z., Scire, C., Accolla, M. Baratta, G. A. and Strazzulla, G. 2016, *Conditions and Impact of Star Formation*, Simon, R., Schaaf, R. and Stutzki, J. (eds), *EAS pub. ser.*, 75-76, 309-314
- Parise, B., Simon, T., Caux, E., Dartois, E., Ceccarelli, C., Rayner, J. & Tielens, A. M. M. A. 2003, *A&A*, 410, 897
- Pineda, J. E., Caselli, P., Goodman, A. A. 2008, *ApJ*, 679, 481-496

- Pino, S., Spooner, J. E., Costanzo, G. et al. 2015, *Life*, 5, 372-384
- Pirronello, V. Liu, C., Roser, J. E. & Vidali, G. 1999, *A&A*, 344, 681-686
- Pizzarello, S., Cooper, G. W., Flynn, G. J. 2006, in Lauretta, D. S. and McSween, H. Y. (Eds.), *Meteorites and the Early Solar System II*, 625-651
- Podio, L., Lefloch, B., Ceccarelli, C., et al. 2014, *A&A* 565, id.A64
- Pollack, J. B., Hubickyj, O., Bodenheimer, P. et al. 1996, *Icarus*, 124, 62
- Pontoppidan, K.M., Fraser, H.J., Dartois, E., et al. 2003, *A&A*, 408, 981
- Prasad, S. S. & Tarafdar, S. P. 1983, *ApJ*, 267, 603
- Quirico, E. & Schmitt, B. 1997, *ICARUS*, 127, 354
- Räsänen, M. 1983 (a), *J. Mol. Struct.* 101, 275
- Räsänen, M. 1983 (b), *J. Mol. Struct.* 102, 235
- Raunier, S., Chiavassa, T., Duvernay, F., et al. 2004, *A&A* 416,165
- Raut, U., Loeffler, M. J., Vidal, R. A. & Baragiola, R. A. 2004, *LPI*, 35, 1922
- Raut, U., Fama, M., Teolis, B.D. et al. 2007, *Bulletin of American Astronomical Society*, 39, 489
- Raut, U., Teolis, B. D., Loeffler, M. J., Vidal, R. A., Famá, M. & Baragiola, R. 2007, *J. Chem. Phys.*, 126, 244511
- Rodríguez-Fernández N. J., Tafalla M., Gueth F., et al. 2010, *A&A*, 516, 98
- Rothard, H., Domaracka, A., Boduch, P., Palumbo, M. E., Strazzulla, G., da Silveira, E. F. and Dartois, E. 2017, *J. Phys. B: At. Mol. Opt. Phys.*, 50, 062001
- Rowland, B., Fisher, M., & Devlin, J. P. 1991, *J. Chem. Phys.*, 95, 1378
- Rubin, R. H., Swenson, G. W., Benson, R. C. et al. 1971, *ApJ*, 169, L39-L44
- Rubin, M., Altwegg, K., Balsiger, H., et al. 2015. *Sci* 248, 232
- Saladino, R., Crestini, C., Neri, V. et al. 2005, *ChemBioChem*, 6, 1368
- Saladino, R., Crestini, C., Ciciriello, F. et al. 2009, *Res. Microbiol.*, 160, 441-448
- Saladino, R., Crestini, C., Pino, S., et al. 2012, *PhLiRe*, 9, 84
- Sandford, S.A., Allamandola, L.J., Tielens, A.G.G.M. et al. 1988, *Astrophys. J.*, 329, 498
- Sandford, S. A., Allamandola, L. J. 1993, *ApJ*, 417, 2, 815
- Santangelo, G., Codella, C. Cabrit, S., Maury, A. J. et al. 2015, *A&A*, 584, A126
- Schmitt, B., Grimm, R. & Greenberg, M. 1988, *Proc. 22nd ESLAB Symposium on Infrared Spectroscopy in Astronomy*, ESA SP-290, pp. 213-219.

- Schmitt, B., Grimm, R. & Greenberg, M. 1988, Proc. 22nd ESLAB Symposium on Infrared Spectroscopy in Astronomy, ESA, SP-290, 213
- Schmitt, B., de Bergh, C. & Festou, M. 1998, Solar System ices (Dordrecht: Kluwer)
- Schutte, W. A., Gerakines, P. A., van Dishoeck, E. F., Greenbergand, J. M. and Geballe, T. R. 1994, AIP Conference Proceedings, 312, 73
- Schutte, W. A., Boogert, A. C. A., Tielens, A. G. G. M., et al. 1999, A&A, 343, 966
- Seperuelo Duarte, E., Domaracka, A., Boduch, P., et al. 2010, A&A, 512, A71
- Seperuelo Duarte, E., Domaracka, A., Boduch, P. et al. 2010, A&A, 512, A71
- Shen, C. J., Greenberg, J. M., Schutte, W. A. et al. 2004, A&A, 415, 203
- Shimajiri, Y., Takahashi, S. Takakuwa, S. Saito, M. & Kawabe, R. 2008, ApJ, 683, 255
- Shimajiri, Y., Sakai, T., Kitamura, Y., Tsukagoshi, T., Saito, M. et al. 2015, ApJSS, 221, 31
- Sicilia, D., Ioppolo, S., Vindigni, T., Baratta, G. A., Palumbo, M.E. 2012, A&A, 543, A155
- Sims, I.R. & Smith, W.M. 1995, Annu. Rev. Phys. Chem. 46, 109
- Sivaraman, B., Raja Sekar, B. N., Jones, N. C. et al. 2012, Chem. Phys. Lett., 554, 57
- Sivaraman, B., Raja Sekar, B. N., Nair, B. G. et al. 2013, Spectrochim Acta, Part A, 105, 238
- Sivaraman, B., Nair, B. G., Raja Sekhar, B. N. et al. 2014, Chem. Phys. Letters, 603, 33-36
- Skouteris, D., Vazart, F., Ceccarelli, C., Balucani, N., Puzzarini, C. and Barone, V. 2017, MNRAS, 468, L1
- Soifer, B. T., Puetter, R. C., Russell, R. W., et al. 1979, ApJ 232, L53
- Stahler, S. W. & Palla, F. 2005, Ward Thompson D., A star is born how, exactly, Astronomy & Geophysics, 46, 3, 38
- Strazzulla, G., Calcagno, L. and Foti, G. 1983, MNRAS, 204, 59
- Strazzulla, G. & Johnson, R. E. 1991, in Comets in the Post-Halley Era, ed. R. L. Newburn, Jr., M. Neugebauer & J. Rahe (Dordrecht: Kluwer), 243
- Strazzulla, G., Baratta, G. A., Johnson, R. E., et al. 1991, Icarus 91, 101
- Strazzulla G., Baratta G. A., 1992, A&A, 266, 434
- Strazzulla, G., Brucato, J. R., Palumbo, M. E., Satorre, M. A. 1997, A&A, 321, 618
- Strazzulla, G., Baratta, G. A. & Palumbo, M. E. 2001, Spectrochimica Acta A, Molecular and Biomolecular Spectroscopy, 57, 4, 825
- Strazzulla, G., Leto G., Gomis, O.,& Satorre, M. A. 2003, Icarus 164, 163
- Strom, S. E., Strom, K. M. & Grasdalen, G. L. 1975, ARAA, 13, 187
- Suhai, S. 1996, J. Phys. Chem., 100, 3950

- P. Swings, L. Rosenfeld, Considerations regarding interstellar molecules. *Astrophys. J.* 86, 483
- Tegler, S.C., Weinteraud, D.A., Rettig, T.W., Pendleton, Y.J., Whittet, D.C.B., Kulesa, C.A. 1995, *ApJ*, 439, 279
- Teixeira, T. C., Devlin, J. P., Buch, V. and Emerson, J. P. 1999, *A&A*, 347, L19-L22
- Tenenbaum, E. D., Aponi, A. J., Ziurys, L. M., Agundez, M., Cernicharo, J., Pardo, J. R., Guelin, M. 2006, *ApJ*, 649, L17
- Tielens, A.G.G.M. & Hagen, W. 1982, *A&A* 114, 245
- Tielens, A. G. G. M., Tokunaga, A. T., Geballe, T. R., & Baas, F. 1991, *ApJ*, 381, 181
- Thomas, P., Veverka, J. & Dermott, S. 1986, *Satellites* (Tucson: University of Arizona Press), p. 802
- Torrie, B. H. & Brown, B. A. 1994, *J. Raman Spectrosc.*, 25, 183
- Trottier, A. & Brooks, R. L. 2004, *ApJ*, 612, 1214
- Turner, B. E., Zuckerman, B., Fourikis, N. Morris, M. and Palmer, P. 1975, *ApJ*, 198, L125-L128
- Turner, B.E., Herbst, E., Terzieva, R. 2000, *The Astrophysical Journal Supplement Series*, 126:427-460
- Urso, R.G., Scirè, C., Baratta, G.A., Compagnini, G. and Palumbo, M.E. 2016, *A&A*, 594, A(80)
- Urso, R. G., Scirè, C., Baratta, G. A., Brucato, J. R., Compagnini, G., Kaňuchová, Z., Palumbo, M. E. and Strazzulla, G. 2016, *A&A*, 594, A80
- van Broekhuizen F. A., Keane, J. V.; Schutte, W. A. 2004, *A&A* 415, 425
- van Broekhuizen, F. A., Pontoppidan K. M., Fraser, H. J., van Dishoeck E. F. 2005, *A&A* 441, 249
- van de Hulst H. 1946, *Rech. Astron. Obs., Utrecht*, 11,2
- Vastel, C., Ceccarelli, C., Lefloch, B., Bachiller, R. 2014, *The Astrophysical Journal Letters*, 795:L2
- Vazart, F., Latouche, C., Skouteris, D., Balucani, N., Barone, V. 2015, *ApJ*, 810, 111
- Vazart, F., Calderini, D., Puzzarini, C & Barone, V., 2016, *J. Chem. Theory Comput.* 12, 5385
- Wakelam, V., Herbst, E., Loison, J. C., Smith, I. W., Chandrasekaran, V., Pavone, B., Adams, N. G. et al. 2012, *ApJ Supp. Ser.* 199:21
- Watanabe, N. & Kouchi, A. 2002, *ApJ*, 571, L173-L176
- Webber, W. E. 1998, *ApJ*, 506, 329
- Wiener, R. N. and Nixon, E. 1956, *The Journal of Chemical Physics*, 25, 175, 175
- Willacy, L., Langer, W.D., Velusamy, T. 1998, *The Astrophysical Journal*, 507:L171-L175
- Willacy, K. & Millar, T. J. 1988, *MNRAS*, 298, 562-568

- Wilson, R. W., Jefferts, K. B. & Penzias, A.A. 1970, ApJ 161, L43
- Woodney L.M., McMullin J., A'Hearn M.F. 1997, Planet. Space Sci. 45, 717
- Woods, P., Occhiogrosso, A., Viti, S. et al. 2015, MNRAS, 450, 1256
- Woon, D.E. and Herbst, E. 2009, ApJSS, 185, 273
- Wootten, A., Bozyan, E. P., Garrett, D. B., Loren, R. B., Snell, R. 1980, The Astrophysical Journal, 239:844-854
- Wootten, A. 1989, ApJ, 337, 858
- Yamamoto, S., Saito, S., Ohishi, M., Suzuki, H., Ishikawa, S.I., Kaifu, N., Murakami, A., ApJ, 322:L55-L58, 1987
- Yamamoto, S. 2014, Introduction to Astrochemistry, A&A Library, Springer, DOI 10.1007/978-4-431-54171-4
- Zheng, W., Jewitt, D. & Kaiser, R. I. 2006, ApJ, 639, 534-548
- Ziegler, J.F., Biersack, J.P., & Ziegler, M.D. 2008, The Stopping and Range of Ions in Solids (New York: Pergamon Press), 321

7.1 Acknowledgements

Here I would like to thank all the people were involved in this work. First of all, I want to express my deepest gratitude to my tutors, Prof. Giuseppe Compagnini and Dr. Maria Elisabetta Palumbo, together with all the LAsp team members, Dr. Giovanni Strazzulla, Dr. Giuseppe Baratta, Dr. Carlotta Scirè, Dr. Mario Accolla and Dr. Gleb Fedoseev. A warm thanks to Prof. Cecilia Ceccarelli and all the people I met at the IPAG. Thanks to all the friends I met at INAF-Osservatorio Astrofisico di Catania, and to all the colleagues I met in these years. I'm grateful to Prof. Salvo Mirabella and Prof. Enrico Ciliberto that encouraged me to start this amazing journey Finally I thank my parents, my brother and Federica for all the unconditional love and support.